# Hydrocarbon Potential of the Upper Green River Petroleum System in the Uinta Basin, Utah: A Basin Modeling Approach

---

A Thesis Presented to

the Faculty of the Department of Earth and Atmospheric Sciences

University of Houston

---

In Partial Fulfillment

of the Requirements for the Degree

Master of Science

---

By

Robert Raschilla

May 2013

# Hydrocarbon Potential of the Upper Green River Petroleum System in the Uinta Basin, Utah: A Basin Modeling Approach

**Robert Raschilla**

APPROVED:

**Dr. Jolante Van Wijk, Chairman**

**Dr. Alexander Robinson**

**Dr. Darrin Burton**

**Dan E. Wells, Dean, College of Natural Sciences and Mathematics**

## ACKNOWLEDGEMENTS

I would like to thank Dr. Jolante Van Wijk for guiding me through this process, supporting the research topic that I selected, and providing exceptional ideas. Likewise, I would like to extend my genuine thanks to my committee members Dr. Alexander Robinson and Dr. Darrin Burton. My deepest gratitude goes to Newfield Exploration for providing the data set and software packages that made this study possible, as well as their supportive employees who provided numerous beneficial suggestions along the way. Nancy Hunter, from Platte River Associates, spent numerous hours assisting me with software issues and for this, I am extremely grateful. Finally, I want to thank all of my friends and family for their patience, understanding, and support during this mammoth endeavor.

# Hydrocarbon Potential of the Upper Green River Petroleum System in the Uinta Basin, Utah: A Basin Modeling Approach

---

An Abstract of a Thesis Presented to

the Faculty of the Department of Earth and Atmospheric Sciences

University of Houston

---

In Partial Fulfillment

of the Requirements for the Degree

Master of Science

---

By

Robert Raschilla

May 2013

## ABSTRACT

The Late Cretaceous Uinta Basin is a foreland basin located in northeastern Utah within the northern most portion of the Colorado Plateau. The basin's uplift and subsidence history and thermal evolution have impacted the maturity of source beds in the Parachute Creek Member. Sixty wells and three 2-D models generated from well logs are used in a basin modeling study of the Uinta Basin's thermal structure, tectonic history, and petroleum system. These factors impact the maturation of source rocks within the Parachute Creek Member of the Green River Formation. All models were calibrated to measured data, including vitrinite reflectance and transformation ratios from Rock-Eval pyrolysis. The models predict that the heat flow ranges from 65 $mW/m^2$ to 45 $mW/m^2$ from south to north in the study area. Additionally, model calibration provides a means for estimating the amount of uplift and erosion in the Uinta Basin. For the three 2-D models, uplift and erosion predicted for the Uinta Basin ranges from 6700 ft to 7200 ft (2042 m to 2195 m). Based on the eroded thicknesses and heat flow values determined from calibration to measured thermal maturity indicators, the maturity of the rich oil shales of the Parachute Creek Member is inferred. Model predictions have suggested that source intervals of the Parachute Creek Member follow a general trend of increasing maturity from south to north in the study area. Local variations in predicted maturity that deviate from this trend most likely occur due to the effects of decreasing heat flow outpacing the effects of greater burial depths from south to north.

## CONTENTS

## CHAPTER 1: Introduction

The purpose of this study is to conduct a basin analysis of the Uinta Basin in northern Utah, USA (Figure 1). The focus is primarily on the burial history, thermal maturity, and timing of hydrocarbon generation for the upper most petroleum system within the Green River Formation. The upper petroleum system is comprised of the alternating rich and lean zones of the Parachute Creek Member. Rich zones include the R8, the Mahogany oil shale (R7), the R6, the GG0 (Garden Gulch), the GG, the GG1, and the GG2 (Figure 3). Lean zones include the A Groove, B Groove, L5, L4, L3, and L2 (Figure 3). These intervals are situated stratigraphically beneath the Uinta and Duchesne River Formations and above the Douglas Creek Member. Zones of the upper petroleum system, such as the Mahogany oil shale, contain large amounts of TOC (total organic carbon), are laterally extensive, and are of significant economic interest (Tissot et al., 1978; Ruble et al., 2001).

The upper petroleum system of the Uinta Basin is not well understood. Previous modeling efforts have largely focused on the burial history of the Shell 1-11-B4 Brotherson well (Sweeney et al., 1987; Anders et al., 1992; Fouch et al., 1994; and Ruble et al., 2001). Some of these studies have concluded that the Parachute Creek Member, including the rich Mahogany oil shale, has been buried to sufficient depths to generate hydrocarbons and others have predicted that the Parachute Creek Member may remain largely immature. The aim of this study is to provide constraints on Cenozoic uplift and heat flow in the Uinta Basin in order to assess their influence on the maturity of some of the world's richest oil shales. In this study, the Uinta Basin's burial history and thermal

structure are modeled in 1-D using 60 wells. Three north-south trending cross sections are constructed from the 60 wells in order to generate three 2-D basin models. Models are calibrated to measured geochemical data from the basin to assess the influence of heat flow and erosion on maturation of the upper petroleum system. The software packages BasinMod 2011 and BasinMod 2-D (Platte River Associates) are used for the basin analysis. 1-D and 2-D models are generated from interval thicknesses, rock properties, ages, and geochemical data. The models are constrained by data from many wells and the tectonic events that shaped the Uinta Basin. The basin analysis includes the Uinta Basin's burial history and thermal structure and their effect on generation, migration, and the maturity of the source rocks of interest. Since heat flow is constrained by the works of several previous researchers, calibration of the models to measured thermal maturity indicators can provide a method to constrain uplift and erosion in the northern Colorado Plateau. Uplift and erosion can be adjusted by iteration until an agreement is brought forth between measured thermal maturity indicators and predicted maturity.

The following sections in this study are divided into chapters. Chapter 2 describes the geologic setting and includes discussions of the petroleum system, tectonic history, and the evolution of the lacustrine depositional system. Chapter 3 describes the methods used to construct basin models, the inputs required, and the calibration process and types of data utilized during this procedure. Chapter 4 describes the results of the models, chapter 5 is a discussion of the results, and chapter 6 includes conclusions drawn from the study.

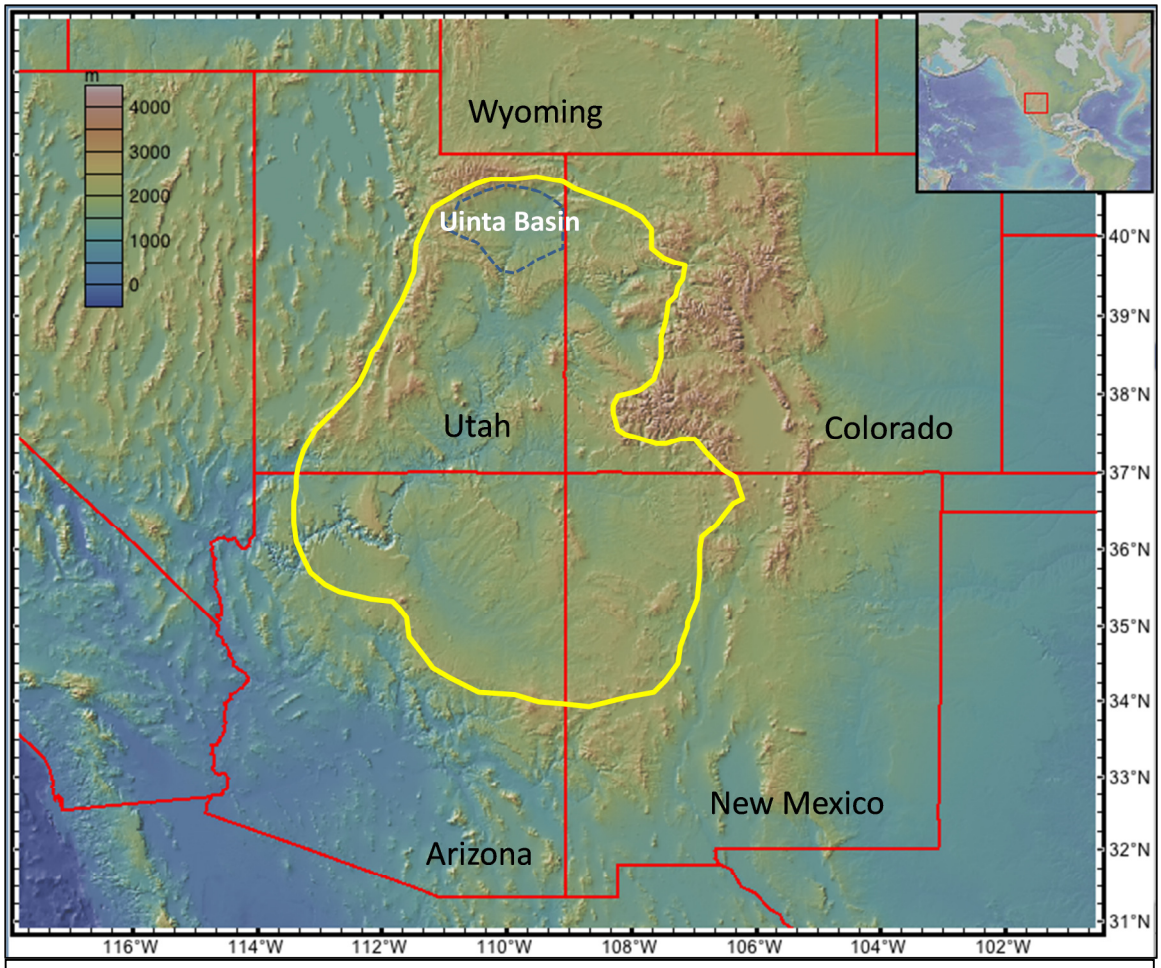


***Figure 1***: Topographic map of the western U.S. The Uinta Basin (blue dotted line) is located in the northern most portion of the Colorado Plateau (yellow line) in northeast Utah.

## CHAPTER 2: Geologic Setting of the Uinta Basin

### 2.1 Petroleum System of the Uinta Basin

The Uinta Basin is a foreland basin located in northeastern Utah within the northern most portion of the Colorado Plateau (Figure 1). The basin forms an asymmetric depression that is flanked by reverse faulted uplifts formed during the Laramide orogeny (Dubiel, 2003). The Uinta Basin covers approximately 9300 $mi^2$ (24086.9 $km^2$) (Osmond, 1965) and is filled with roughly 16400 ft (5000 m) of late Cretaceous to Oligocene age fluvial and lacustrine sediments (Johnson, 1985; Fouch et al., 1994). It is bounded by the Uinta Mountains to the north, the Wasatch Plateau and the Wasatch Mountains to the west, the San Rafael Uplift, Book Cliffs and Uncompahgre Uplift to the south, and the Douglas Creek Arch to the east (figure 2). The Douglas Creek Arch separates the Uinta Basin from the adjacent Piceance Creek Basin in Colorado (Figure 2). The synclinal axis of the basin is located just south of the Uinta Mountains (Tissot et al., 1978). Strata toward the southern margin of the basin are broad and shallowly dipping (4-6 degrees), whereas nearly vertical beds characterize the northern margin where strata are faulted alongside the southern margin of the Uinta uplift (Osmond, 1965; Johnson, 1985; and Fouch et al., 1994). About 3000 – 6000 ft (914 – 1828.8 m) of relief exists between the basin's lowest lying areas and its margins (Osmond, 1965).

The main focus of this study is on the middle to upper Green River petroleum system within the Uinta Basin. Figure 3 shows a generalized stratigraphic column of the intervals of interest in the study compared with a well log with the top of the Wasatch

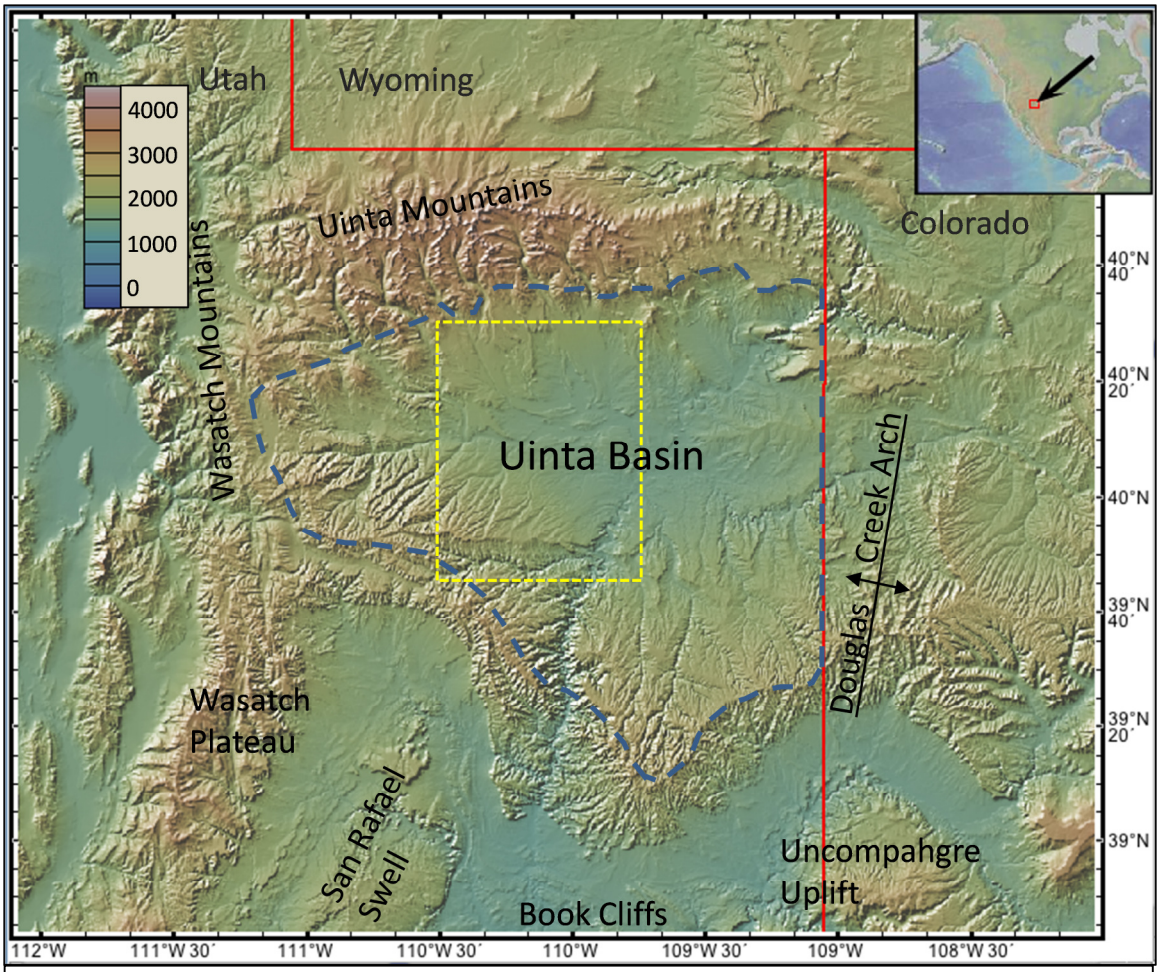


***Figure 2***: Key structural features that delineate the Uinta Basin. The approximate location of the study area is outlined in yellow. The approximate extent of the Uinta Basin is represented by the blue dashed line.

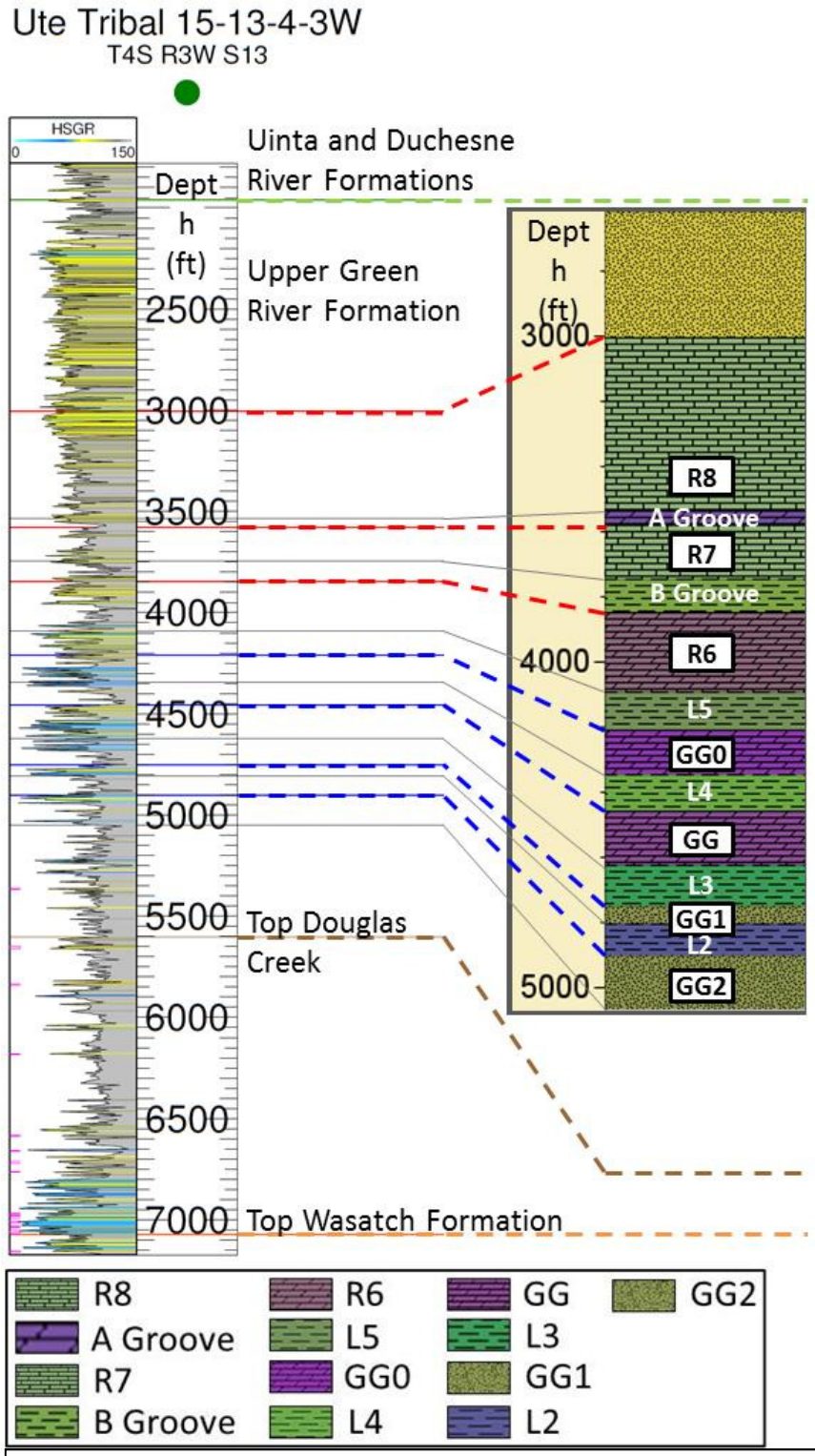


***Figure 3***: Generalized stratigraphic column showing the position of the rich and lean zones of the Parachute Creek Member. These zones are located approximately 2000 ft (609.6 m) above the top of the Wasatch Formation.

Formation marked for reference. The Green River Formation, within the Uinta Basin, is a productive interval of Eocene age lacustrine sediments. In conjunction with the Wasatch and Colton Formations, the Green River petroleum system has produced over 500 million barrels of oil (Morgan et al., 2003). The Green River Formation was deposited in an ancient lake system where anoxic and restricted conditions created an ideal environment for the preservation of organic material (Fouch et al., 1994). Within this lacustrine depositional system, the Green River Formation is composed of three key depositional facies (Ryder et al., 1976): open lacustrine, marginal lacustrine, and alluvial. Open lacustrine facies occupy the most distal depositional environment within the Uinta Basin. Open lacustrine deposits are made up of organic-rich (type 1 kerogen) mud supported carbonates and calcareous claystones that are interbedded with lean zones made up of sandstone, siltstone, carbonate packstone, and bedded chert (Ryder et al., 1976). In general, marginal lacustrine facies occupy a more proximal position, but intertongue with open lacustrine facies toward more distal areas. Marginal lacustrine facies are made up of sandstone, siltstone, carbonates, and claystones that were deposited in a deltaic to interdeltaic environment (Ryder et al., 1976). Alluvial facies are the most proximal deposits and are made up of channel sands, thinly bedded siltstone, very fine-grained sandstone, and red claystone. These deposits are associated with lower deltaic plain, high mud flat, and alluvial fan depositional environments (Ryder et al., 1976).

In the Green River Formation, type 1 kerogen-bearing lacustrine rocks are the principal source rocks. These source rocks are dominantly carbonate-rich shales and marlstones that were deposited in an open lacustrine environment (Fouch et al., 1994). Marginal lacustrine channel sands make up the major reservoirs (Fouch et al., 1994;

Ruble et al., 2001). In the study area, massive organic-rich oil shale deposits have been estimated to contain up to 321 billion barrels of oil (Cashion, 1964). The development of the Green River Formation's oil shale resources may have significant implications for the world's growing energy demands (Bartis et al., 2005).

### 2.2 Tectonic History of the Uinta Basin

During the Phanerozoic, the Uinta Basin was situated in an intraplate setting largely underlain by Phanerozoic rocks, which were deposited on top of a heterogeneous Precambrian basement (Johnson, 1992). The Uinta Basin is a typical feature of the Rocky Mountain foreland (Dickinson et al., 1988). This area is characterized by isolated nonmarine basins that formed in the response to basement deformation and thick skinned uplifts associated with the compressional tectonic setting of the Laramide orogeny in the late Cretaceous and Paleogene (Dickinson et al., 1988; Bader, 2009). The transformation of the continuous Rocky Mountain foreland into smaller separated basins occurred progressively after the initiation of the Laramide orogeny. By the late Cretaceous when the Laramide orogeny was in its earliest stages, the Uinta Basin was structurally defined by adjacent Laramide and Sevier uplifts. During this time, sedimentation was dominantly restricted to the western and central portions of the basin. By the early Paleogene, sedimentation was largely dictated by the changing hydrological system of Lake Uinta, tectonic activity, or changes in climate (Johnson, 1985). The tectonic history of the Uinta Basin is complex and includes folds, faults, and blocks that have recorded several different generations of tectonic stresses throughout the area's history (Osmond 1965). Although most of the tectonic events that contributed to the formation of the Uinta Basin

are of Cenozoic age, older features that pre-date the Laramide orogeny had prolonged or rejuvenated influence on the basin's formation and sedimentation during the Cenozoic. Reactivation of the Precambrian structural elements significantly controlled deformation and subsidence during the Phanerozoic (Johnson, 1992). As a result, the key tectonic events that influenced the Uinta Basin prior to the Cenozoic will be briefly discussed with emphasis on the Cenozoic history.

### *Cambrian to Middle Devonian*

From the Cambrian to the middle Devonian, rifting along the western margin of North America resulted in the development of a passive margin. Subsidence due to the generation of this passive margin was greatest west of the area associated with the Uinta Basin. Around 5000 ft (1524 m) of tectonic subsidence occurred in this area by the end of the Cambrian (Johnson, 1992). Around the late Precambrian to early Cambrian, folding, faulting, and tilting of the late Proterozoic Uinta Mountain Group in the area associated with the Uinta Mountains occurred (Hansen, 1986). This event is thought to have occurred due to the rejuvenation of pre-existing weaknesses along the E-W trending fault bounded depression that the Uinta Mountain Group was deposited within.

### *Late Devonian to Late Mississippian*

Beginning in the late Devonian, the Uinta Basin area was affected by the Antler orogeny, which is associated with an arc-continent collision that occurred in central Nevada (Johnson, 1992). West of the Uinta Basin, the generation of a thrust belt produced heightened subsidence rates and gave rise to new depositional patterns in the

western portion of the Uinta Basin area. The Uinta Basin region experienced approximately 1600 ft (487.7 m) of tectonic subsidence during this time. The sediment source for basins located east of the thrust sheet may have been a flexural bulge generated from the advancing thrust sheet (Goebel, 1991). Also, during this time of increased subsidence rates, multiple cratonic basins within North America experienced rejuvenation. Kominz and Bond (1991) have suggested that increased rates of subsidence in North American basins may be attributed to the early stages of the accretion of Pangaea. Antler activity was enhanced in the early Mississippian due to the emplacement of another allochthon and resulted in increased subsidence rates in the Uinta Basin area (Johnson, 1992).

***Middle Mississippian to Early Permian***

From the middle Mississippian to the early Permian, basement faults were reactivated due to a major continental collision that resulted in the uplift of the ancestral Rocky Mountains (Johnson, 1992; Foos, 1999). This uplift was driven by the collision between Gondwana and Laurasia on the southeast flank of North America (*in* Johnson, 1992). Deformation due to this collision was confined to areas possessing pre-existing weaknesses within North America (Kluth, 1986). Near the Uinta Basin area, an additional 1600 ft (487.7 m) of tectonic subsidence occurred (Johnson, 1992). During the Pennsylvanian, the Uncompahgre uplift, which now comprises a portion of the Uinta Basin's southern boundary, was uplifted near the present day location of the Uinta Basin's southern margin (Osmond, 1965; Osmond, 2003). The Uncompahgre uplift is a fault bounded basement cored uplift, which possessed significant structural and

topographic relief (Johnson, 1992). Toward the end of the Pennsylvanian, subsidence rates decreased and recently formed uplifts, such as the Uncompahgre uplift, were the major sources for clastic sediments. Later, this feature experienced rejuvenation during the Cenozoic when it became part of the southern boundary of the Uinta Basin (Osmond, 1965; Johnson, 1985).

### *Early Permian to Early Jurassic*

From the early Permian to the early Jurassic, the Uinta basin region experienced periods of rapid tectonic subsidence due to the emplacement of the Golconda allochthon in Nevada. During this time, increased subsidence rates were felt in the western Uinta Basin area and progressively decreased toward the east. Subsidence rates in the east may have been controlled by flexure caused by the loading of the Golconda allochthon toward the west (Johnson, 1992). From the middle Triassic to the early Jurassic, the Uinta Basin region was relatively stable with subsidence induced primarily by sediment loading rather than tectonics.

### *Middle Jurassic to Early Cretaceous*

Subsequently, from the middle Jurassic to the early Cretaceous, the region experienced a period of increased subsidence rates related to thrusting in eastern Nevada trailed by a time of decreased subsidence rates and tectonic stability. Subsidence rates were highest in the middle Jurassic and asymmetrical subsidence associated with this time suggests a flexural response to a load emplaced to the west. Allmendinger and Jordan (1981) have suggested that thrusting occurred west of the Sevier orogenic belt in

northwest Utah during the Jurassic and Thorman et al. (1991) have identified thrusting and folding in six different locals in northeastern Nevada during this time. Less than 1600 ft (487.7 m) of tectonic subsidence is associated with the middle Jurassic and little tectonic subsidence occurred during the early Cretaceous in the Uinta Basin region (Johnson, 1992).

### *Early Cretaceous to Late Eocene*

From the early Cretaceous to the late Eocene, the Sevier and Laramide orogenies played the dominant role in shaping the Rocky Mountain foreland and the Uinta Basin. The Sevier orogeny involved uplift and east directed thrusting from the Jurassic to the early Cenozoic and bounds the Uinta Basin toward the west (Johnson, 1985). The Sevier orogeny is characterized by back arc thrusting that occurred during a time of high angle subduction off the western margin of North America (Johnson, 1992). In front of the Sevier thrust belt, there existed a foreland basin that gave rise to a seaway that stretched from the Arctic Ocean to the Gulf of Mexico (Johnson, 1985). Subsidence of the foreland basin occurred due to flexure induced by loading of the thrust sheets (Johnson, 1992). During this time, depositional patterns were dictated by Sevier tectonic activity and eustasy, which controlled transgressions and regressions of the Cretaceous Interior Seaway (Fouch et al., 1983; Johnson, 1992). The episodic delivery of sediment corresponds with periodic thrusting events along the Sevier orogenic belt (Fouch et al., 1983). Thrusting and tectonic activity of the Sevier orogeny slowed down in Utah by the latest Cretaceous when the Laramide orogeny began (Johnson, 1985).

In the Uinta Basin region, the shift from Sevier to Laramide paleogeography happened sometime between the late Maastrichtian to early Paleocene and involved the withdrawal of the Cretaceous Interior Seaway, the creation of a regional unconformity, and the development of the Uinta Basin (Johnson, 1988). Shallow angle and more rapid subduction, shutting down of arc magmatism, and the movement of contractional deformation farther toward the east characterize the Laramide orogeny. The dominant style of deformation involved thrust or reverse fault bounded basement cored uplifts (Johnson, 1992). Also, the Colorado Plateau may have experienced a minor clockwise rotation (Hamilton, 1988). When Laramide deformation began, the Rocky Mountain region was divided into locally confined basins separated by emerging basement-cored uplifts that served as sediment sources (Dickinson et al., 1988). Horizontal compression of the foreland was influenced by northeast directed shallow angle subduction along the western coast of North America around 85 Ma (Bader, 2009). The deformation associated with the compressional stresses is expressed in the form of uplifts and basins. Uplifts formed as older basement faults were reactivated and basins subsided due to the flexural effect of thrusted loads on the lithosphere (Dickinson et al., 1988). The rejuvenation of Precambrian and late Paleozoic structural trends was important in dictating the location and geometry of uplifts and emergent basins during this time (Johnson, 1992).

From the late Cretaceous through the Cenozoic, the largest amount of tectonic activity affected the region and the compressive stresses of the Laramide orogeny were greatly felt in and around the Uinta Basin (Osmond, 1965). When Laramide deformation initiated in the Cretaceous, the Douglas Creek Arch, which separates the Uinta Basin from the Piceance Creek basin, began to be uplifted (Osmond 1965). The Douglas Creek

Arch is a faulted anticline that is related to the Douglas Creek fault zone that dates back to the Precambrian times. These faults are an example of features that were reactivated during the Laramide orogeny (Bader, 2009). The Douglas Creek Arch was also active during the Paleocene as evidenced by the lapping out of Paleocene age sediments near the arch on the regional Cretaceous-Paleogene unconformity (Johnson and May, 1980). The Uncompahgre uplift, which formed during the Pennsylvanian, was also structurally rejuvenated from the Maastrichtian into the Cenozoic, thus forming the southeastern margin of the basin (Osmond, 1965; Johnson, 1985). The San Rafael Swell makes up the southwestern boundary of the Uinta Basin and is an anticline that formed in response to subsidence of surrounding areas. The San Rafael Swell initially emerged around the latest Campanian (Fouch et al., 1983). During the Paleocene and Eocene, the Uinta Mountains experienced punctuated episodes of uplift and the synclinal axis of the basin became re-located toward the north, resulting in near vertical dips of pre-Cenozoic strata just south of the Uinta Mountains (Osmond 1965; Osmond 2003). The Uinta Mountains thus outline the northern portion of the basin's rim. The orientation of the Basin Mountain boundary fault, which is located along the southern margin of the Uinta Mountains, closely approximates the trend of the Precambrian Uinta Mountain trough and may evidence the rejuvenation of structures associated with this feature (Johnson, 1992). Also, the Douglas Creek Arch, which formed during the late Cretaceous, was reactivated and uplifted into a topographic high, thus delineating the eastern most boundary of the Uinta Basin and the western boundary of the Piceance Creek basin. The axis of this structure was truncated by the uplift of the Uinta Mountains (Bader, 2009). These newly created tectonic uplifts and reactivated uplifts, such as the Uinta Mountains, the Uncompahgre

uplift, and the San Rafael Swell, were the primary sediment sources for the rapidly subsiding Uinta Basin (Birgenheier and Vanden Berg, 2011). Lacustrine deposition was concentrated in the central part of the basin during the deposition of the Wasatch, Green River, and lower Uinta Formations. Fluctuations in the tectonic regime and the sediment supply gave rise to a complex intertonguing of oil shale and alluvial sediment (Osmond, 1965).

### *Uplift During the Miocene*

Toward the end of the Cenozoic during the later Miocene, the Colorado Plateau experienced regional uplift, which gave rise to the post-Laramide landscape. Many researchers (Johnson and Nuccio, 1986; Sweeney et al., 1987; Anders et al., 1992; Johnson and Nuccio, 1993; Ruble et al., 2001; Nuccio and Roberts, 2003; and others) agree that major uplift and down cutting occurred in the Uinta-Piceance region within the last 10 Ma. Maps of Gable and Hatton (1983) indicate that the entire region experienced approximately 6500 – 10000 ft (1981 – 3048 m) of uplift during this time. In the adjacent Piceance Creek basin, downcutting of the Colorado River of 5,000 ft (1524 m) has occurred and the timing associated with the initiation of down-cutting is constrained by 9.7 Ma basalts that cap the remnants of the pre-uplifted surface (Johnson and Nuccio, 1986). Hunt (1969) suggested that by the end of the Miocene, the present day drainage pattern was established for the Colorado River. The estimated 6500 – 10000 ft (1981 – 3048 m) of uplift for the Colorado Plateau may be attributed to dynamic topography (Moucha et al., 2009; Liu and Gurnis, 2010) and static thermal uplift in response to removal of the Farallon slab (Bird, 1984; Beghoul and Barazangi, 1989; and Roy et al.,

2009). As a result, the Uinta Basin has experienced uplift and likely over 3300 ft (1000 m) of erosion (Osmond, 2003).

***Summary***

The present-day geometry of the Uinta Basin is dominantly dictated by Cenozoic tectonics and partially controlled by pre-existing structures (Osmond 1965). Compressive stresses of the Laramide orogeny gave rise to newly formed uplifts and rejuvenated older features that formed the boundaries of the Uinta Basin. The basin's northern margin was formed when the Precambrian Uinta Mountain group was reactivated and uplifted in the Eocene to form the Uinta Mountains (Osmond, 1965). The formation of its eastern margin was dictated by the Cenozoic rejuvenation of the stable Douglas Creek arch, which originally emerged in the Late Cretaceous (Bader, 2009). The basin's southeastern margin is controlled by the Late Cretaceous through Cenozoic reactivation of the Uncompahgre block, which originally formed during the Pennsylvanian (Osmond, 1965). The basin's southwestern margin is formed due to the San Rafael Swell, a Cenozoic anticline. In essence, during the Cenozoic, the boundaries of the Uinta Basin formed due to varying rates of uplift between the basin's center and its margins driven by Laramide compressional stresses.

## 2.3 Evolution of the Lake Uinta Depositional System

South of the Uinta Mountains, Lake Uinta was the internally drained depositional center that now contains the Cenozoic rocks of the Uinta Basin. Intervals of the Green River Formation are made up of sediments that were deposited within this ancient lake

system (Fouch et al., 1994). Following the retreat of the Cretaceous Interior Seaway, deposition of clastic continental facies (North Horn, Colton, and Wasatch Formations) occurred during the early Cenozoic. Subsequently, the joining together of several freshwater lakes resulted in a large period of lacustrine deposition during which the Eocene Green River Formation was deposited. During this time of deposition, lake level continually fluctuated which gave rise to a complicated intertonguing of lacustrine and fluvial deposits (Ruble et al., 2001). Deposition from the surrounding highlands into the Uinta Basin evolved over time as conditions changed in and around the basin (Ruble et al., 2001). Subsidence rates, sediment supply, climate, and eustasy controlled sedimentation in the Uinta Basin. During times of high subsidence rates, clastic sediments were restricted to narrow zones nearby tectonic highs, whereas distal portions of the basin received input of fine grained clastics interbedded with evaporites. Deposition of carbonates is also associated with times of rapid subsidence, low sediment supply, and high lake level. Periods of tectonic stability gave rise to alluvial clastics, eolianites, or carbonates. Alluvial and eolian deposition occurred during times of humid and arid climates, respectively (Johnson, 1992). The evolution of Lake Uinta was largely dictated by changes in climate and tectonically driven alterations in the basins geometry. Water chemistry and lake level were particularly sensitive to these changes because Lake Uinta was internally drained with no external outlet. As a result, changes in climate and tectonics were the primary vehicle for the deposition and preservation of source, reservoir, and seal rocks (Fouch et al., 1994). The Green River Formation has recorded long and short-term fluctuations in climate and tectonic activity. For example, faulting may have induced large expansions of the lake, which would result in the deposition of

thick discrete stratigraphic sequences and oil shale. Shorter-term changes also modulated the lake level, water chemistry, and the depositional patterns and are primarily climate controlled. In kerogen rich oil shales, climate induced cycles gave rise to fluctuations in the amounts of carbon and oxygen. Changes in carbon and TOC record variations in the productivity of organic material and the amount of reduced carbon available for the precipitation of carbonates. As a result, deposition within Lake Uinta is characterized by carbonate geochemical and sedimentary parasequences (Fouch et al., 1994). In the following section, the transition from freshwater to saline Lake Uinta will be discussed, and the depositional environment associated with the intervals of interest of this study will be described.

***Formation of Freshwater Lake Uinta***

Downwarping associated with the latest phases of the Sevier orogeny and the initial stages of the Laramide orogeny gave rise to a transitional sedimentary basin in the central and western Uinta Basin area and toward the south in between the Sevier orogenic belt and the San Rafael Swell (Spieker, 1946; La Rocque, 1960; and Johnson, 1985). Toward the west, this basin's geometry was dictated by post thrusting motion along the Sevier orogenic belt and toward the east, the basin's geometry was dictated by Laramide uplifts (Stanley and Collinson, 1979). Multiple lakes were likely present in the central portion of this basin from the Maastrichtian to the late Paleocene (Fouch et al., 1983). Throughout the Paleocene, this basin expanded until the outline of the Uinta sedimentary basin was formed. Sometime in the late Paleocene, the smaller lakes combined to form a larger lake known as Lake Flagstaff. Prior to the end of the Paleocene, Lake Flagstaff

expanded to a point in which it was in close proximity with the Douglas Creek arch. During this time, the Uinta and the adjacent Piceance Creek basins are believed to be isolated hydrologic basins. Between the late Paleocene and the early Eocene, inward deposition of large packages of fluvial and alluvial mudstone and sandstone occurred from the basins margins. It is possible that the growth of alluvial depositional environments during this time was initiated by rejuvenated tectonic uplift or short-term changes in climate (Johnson, 1985; Fouch et al., 1994). By the early Eocene, the depositional environment within the Uinta Basin was characterized by fresh water lakes. Expansion of fresh water lacustrine deposition may have created a connection between the hydrologic systems of the Uinta and Piceance Creek Basins. Within the Uinta Basin, lakes coalesced and southward expansion along the Sevier orogenic belt occurred until the lake occupied a large portion of area formerly occupied by Lake Flagstaff. This expansion can be considered the initial phase of Lake Uinta (Johnson, 1985).

***Transition to Saline Lake Uinta***

The stratified lake model of Bradly and Eugster (1969) suggests that Lake Uinta was separated into a highly saline, reducing, and bicarbonate rich underlying layer and a less saline overlying layer that was oxidizing. In the stratified model, planktonic algal blooms would occur sporadically in the overlying layer where they would exploit carbon dioxide. This resulted in the precipitation of calcium carbonate. Calcium carbonate and decaying organic material would then drift through the water column to the bottom of the lake, giving rise to carbonate and organic rich deposits. As the organic material settled, carbon dioxide was generated at the expense of the available oxygen and used in the

precipitation of bicarbonate minerals, which are interbedded with the oil shale deposits (Johnson, 1985).

The transition from freshwater to Saline lake Uinta began during the Eocene when the lake experienced a period of major expansion that is termed the Long Point transgression (Johnson, 1985). During this time, Lake Uinta expanded to the structural features that delineate the basins margins, thus covering a much larger area than ever beforehand. Abundant deposition of limestone and carbonate-rich mudstone occurred as a result of the transgression. Carbonate deposition was limited to areas with low rates of clastic input, such as the southwestern portion of the basin. Furthermore, organic-lean, clay-rich oil shale was deposited and the oil shale depocenter expanded. Additionally, widespread sandy marginal lacustrine shelves formed in zones with high clastic input once maximum transgression was reached. During this time, Lake Uinta transitioned from an open hydrologic system into an internally drained, closed hydrologic system. This is evidenced by a lack of freshwater fauna, accelerated carbonate production, and an increase in the richness of oil shale deposits (Johnson, 1985; Fouch et al., 1994).

The next phase of saline Lake Uinta evolution involved a marked increase in the richness of deposited oil shales. The depositional environment was organically productive and the hydrologic system was closed as evidenced by the presence of oil shale deposits rich in carbonate minerals of biological origins (Fouch et al., 1994). Oil shales were still clay-rich during this phase. Generally, sediments deposited during this phase of lake evolution were thicker and more diluted by clastics. Clastic sedimentation alternated between periods of rapid and slow deposition, which resulted in the deposition

of alternating rich and lean zones. Lake Uinta regressed and transgressed during periods of rapid clastic sedimentation and oil shale deposition, respectively (Johnson, 1985).

The next phase is marked by another change in the depositional character. During the middle Eocene, Lake Uinta rose to its maximum and deposition of the Parachute Creek Member of the Green River Formation began (Ruble et al., 2001). A transition to more carbonate-dominated deposition in both open and marginal lacustrine depositional environments occurred (Johnson, 1985). This portion of lake evolution spans the deposition of the lower intervals of the Parachute Creek Member, which include the GG2, L2, GG1, and L3 rich and lean zones. These intervals are characterized by interbedded clay-rich and carbonate-rich oil shale. The newly emergent carbonate-rich oil shale is a fine-grained rock with 50% carbonate or more with minor sandstone and siltstone. In marginal lacustrine areas, the transition from clastic-rich to carbonate-rich deposition was less pronounced due to higher rates of clastic input (Johnson, 1985).

The next phase of development is marked by another transgression that occurred stratigraphically at the base of the GG-rich oil shale interval. Deposition associated with this phase extended to the base of the Mahogany oil shale and included the rich zones of the GG, GG0, and R6 of the Parachute Creek Member. During this time, oil shale deposition expanded beyond the outer portion of the marginal lacustrine areas. Also, sandstone and siltstone intervals extended to the oil shale depocenter, giving rise to well laminated organic-lean zones. As a result, the rich oil shale zones are interbedded with lean zones containing mudstone, sandstone, and siltstone. Kerogen content in the oil shale depocenter greatly increased during this phase and exceeded the amount of kerogen deposited during the earlier stages (Johnson, 1985).

The final stage of saline Lake Uinta evolution involved yet another transgression. This transgression began stratigraphically at the upper R6 and resulted in the expansion of oil shale deposition to the whole area previously associated with marginal shelves. Next, volcaniclastics were deposited around the outer portions of the Uinta Basin but did not make it to the oil shale depocenter. Lake Uinta continued to be present in the central and western portions of the basin until around the late Eocene. Deposition of sandstone, silt, lacustrine marlstone, shale, and oil shale continued until the end of the Eocene when clastics sourced from adjacent Laramide uplifts became the dominant type of sediment that filled in the basin (Johnson, 1985). At this time, the lake became filled with coarse-grained clastics that comprise the Uinta Formation, Duchesne River Formation, and Bishop Conglomerate. Clastic deposition continued until the Oligocene or Miocene (Abbott, 1957; Untermann and Untermann, 1964).

# CHAPTER 3: Methods

## 3.1 Methods

A basin modeling analysis can give insight into the thermal and uplift/subsidence history of a basin. This type of information is crucial for determining if the upper petroleum system of the Green River Formation has been buried to sufficient depth and experienced sufficient temperatures to generate hydrocarbons, and if so, at what locations within the basin this may have occurred. Building two-dimensional (2-D) basin models requires an extensive list of input parameters, in addition to measured data, such as vitrinite reflectance and Rock-Eval measurements which are necessary for model calibration. In this study, models are generated from well logs using the BasinMod 2011

and BasinMod 2D software packages (Platte River Associates). BasinMod 2011 is a software package that allows the user to reconstruct burial histories and estimate a basin's thermal history in order to evaluate the hydrocarbon potential at a single well location. A wide range of other values may be calculated as well, such as maturity, porosity, permeability, pressure, and temperature (Platte River Assocaites, 2012). BasinMod 2D allows the user to construct a gridded 2-D cross section from which values are calculated in cells within the calculation grid based on a forward modeling approach. Parameters such as temperature, pressure, maturity, and hydrocarbon generation can be displayed over different time steps across a 2-D section. In order to better understand how the Uinta Basin's tectonic history and thermal structure influenced the maturity of source rocks within the middle to upper Green River Formation, 60 1-D models are constructed along three sections that span from the Greater Monument Butte to the Altamont Bluebell oil fields. From these 1-D models, three 2-D models will be constructed from north to south along sections A-A', B-B', and C-C'. The location of the three cross sections is shown in Figure 4.

In order to evaluate various model-calculated parameters, such as the thermal maturity of a source interval, the modeling software must predict the maximum burial depth of a rock interval. Calculating maximum burial depth is crucial because this directly impacts the temperatures and pressures a rock interval experiences over time. The total amount of subsidence a basin experiences is a combination of both the subsidence due to tectonic activity and the subsidence induced by the loading of sediments. The model-predicted theoretical subsidence curve is calculated based on the user-defined lithologies, age assignments, and erosional events by systematically

decompacting the sediments. This process, known as backstripping, involves removing the effect of a sediment load on the total subsidence of a basin to obtain tectonic subsidence (Baur et al., 2009). This process assumes Airy isostacy and adjusts for isostatic rebound. Once each layer is decompacted and isostatically balanced, in order to calculate the length of accommodation created if a sediment package were replaced with a column of water, the tectonic subsidence curve can be obtained. The equation used to calculate the depth of the basement corrected for the sediment load is (Steckler and Watts, 1978):

$$Y = S\left(\frac{\rho_m - \rho_s}{\rho_m - \rho_w}\right) - \Delta SL\left(\frac{\rho_w}{\rho_m - \rho_w}\right) + \left(W_d - \Delta SL\right)$$

where:

$Y$ = basement depth corrected for sediment load

$S$ = thickness of sediment column corrected for compaction

$\rho_m$ = mantle density

$\rho_s$ = sediment density

$\rho_w$ = water density

$\Delta SL$ = change in elevation of sea level

$W_d$ = paleo sea depth

### 3.2 Building the Framework

When building basin models, the first step involves constructing the framework upon which the basin models will be built. The framework consists of a series of correlated well logs along the three north-south sections discussed above. This is

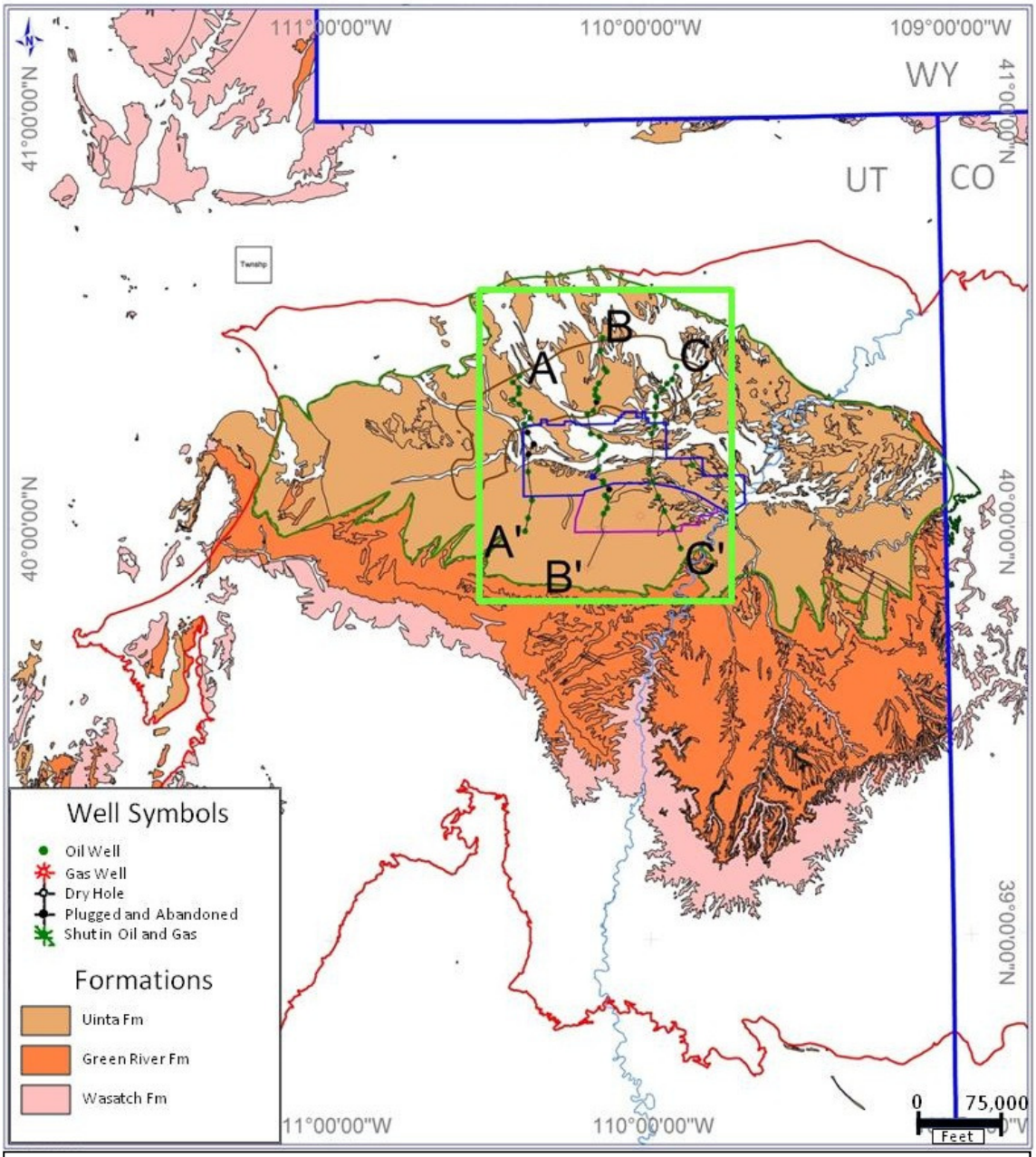


***Figure 4***: Map showing the location of the three lines of section that are used to generate the 2-D models. The three north to south trending lines are composed of sixty wells. The red line is the greater Uinta-Piceance province, the brown line is the Altamont Bluebell oil field, the blue line is the Central Basin oil field, the purple line is the Greater Monument Butte oil field, and light green box shows the extent of the study area.

necessary in order to extract the depths and thicknesses of the intervals of interest across the basin so they can be imported into the modeling software. The software package IHS Petra (IHS, 2012), where well log data can be stored and populated, is used to build the framework. Wells are selected based on the geophysical logs available, the depth to which the data were logged, and their position with respect to the locations from which measured data is available. Wells that possess gamma ray, induction, and density logs allow for easier picking of the intervals of interest based on characteristic responses of these logs. The depths from which data were logged must span stratigraphically from above the Mahogany to the basal interval of the Garden Gulch. In addition, wells were selected based on the location of control points from which measured data is available. If a section is not able to go directly through a well with measured data, it is positioned as close as possible to that well while maintaining a north to south trend. Wells fitting the above data criteria are picked in a fashion that yields three north-south sections that cover the major oil fields in the study area. All well data used are courtesy of the database of Newfield Exploration. The three correlated sections are shown in plates 1-4.

The next step is to pick the formation tops associated with each of the rich and lean zones of the Parachute Creek Member in each of the wells that compose the framework sections. Tops are picked based on characteristic signatures of geophysical logs that are unique to each zone. Once this is completed, well information (name, ground elevation, and API) and depths are exported into a spreadsheet for easy data entry once the model-building phase begins.

### 3.3 Inputs Required for 2D Models

#### *1) Lithologies*

Lithologies of the intervals of interest must be assigned at each well location. Lithologies are important to constrain as accurately as possible because they affect other modeling parameters, such as the reduction of porosity with depth, permeability, and the thermal conductivity of the rocks, which in turn will impact maturity and hydrocarbon generation. BasinMod 1-D possesses a library of eight pre-built pure lithologies and corresponding rock property values that are used in calculations. Some of these rock properties include initial porosity, compaction behavior, density, grain size, thermal conductivity, and heat capacity (Platte River Associates, 2012). In the real world, formations can rarely be described by a single, pure lithology. For this reason, BasinMod 2011 and BasinMod 2-D allow the user to generate custom lithology mixes by identifying percentages of lithologic components such as sandstone, siltstone, shale, dolomite, and limestone. When a custom lithology is created, the program automatically calculates the rock properties that correspond to the new lithology via interpolation from the pure lithology values. In addition, BasinMod 2011 allows the user to create lithologies based on mineral composition. In this case, the user can define lithologies based on percentages of component minerals and the grain size of each mineral. Although this method provides more detailed lithologies, rock properties, and takes into account the degree of sorting, sufficient data is not available to describe lithologies in this fashion. For this reason, lithologies were constrained as best as possible by building on previous researchers descriptions and using the mixing option.

The Uinta Formation, Duchesne River Formation, and the Bishop Conglomerate are represented jointly by the uppermost layer in the models. The Uinta and Duchesne River Formations represent the fluvial and lacustrine units that were deposited during the latest stages of subsidence in the Uinta Basin (Johnson and Nuccio, 1993). The Uinta Formation is present in outcrop through a large portion of the central Uinta Basin and is dominantly composed of sandstone, siltstone, and mudstone, which was deposited within lacustrine, marginal lacustrine, and fluvial environments. The Duchesne River Formation is dominantly a fluvial unit composed of mudstone enclosed within sandstone bodies (Johnson and Nuccio, 1993). Ryder et al. (1976) describe the Uinta and Duchesne River Formations as coarse alluvial sediments. As a result, these upper intervals were assigned a lithology dominantly composed of sandstone with minor amounts of siltstone.

Many researchers (Ryder et al., 1976; Dyni et al., 1985; Birgenheier and Vanden Berg, 2011; and others) have highlighted the presence of evaporite beds within the upper most portion of the Green River Formation. Subsequent to the deposition of the intervals possessing the richest oil shale of Lake Uinta, the lacustrine environment entered a hypersaline phase that resulted in the deposition of evaporites on top of the organic-rich carbonate oil shales (Ryder et al., 1976). Core drilling around the southwestern portion of the basin within Duchesne County has revealed multiple beds of mixed halite and sodium carbonate salts that are up to 19 ft (5.8 m) thick within the uppermost portions of the Green River Formation (Dyni et al., 1985). Correlated cross sections of Birgenheier and Vanden Berg (2011) illustrate the presence of these saline facies within the middle to upper most portion of the R8 zone just beneath the Uinta Formation. In the models of this study, the saline zone is combined with the upper Green River Formation and is

considered a separate interval from the underlying R8 zone. Birgenheier and Vanden Berg (2011) describe the middle and upper R8 as evaporite bearing carbonate mudstone and volcaniclastic sandstone. As a result of this previous work, the upper Green River Formation was assigned a lithology that consists of sandstone and carbonate with evaporites.

Stratigraphically between the upper Green River Formation interval just described and the fluvial-deltaic Douglas Creek Member, are the carbonate-dominated rich and lean zones that make up the Parachute Creek Member (Ryder et al., 1976). Within the Parachute Creek Member, organic-rich and lean zones are alternately stacked. The Mahogany oil shale (R7) is the most organic-rich zone associated with this interval. Lithologies of this interval were largely inferred based on the core and XRF data of Birgenheier and Vanden Berg (2011). Their XRF data suggests that the oil shale intervals are largely composed of clay minerals and dolomite below the base of the Mahogany zone and transition to more calcareous oil shale above the base of the Mahogany zone. Particularly, their data indicate that the R8 is made up of calcareous mudstone with some sandstone, the R7 is made up of organic-rich calcareous mudstone (oil shale), and the rich zones spanning from the R6 down to the GG2 are made up of organic-rich dolomitic mudstone (oil shale). In the Uinta Basin, higher rates of clastic input are associated with the deposition of the GG1 and GG2 rich zones (Johnson, 1985). Gamma ray signatures from well logs along the three lines of section indicate a trend that is consistent with increased clastic influence closer to the Uinta uplift toward the north. In an attempt to capture this trend, the carbonate content associated with the rich zones was approximated by systematically increasing it from the north toward the south where intervals are closer

to the oil shale depocenter. XRD data from Norling 1-9B1, which is located in the east-central portion of the study area, indicates that the carbonate content for the Mahogany and overlying A-Groove is about 50% or greater. Toward the south, data from Murphy 2-31-3-2W indicates that carbonate content increases up to 80 percent in the rich zones of the Parachute Creek Member.

The lean zones sandwiched in between the rich zones were deposited as a result of clastics reaching the oil shale depocenter during periods of heightened weathering and sediment production that is likely induced by changes in climate. Lean zones spanning from the B-Groove down to the L2 are composed of organic lean clay-rich mudstone that contains sandstone, siltstone, and shale (Johnson, 1985; Birgenheier and Vanden Berg, 2011). As a result, the lean zones are assigned various mixtures of dolomite, sandstone, and shale to reflect as best as possible the lithologic descriptions associated with the core data of Birgenheier and Vanden Berg (2011). The above lithologies are constrained with the available geologic data and are considered reasonable until future studies warrant more detailed data. Table 1 shows the best approximation for the lithologies that are used in the models.

***2) Compaction Behavior and Porosity***

Initial porosities of each interval are calculated based on the percentages of different pure lithologies assigned to each interval. Initial porosity is calculated via interpolation between the initial porosity values of several pure lithologies that comprise a custom mixed lithology. The degree to which porosity is reduced with continued deposition and burial is important when modeling because this will influence a rock

**Table 1**: Generalized lithologies used to construct burial histories and 2-D models.

| Interval Name | % Sandstone | % Siltstone | % Shale | % Limestone | % Dolomite | % Evaporite |
|---|---|---|---|---|---|---|
| Uinta and Duchesne River Fm | 90 | 10 | 0 | 0 | 0 | 0 |
| Upper Green River | 66 | 0 | 0 | 24 | 0 | 10 |
| R8 | 17-40 | 0 | 18-40 | 20-65 | 0 | 0 |
| A Groove | 10 | 0 | 30 | 0 | 60 | 0 |
| R7 | 17-40 | 0 | 18-40 | 20-65 | 0 | 0 |
| B Groove | 35 | 0 | 50 | 0 | 15 | 0 |
| R6 | 17-40 | 0 | 18-40 | 0 | 20-65 | 0 |
| L5 | 25 | 0 | 50 | 0 | 25 | 0 |
| GG0 | 10-17 | 0 | 10-18 | 0 | 65-80 | 0 |
| L4 | 25 | 0 | 65 | 10 | 0 | 0 |
| GG | 15-22 | 0 | 15-23 | 0 | 55-70 | 0 |
| L3 | 0 | 0 | 90 | 0 | 10 | 0 |
| GG1 | 34-41 | 0 | 34-42 | 0 | 17-32 | 0 |
| L2 | 0 | 0 | 50 | 0 | 50 | 0 |
| GG2 | 34-41 | 0 | 34-42 | 0 | 17-32 | 0 |

interval's thermal history. Dykstra (1987) compared uncorrected burial history curves with burial history curves corrected for compaction and found that source rock intervals will experience greater subsidence rates when corrected for compaction and therefore, earlier timing of petroleum generation. BasinMod 2011 and 2-D both offer multiple mechanical compaction options that determine how porosity is reduced with depth. These methods are developed from data that describes how porosity changes with depth from specific basins or for specific lithologies (Platte River Associates, 2012). The underlying assumption for mechanical compaction is that the thickness of a deposit is reduced by some predictable amount that is dictated by lithology and burial depth. In this study, different mechanical compaction methods are tested and compared with porosities extracted from neutron density logs. The mechanical compaction method that predicts a porosity reduction trend that best fits the measured porosity data is used. Although

porosity values determined from the logs are scattered, the exponential porosity reduction method of Sclater and Christie (1980) best fit the general trend determined from neutron porosity logs. Figure 5 shows porosity with respect to depth predicted by the exponential method compared with measured porosity from logs at three wells from the central portion of the study area.

The exponential mechanical compaction method of Sclater and Christie (1980) is derived from the study of Cretaceous chalks, Paleocene sands, and Cenozoic shales from the Central Graben of the North Sea. These sediments exhibited an exponential increase in thickness with shallower burial depth. In this method, porosity varies with depth by the equation (Sclater and Christie, 1980):

$$\phi = \phi_0 \exp^{(-Kz)}$$

where:

$\phi$ = porosity

$\phi_0$ = initial porosity

K = compaction factor (lithology dependent)

z = depth

Initial porosities and compaction factors determined from their study of North Sea lithologies are:

| **Lithology** | **Initial Porosity ($\phi_0$)** | **Compaction Factor (K)** |
|---|---|---|
| Shale | 0.63 | $0.51 \times 10^{-5}$ / cm |
| Sand | 0.49 | $0.27 \times 10^{-5}$ / cm |
| Chalk | 0.70 | $0.71 \times 10^{-5}$ / cm |
| Shaley sand | 0.56 | $0.39 \times 10^{-5}$ / cm |

*(Sclater and Christie, 1980)*

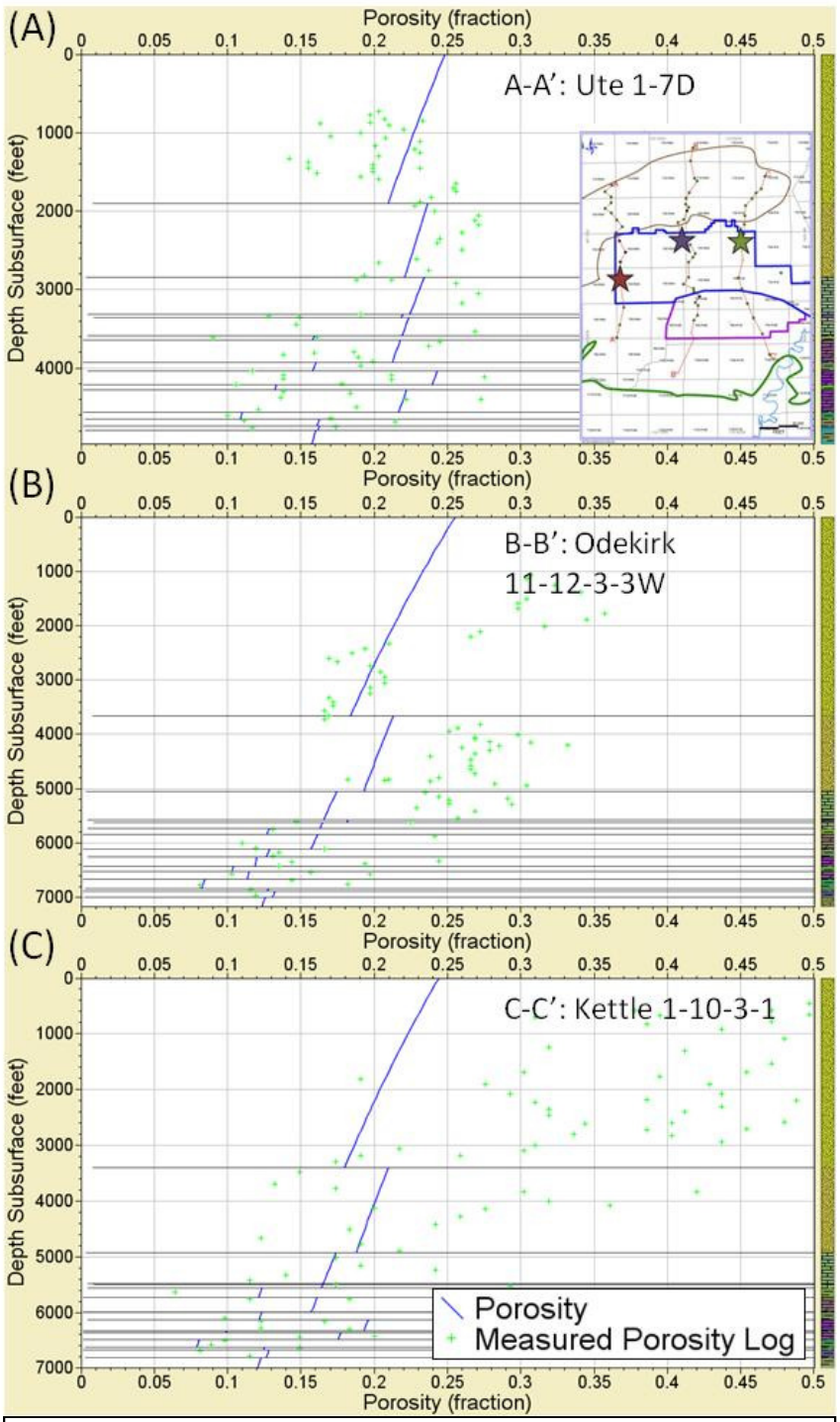


***Figure 5***: Measured porosity with respect to depth compared with model-predicted porosity at wells Ute 1-17A (A), Odekirk 11-12-3-3W (B), and Kettle 1-10-3-1 (C). Thumbnail map in 5a shows the locations of Ute 1-17A (red star), Odekirk 11-12-3-3W (purple star), and Kettle 1-10-3-1 (green star).

***3) Permeability***

Permeability characterizes the ability of a porous media to transmit fluids. Flow through porous media can be characterized by Darcy's Law, which is expressed by the equation:

$$v = \left(\frac{-k\rho g}{\mu}\right) \times \left(\frac{dh}{dl}\right)$$

where: $v$ = Darcy velocity

$k$ = permeability

$\rho$ = density

$g$ = acceleration due to gravity

$\mu$ = viscosity

$\frac{dh}{dl}$ = hydraulic gradient.

In BasinMod 2-D, the Power Function and the modified Kozeny-Carman equation are the two methods the user may select to calculate permeability. These methods are non-linear functions that relate permeability and porosity. Generally, changes in permeability occur logarithmically with linear changes in porosity (Platte River Associates, 2012). The Modified Kozeny-Carman method requires data not possessed for calculations of permeability. As a result, the default Power Function is used in order to calculate permeability. This method relies on void ratios to determine permeability and is represented by the equation from Lerche (1990):

$$k = k_1\left(\frac{e}{e_1}\right)^C$$

where:

$k$ = permeability

$k_1$ = initial permeability

$e$ = void ratio; ( $\phi$ / 1 – $\phi$)

$e_1$ = initial void ratio

C = permeability power (lithology dependent)

***4) Thermal Conductivity***

The thermal conductivity of a rock interval characterizes that interval's ability to conduct heat. Thermal conductivity is an important input variable because it affects the model calculated geothermal gradients. Thermal conductivity is influenced by the matrix conductivity (determined by user assigned lithologies), fluid conductivity (assumed to be water), porosity (determined from the burial history), and temperature (determined by user specified heat flow values). The total conductivity of a rock is determined by calculating the matrix conductivity (assuming no porosity and no pore fluids) and the fluid conductivity (Platte River Associates, 2012). Since we do not have access to laboratory measurements of thermal conductivities of Green River oil shales, BasinMod 2-D will calculate matrix conductivity by the equation:

$$k_M = k_0 \exp\left(\frac{C_f}{T} - \frac{C_f}{T_0}\right)$$

where:

$k_M$ = calculated matrix conductivity

$k_0$ = initial matrix conductivity at standard temperature

$T$ = calculated temperature

$T_0$ = standard temperature (273 K)

$C_f$ = correction factor (250)

The thermal conductivity of the fluids is calculated according to Deming and Chapman (1989) and is an arithmetic mean of the fluid conductivity of water, oil, and gas (Platte River Associates, 2012).

***5) Ages***

For the uppermost section of the model, which includes the Uinta Formation, Duchesne River Formation, and the Bishop Conglomerate, only the age associated with the end of significant deposition within the Uinta Basin needs to be constrained since the upper portions of the Green River Formation can be constrained with the Strawberry Tuff (Smith et al., 2008, 2010). Since the top of the modeled section is marked by an erosional surface, it is difficult to estimate when significant deposition ceased. Models of Anders et al. (1992) and Johnson and Nuccio (1993) suggest that significant deposition ceased sometime between 40-35 Ma. Models of Sweeney et al. (1987) and Fouch et al. (1994) suggest that major deposition ceased around 30 Ma. Conversely, models of Ruble et al. (2001) and Nuccio and Roberts (2003) indicate significant deposition ceasing around 20 Ma. A time stratigraphic cross section of Johnson and Johnson (1991) indicates deposition occurred until roughly 25 Ma. Bryant et al. (1989) indicated that deposition of the Duchesne River Formation occurred until 30 Ma or later through dating tuff beds. For this study, the models of Nuccio and Roberts (2003) and Ruble et al. (2001) are followed. Assuming deposition continued until 20 Ma is reasonable given that a large portion of section is eroded. Furthermore, this will provide a more conservative estimation of

maturity because maximum burial depth will be achieved later than previously assumed by earlier models. Furthermore, any uncertainty associated with the timing of maximum burial depth will not result in a large error in the predicted maturity. Tissot et al. (1987) have pointed out that large changes in reaction times do not result in large changes in temperatures and henceforth, maturity.

Ages of the zones of interest within the Parachute Creek Member can be difficult to assign precisely since the deposition of multiple intervals occurred over a relatively small time interval. However, ages can be roughly constrained from known ages of stratigraphic intervals that bound the zones of interest. Smith et al. (2008, 2010) conducted multiple $^{40}Ar/^{39}Ar$ experiments on sanidine and biotite from ash beds within the Uinta and its neighboring basins. The Strawberry tuff is located stratigraphically below the Uinta Formation within the upper most Green River Formation and yields ages of about 44.3 Ma. The Mahogany oil shale zone (R7) is situated in between the Wavy (48.66 Ma) and Curly (49.32 Ma) tuffs, so its age lies somewhere in between these two ages. The yellow tuff yielded an age of 51.55 Ma and is located toward the base of the Parachute Creek Member. However, this age was obtained from the adjacent Piceance Creek Basin, so it will be considered carefully. Remy et al. (1992) determined that the age associated with the base of the carbonate marker, which separates the middle and lower Green River Formation is around 54 Ma. With this framework in mind, we can assume that the rich and lean zones of the Parachute Creek Member were deposited between 44-54 Ma. Ages assigned to each rich and lean zone will be approximated to some age in between 44-54 Ma, however ages can be further constrained by the timing of known Eocene hyperthermal events (in which the lean zones are deposited).

Birgenheier and Vanden Berg (2011) have interpreted the stacked alternating sequences of rich oil shale and lean zones to represent periods of decreased and increased sediment supply, respectively. Birgenheier et al. (2009) investigated the effects of variations in climate on the depositional character within the Green River Formation and concluded that systematic variations in the nature of the organic material and mineralogy of mudrocks may be linked to early Eocene hyperthermal events. Furthermore, Plink Bjorklund et al. (2010) linked changes in the character of channel fill deposits associated with rapid deposition and high avulsion rates to periods characterized by a highly seasonal and flashy climate. They suggest that these periods also represent Eocene hyperthermal events. As a result, the lean zones in the study area can be interpreted to record periods of high sediment supply during hyperthermal events. During these periods, the lake level may have been lower as a result of decreased accommodation associated with heightened sedimentation rates. Furthermore, it is likely that rich zones record deposition during "normal" climate conditions (Birgenheier and Vanden Berg, 2011). If the ages of Eocene hyperthermal events are known and assumed to represent the deposition of lean zones in between the rich oil shales, then a more detailed framework for the ages of the individual rich and lean zones can be constructed.

Sexton et al. (2006) demonstrated that benthic foraminiferal isotope data yields evidence of these hyperthermal events. Their data indicate that these events occur at 52.6 Ma, 50.4 Ma, and 51 Ma. The data show negative excursions in both d13C and d18O indicative of warming events and they believe the trends to be global. For an in depth discussion, see Sexton et al. (2006). Nicolo et al. (2007) have shown that negative carbon isotope excursions, which signify warming events, have also occurred at 53.52, 53.26,

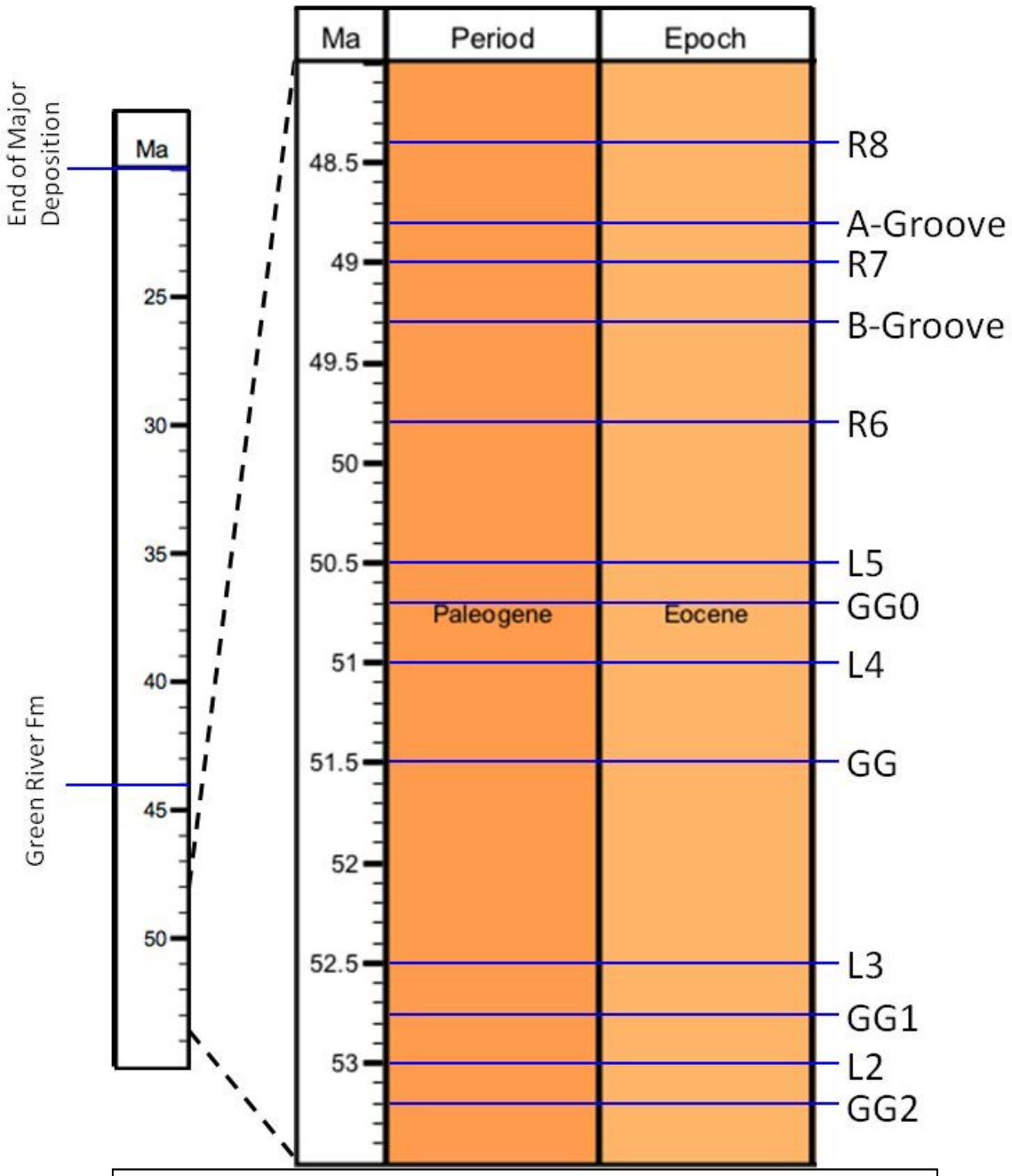


***Figure 6***: Approximated ages used to construct burial histories and 2-D models. Ages are constrained from the known ages of Eocene hyperthermal events, tuff beds, models of previous workers, and time stratigraphic cross sections.

and 53.18 Ma. Starting from the most recent warming event at 50.4 Ma, it is assumed that the L5 lean zone was deposited during this time. Moreover, the L4, L3, and L2 may have been deposited around 51Ma, 52.6 Ma, and 53.18, respectively. Assuming the above age constraints, the yellow tuff, which has been assigned an age of about 51.55 Ma, would then fall stratigraphically between the L4 and L3 and therefore corresponds to our GG (R4) units. It is important to note that the constrained ages of the middle Green River Formation fall within the published age constrains for the documented early Eocene hyperthermal events. From this data, ages are assigned to the intervals of the Parachute Creek Member. Figure 6 illustrates the approximated ages for each interval constrained from the above data.

***6) Erosion and Uplift***

Another input variable that must be determined is erosion. As discussed previously, there is geologic evidence suggesting that a large portion of the stratigraphic section has been uplifted and eroded in the Uinta Basin during the late Miocene. As a result, burial depths of the intervals of interest, determined from well log picks, only characterize the present day burial depth and not the maximum burial depth. Constraining erosion and uplift is crucial to understand the upper petroleum system because the amount of eroded material directly impacts the maximum burial depth and maximum temperatures a source rock experiences. Estimating the amount of overburden removed within the Uinta Basin is made difficult due to the extensive nature of previous downcutting and the alluvial nature of the eroded Uinta and Duchesne River Formations (Sweeney et al., 1987; Johnson and Nuccio, 1993). Furthermore, uplift and erosion have

removed most evidence of any pre-erosional surfaces within the Uinta Basin (Anders et al., 1992). Due to the lack of well preserved surfaces of maximum aggradation, many researchers have utilized a variety of methods that have yielded an assortment of estimations for erosion.

Many different methods have been utilized to estimate erosion. Narr and Currie (1982) studied fluid inclusions within core data from the Altamont area and estimated eroded thicknesses ranging from 1112 – 9482 ft (339 – 2890 m). Sweeney et al. (1987) used the compaction behavior of shale to estimate eroded thickness. They assumed shale porosity and density provide a proxy for maximum burial depth and have suggested eroded thicknesses range from roughly 5000 – 10,000 ft (1524 – 3048 m) throughout the basin. Johnson and Nuccio (1986) and Anders et al. (1992) utilized surfaces that they believe represent the surface of maximum sediment accumulation. As a result, erosion is estimated by simply subtracting present day elevation from the elevation of maximum aggradation. This method yielded eroded thickness ranging from 4000 – 5000 ft (1219 – 1524 m). A final method, utilized by Johnson and Nuccio (1993), involved extrapolation of vitrinite reflectance profiles to reflectance values of 0.20 and 0.30 percent. This method yielded eroded thicknesses ranging from 2300 – 11000 ft (701 – 3352.8 m) from various parts of the basin. They acknowledge that an unacceptably large range in thicknesses of eroded material resulted from this method. In essence, the range of estimated eroded thicknesses is as diverse as the methods used to obtain them. For this study, the estimations of removed overburden, determined from the methods outlined above, will be loosely considered as a guide. Erosion will be best constrained by adjusting it until model predictions match measured thermal maturity indicators. For

example, once reasonable heat flow values are constrained, if model-predicted maturity is lower than measured maturity indicators, erosion is increased until a match is obtained. Alternatively, if model-predicted maturity is too high with respect to measured maturity indicators, the eroded thickness is decreased until a match is obtained. This process will be further discussed in the calibration section.

***7) Heat Flow and Surface Temperatures***

Temperatures increase with burial depth as a result of heat flow from within the earth. Heat flow in a given area can be affected by many factors such as tectonic events, volcanic activity, faulting, groundwater movement, and the thickness and thermal conductivity of rock layers (Anders et al., 1992). When modeling the maturity of a petroleum system, heat flow is arguably one of the most important input variables to constrain. The effects of basal heat flow on oil generation, migration, and accumulation are enormous. An increase of decrease in the user specified heat flow by just 5 $mW/m^2$ largely impacts the spatial extent of source rock maturity. Heat flow within the interior of the Colorado Plateau, which extends north through Uinta Basin, is characterized by low to normal heat flow values (less than 63 $mW/m^2$). Conversely, the western, eastern, and southern margins of the Plateau possess higher heat flow (greater than 80 $mW/m^2$ ) (Swanberg and Morgan, 1985).

Chapman et al. (1984) calculated an average surface heat flow of 57 $mW/m^2$ from thermal conductivities and geothermal gradients deduced from corrected bottom hole temperatures in the study area. Also, their data indicates that heat flow varies from 65 – 40 $mW/m^2$ from the southern to the northern parts of the study area. They attribute this

trend to the highly conductive quartzite of the Uinta Mountains that serves as a heat sink and the circulation of low temperature ground water that has reached significant depths to the north. Anders et al. (1992) mapped geothermal gradients determined from DST fluid temperatures across the Uinta Basin and their data showed a similar trend of increasing heat flow from north to south. They point out that the thermal trend mimics the thickening of organic-rich deposits and agree with the interpretations of Chapman et al. (1984). Swanberg and Morgan (1985) determined heat flow ranges from 39 $mW/m^2$ just north of the study area to 70 $mW/m^2$ or greater south of the study area by analyzing the temperature dependence of quartz solubility in groundwater. They also suggested that very low values could be due the flow regimes of groundwater.

The distribution of Cenozoic igneous rocks is dominantly concentrated around the margins of the Colorado Plateau. However, the area associated with the Uinta Basin does not exhibit this trend. Igneous activity has occurred primarily in the western, eastern, and southern margins of the Plateau during the Cenozoic (Morgan and Swanberg, 1985). Furthermore, low upper mantle seismic velocities, zones of active seismicity, and zones of thinner crust are located in the western, southern, and eastern margins of the Plateau (Morgan and Swanberg, 1985). For these reasons, heat flow values assigned to the models will be constant over time. Although Morgan and Swanberg (1985) have suggested thermal expansion as an uplift mechanism, which would result in increased surface heat flow since the time of uplift, it appears that there is insufficient geologic data to justify changes in modeled heat flow over time and hence, no methodical way to do so. Furthermore, no measurable maturation index can be converted into paleotemperature, so a more indirect approach is used that involves an average paleotemperature (Tissot et al.,

1987). Model-predicted maturity indicators such as transformation ratios and predicted vitrinite reflectance are sensitive to changes in model heat flow values. Therefore, model heat flow values will be adjusted progressively by iteration until measured maturity indicators match with modeled predicted maturity indicators. In conjunction with the burial history reconstructed from backstripping, the simple thermal structure that yields the best match with measured maturity indicators will serve as an "average" paleogradient or thermal hypothesis. In addition, the thermal trends illustrated by the work of Chapman et al. (1984) and Anders et al. (1992) will be used. Lastly, average annual surface temperatures are readily available in online weather databases and suggest an average annual surface temperature of about 50 F.

***8) Kerogen and Kinetics***

Green River oil shales dominantly contain type 1 kerogen that is rich in lipid material and primarily made of crosslinked aliphatic chains (Tissot et al., 1978; Tissot et al., 1987). Type 1 kerogen requires greater temperatures in order to generate hydrocarbons because cracking of C-C bonds requires a larger amount of energy (Tissot et al., 1978). In sedimentary basins, oil and gas is generated due to the conversion of kerogen into hydrocarbons. This process occurs as a result of chemical reactions that are dominantly controlled by temperature and other factors such as pressure and the amount of kerogen available for the reaction. Chemical kinetics, which are unique to each type of kerogen, dictate how much oil and gas is produced and affect maturity indicators such as vitrinite reflectance or parameters measured during pyrolysis. In short, all properties that are measured from kerogen or its byproducts are associated with the continuous change

of its chemical structure. Understanding how kinetic parameters vary depending on kerogen type or composition provides a better framework for interpreting the behavior of different maturity indices, which are all related to kerogen composition, chemical structure, and thermal history (Tissot et al., 1987). As a result, it is important to accurately constrain the kerogen type and its associated kinetics when modeling.

In BasinMod 2011 and BasinMod 2-D, kinetic modeling takes into account the variety of chemical bond types and compositions in the kerogen. This method calculates multiple parallel reactions, each with a unique petroleum potential and reaction rate parameter, which take place as organic material experiences degradation into hydrocarbons. In order to predict the amount of hydrocarbons generated and the maturity of source beds, each reaction possesses its own kinetic parameters and is characterized by the equation (Tissot et al., 1987):

$$\frac{dx_i}{dt} = -k_i x_i$$

where:

$x_i$ = residual petroleum potential of the organic material involved in reaction i

$k_i$ = reaction rate parameter at a given temperature.

The reaction rate parameter is dependent on temperature through the equation:

$$k_i = A \exp\left(\frac{-E}{RT}\right)$$

where:

$k_i$ = reaction rate parameter

$A$ = Arrhenius constant or frequency factor of the reaction

$E$ = activation energy required for bond rupture

$T$ = temperature

$R$ = gas constant.

The allocation of the activation energies, or the relative abundance of the original petroleum related to the reaction, is a direct result of the kerogen composition (Tissot et al., 1987). BasinMod utilizes a 4-component model in which kinetics concurrently convert kerogen into hydrocarbons. Generated oil can also experience secondary cracking into gas and residue. This process affords a practical representation of the complicated progression of chemical reactions that occur during hydrocarbon generation (Platte River Associates, 2012). For this study, type 1 kerogen of Tissot et al. (1987), which is based on the type 1 lacustrine kerogen from Green River shales, will be used in the models. The initial potentials, fractions, activation energies, and frequency factors of this kerogen are shown in Table 2. For a detailed discussion of kinetic modeling, the reader is referred to the work of Tissot et al. (1987).

**Table 2**: Kinetic parameters used to model hydrocarbon generation (Tissot et al., 1987).

| Initial Potential (mg/g org. C) | Fraction (0.0 - 1.0) | Activation Energy (kcal/mole) | Frequency Factor (1/sec) |
|---|---|---|---|
| 4.8 | 0.0056 | 48 | 1.0e+15 |
| 7.6 | 0.0088 | 50 | 1.0e+15 |
| 16.4 | 0.0190 | 52 | 1.0e+15 |
| 22.0 | 0.0255 | 54 | 1.0e+15 |
| 792.0 | 0.9184 | 56 | 1.0e+15 |
| 8.4 | 0.0097 | 58 | 1.0e+15 |
| 11.2 | 0.0130 | 60 | 1.0e+15 |

### 3.4 Building 1-D and 2-D Models

For this study, 60 1-D burial history curves will be constructed from the 60 wells that comprise the three cross sections shown in Figure 4. Subsequently, three 2-D models will be constructed from the 1-D burial history curves in order to estimate uplift and erosion, basin thermal structure, and maturity of source beds at and in between each well along the three cross sections. A brief description of the construction of 1-D and 2-D models will follow.

After the input gather phase, the next step is to construct 1-D burial history curves for each of the wells within a given framework section. At this point in time, data and inputs such as formation tops, ages, erosion, kerogen type, lithology, TOC, and thermal information, are populated together in a table within the modeling software. BasinMod 1-D will then generate burial history curves that are calculated from this data. A burial history curve simply illustrates the depth associated with a given interval over time since deposition. These are quick and easy to build, allow for an initial assessment of the sensitivity of key input parameters, and an assessment of the burial history and timing of generation. In addition, BasinMod 2-D possesses the ability to generate a 2-D model from multiple 1-D model files. After 1D burial history curves are complete for each of the wells within the three lines of section, the 1D models are imported into BasinMod 2-D. Once imported, BasinMod 2-D automatically builds what is termed an initial cross section from which the 2-D models will be calculated. Initial cross sections for A-A', B-B', and C-C' display each zone of interest correlated across a given line of section and its corresponding depth (Figures 7-9). In order to generate 2-D models, the initial cross section is divided into multiple cells in which calculations, such as subsidence and

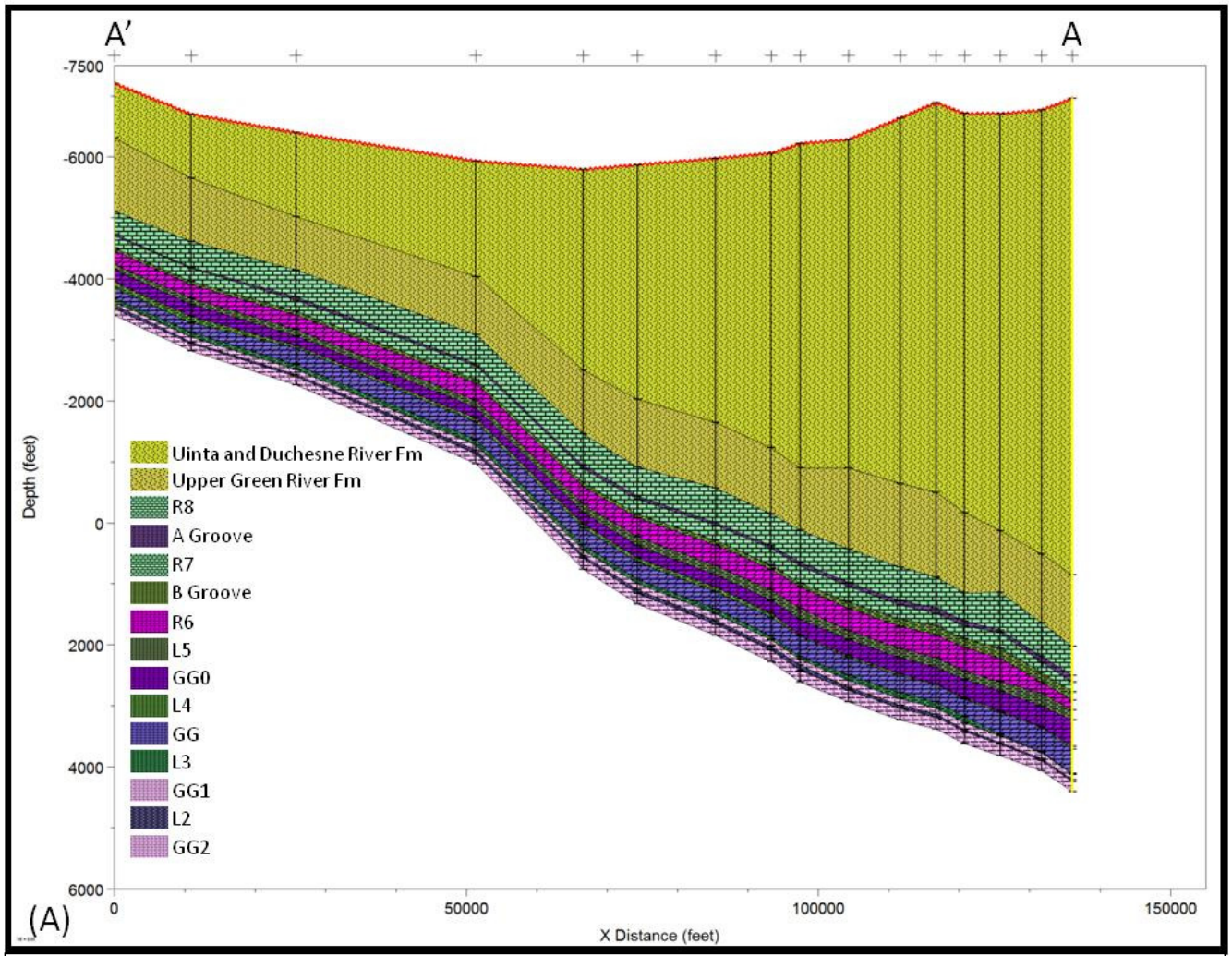


***Figure 7***: Initial cross section produced from the 16 wells that comprise line A-A'. The modeled layers are color coded and the depth scale is subsea.

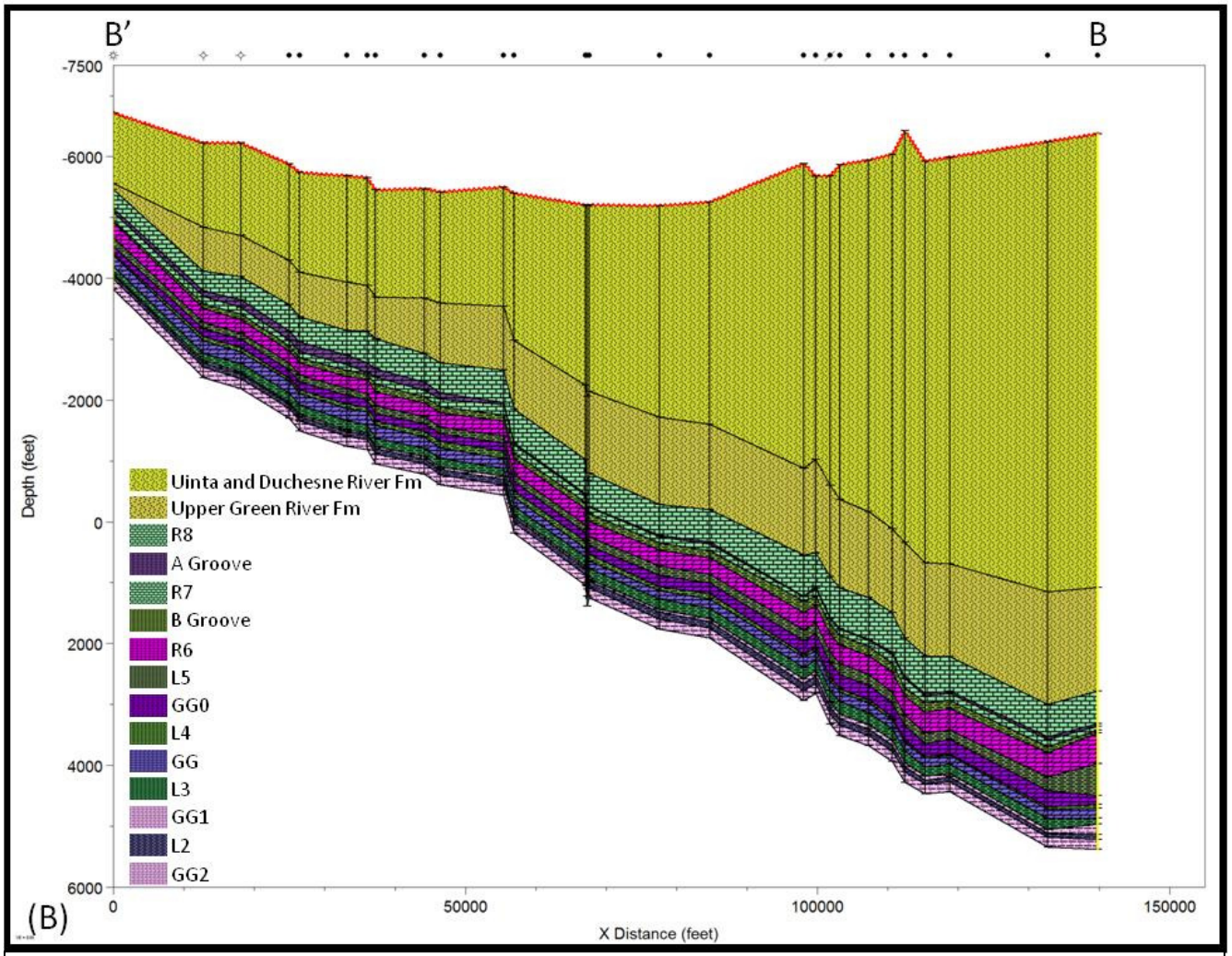


***Figure 8***: Initial cross section produced from the 28 wells that comprise line B-B'. The modeled layers are color coded and the depth scale is subsea.

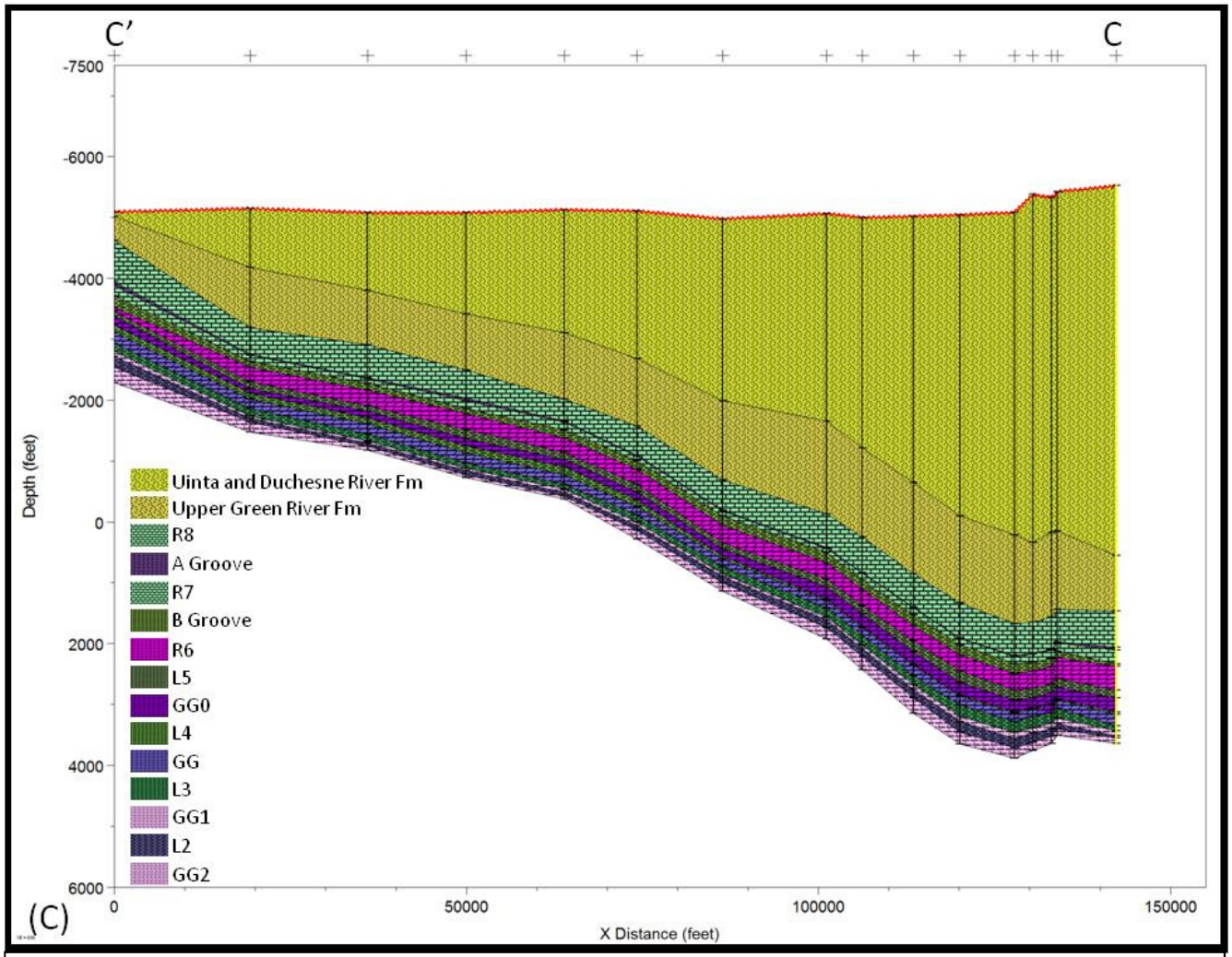


***Figure 9***: Initial cross section produced from the 16 wells that comprise line C-C'. The modeled layers are color coded and the depth scale is subsea.

maturity, will take place. Each initial cross section is divided laterally into 75 cells and vertically into cells that are placed every 5 Ma and at the top and base of each zone of interest.

In order to generate a valid 2D model, three key criteria must be met. The model-predicted vitrinite reflectance versus depth must match reasonably well with measured vitrinite reflectance data, the model-predicted transformation ratios must match up reasonably at the location of the three wells from which measured transformation ratios have been obtained, and the inputs required to obtain these matches must be within geological reason. Once a valid model is generated, conclusions can be made regarding the thermal structure of the basin, the subsidence history, the maturity of the rich zones of the Parachute Creek Member, and the effect of the input parameters. A more detailed discussion of the calibration process follows below.

### 3.5 Measured Data and Calibration

Measurements from Rock-Eval pyrolysis and vitrinite reflectance data will be used to calibrate the 2-D models. Rock-Eval was conducted on samples from three wells located in T3S R2W, T4S R3W, and T3S R1W. Vitrinite reflectance data was obtained from four wells located in T4S R3W, T4S R1E, T9S R17E, and T9S R18E. The locations of these wells are shown in Figure 10. A discussion of the types of data will follow.

Rock-Eval analysis was performed on 244 samples from three wells within the study area (figure 10). Rock-Eval pyrolysis is a technique that is used to quickly investigate the properties of a source rock, such as its generative potential, the quantity of petroleum already generated, the type and quality of hydrocarbons generated, and thermal

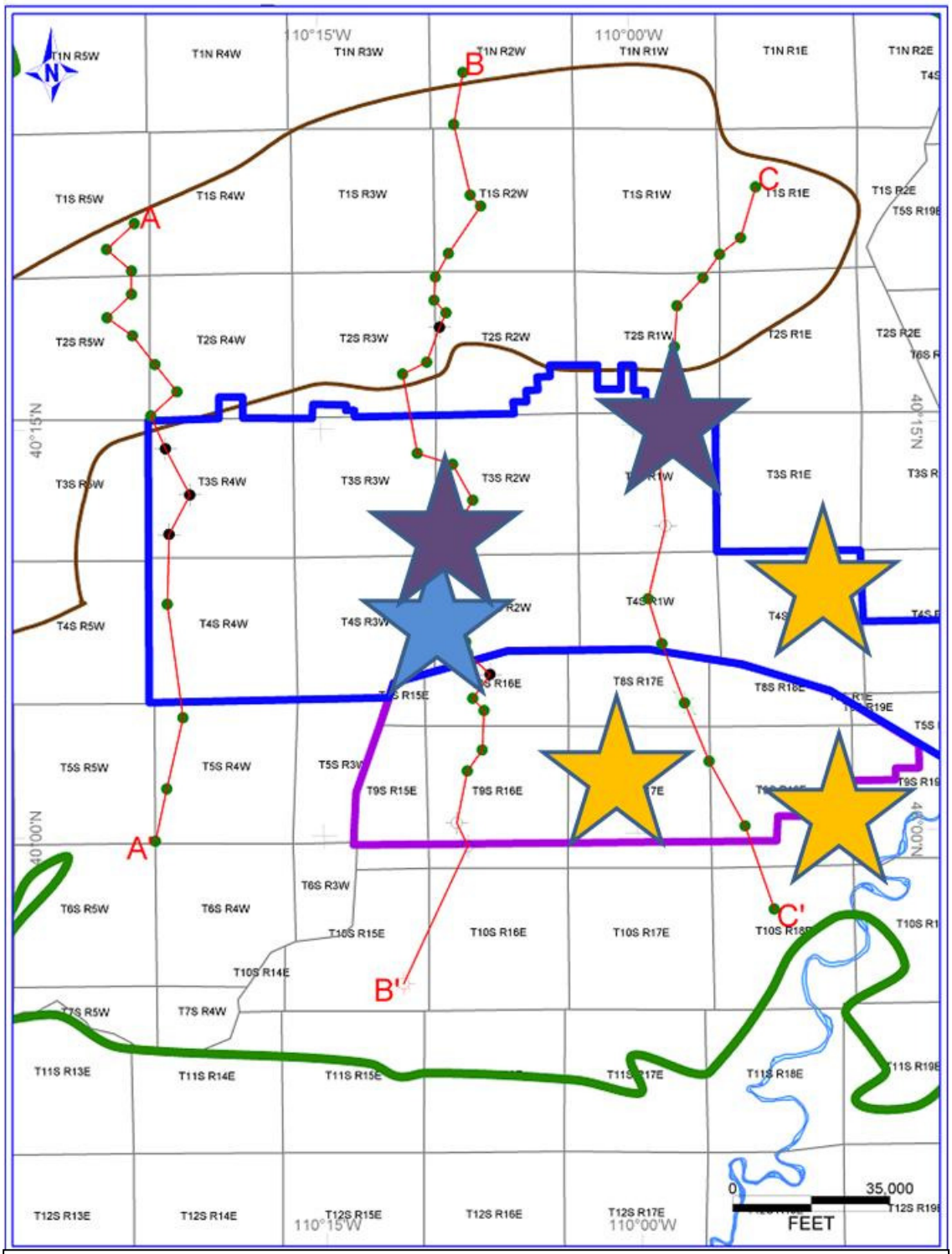


***Figure 10***: Locations of wells from where measured data has been obtained for this study. Orange stars represent locations from which vitrinite reflectance is available, purple stars represent locations from which Rock-Eval pyrolysis is available, and the blue star represent a location in which both vitrinite reflectance and Rock-Eval pyrolysis data are available.

**Table 3**: Total organic carbon (TOC) determined from Rock-Eval pyrolysis on samples from wells shown in figure 10.

| Interval | TOC Min (wt. %) | TOC Max (wt. %) | TOC Average (wt. %) |
|---|---|---|---|
| R8 | 1.24 | 3.30 | 2.28 |
| R7 | 1.07 | 20.40 | 4.89 |
| R6 | 1.20 | 8.81 | 2.75 |
| GG0 | 1.08 | 13.40 | 4.37 |
| GG | 1.04 | 4.59 | 1.75 |
| GG1 | 1.01 | 8.76 | 2.33 |
| GG2 | 1.13 | 4.29 | 2.36 |

maturity. This technique involves heating of the samples in a reaction vessel in order to produce organic compounds. TOC, or total organic carbon is determined from Rock-Eval and is useful for determining the quality of a source rock. Average TOC values from the R8-GG2 are used as model inputs (Table 3). In general, TOC values of the intervals of interest are greater than 1 percent and may reach values of up to 20 percent TOC. Also, Rock-Eval measures other parameters including S1, which describes the amount of hydrocarbons initially present in mg HC per gram sample, S2, which describes the amount of hydrocarbons generated during heating, and S3, which describes the amount of C02 generated (milligrams) per gram sample. Likewise, the production index (PI), also known as the transformation ratio, is calculated during pyrolysis. The transformation ratio is defined as S1/(S1+S2) and describes the ratio of volatile hydrocarbon yield to the total hydrocarbon yield (Nuccio and Condon, 1996). This value can be used to assess the thermal maturity of source rocks because it increases over time with heating and burial. In type 1 kerogen, oil generation generally begins around a transformation ratio of 0.1

(Anders et al., 1992). For this reason, zones along the three cross sections in which the model predicts a transformation ratio of 0.1 or greater will be considered mature. Transformation ratios determined from Rock-Eval will be averaged at each well for each interval of interest and used as a calibration tool. Samples were taken in depth intervals ranging from 10 to 30 ft (3 to 9 m) and the data indicate that measured transformation ratios follow a general trend of increased transformation ratios with depth. However, some minor scatter exists outside of this trend. This occurs because a few samples possess very low TOC percentages and very low S2 values. As a result of uncharacteristically low S2 values, the measured transformation ratio is disproportionately large within some samples, sometimes two or three times more than samples taken 10 ft (3 m) above and below. Therefore, incorporation of these data points results in an inaccurate shift of the average values calculated and would thus overestimate maturity. For this study, these lean zones are excluded from the average transformation ratios calculated for each interval of interest.

Measurements of vitrinite reflectance were also obtained from four wells in the study area: Ute Tribal 15-13-4-3W, Ute Tribal 3-11-4-1E, Beluga 5-16T-9-17, and Federal 15-24-9-18 (Figure 10). Vitrinite is a maceral sourced from woody plant material that frequently occurs in coals and oil shales. Vitrinite reflectance is a measurement of the percentage of reflected light from a polished vitrinite sample. The percentage of reflected light is related to the temperature conditions the sample experienced during burial (Nuccio and Condon, 1996). As a result, vitrinite reflectance is a maturity indicator that covers a broad temperature range from diagenesis through the latest stages of catagenesis and records the maximum temperature a rock experiences during its burial

history (Hunt, 1979; Price and Barker, 1985). In Ute Tribal 15-13-4-3W and Ute Tribal 3-11-4-1E, samples with measured vitrinite reflectance cover the depth range associated with the R8-GG2 intervals. Ute Tribal 3-11-4-1E exhibits nearly a linear increase in % $R_0$ with depth, whereas Ute Tribal 15-13-4-3W exhibits a kink in the trend between 3000 ft (914 m) and 4300 ft (1310.6 m) of depth. The expected increase in % $R_0$ with depth is not observed in this well at this depth range. This change in trend may occur due to the presence of larger than normal quantities of hydrogen within the vitrinite maceral (Price and Barker, 1985). Consequently, care will be exercised when using this vitrinite reflectance data as a calibration tool. The vitrinite reflectance measured in samples from Beluga 5-16T-9-17 and Federal 15-24-9-18 covers depths that exceed the intervals of interest of this study. As a result, the data will be extrapolated to shallower depths where no vitrinite reflectance samples were obtained. The profiles were extrapolated using the methods of Dow (1977), but this resulted in excessive estimated reflectance values at the surface. Particularly, vitrinite reflectance at the surface reached values of just under 1% $R_0$ in Federal 15-24-9-18. As a result, a simple linear extrapolation is used. This yielded a predicted vitrinite reflectance of about .5 % $R_0$ at the surface in both wells. Data of Anders et al. (1992) suggests that surface rocks within the Uinta Basin typically exhibit reflectance values of approximately .5 % $R_0$ or less.

Model-predicted maturity is dominantly dictated by the heat flow and the amount of erosion or uplift specified by the user. Model calibration involves adjusting input parameters, such as heat flow and the amount of uplift or erosion, until model-predicted maturity indicators match the measured maturity indicators obtained from the various wells. As previously outlined, estimations of erosion in the Uinta Basin vary depending

on the researcher and the methods used to obtain the estimation. Conversely, there is more agreement among researchers regarding acceptable values for heat flow in the Uinta Basin. For this reason, multiple amounts of uplift and erosion are tested and heat flow is adjusted until model-predicted transformation ratios and vitrinite reflectance data are brought into agreement with measured transformation ratios and vitrinite reflectance data. Once an agreement between predicted and measured maturity is obtained, the erosion and heat flow required to achieve the match is evaluated. We found that the difference between model-predicted surface heat flow and the heat flow specified at the base of the lowest source interval was negligible due to the relatively shallow nature of the source intervals of this petroleum system. Furthermore, heat flow is assumed to be constant over time as evidenced by the lack of recent significant igneous activity within the Uinta Basin. As a result, heat flow values that approximate the values determined by Chapman et al. (1984) and Swanberg and Morgan (1985) are considered reasonable even though these studies investigated surface heat flow. Reasonable amounts of uplift or erosion are determined based on the corresponding thermal structure required to obtain the match between measured and predicted maturity data. For example, maturity can be held constant by increasing the amount of uplift and erosion while decreasing the heat flow. Alternatively, decreasing the erosion and increasing the heat flow can achieve the same effect. Both of these cases would result in the same predicted and measured maturity, however, the inputs required to obtain the match are different, usually with one set more geologically reasonable than the other. Once erosion and uplift are established, it is assumed that these values represent reasonable estimations that can be extrapolated to areas where no geochemical data is available for calibration. In these areas, particularly

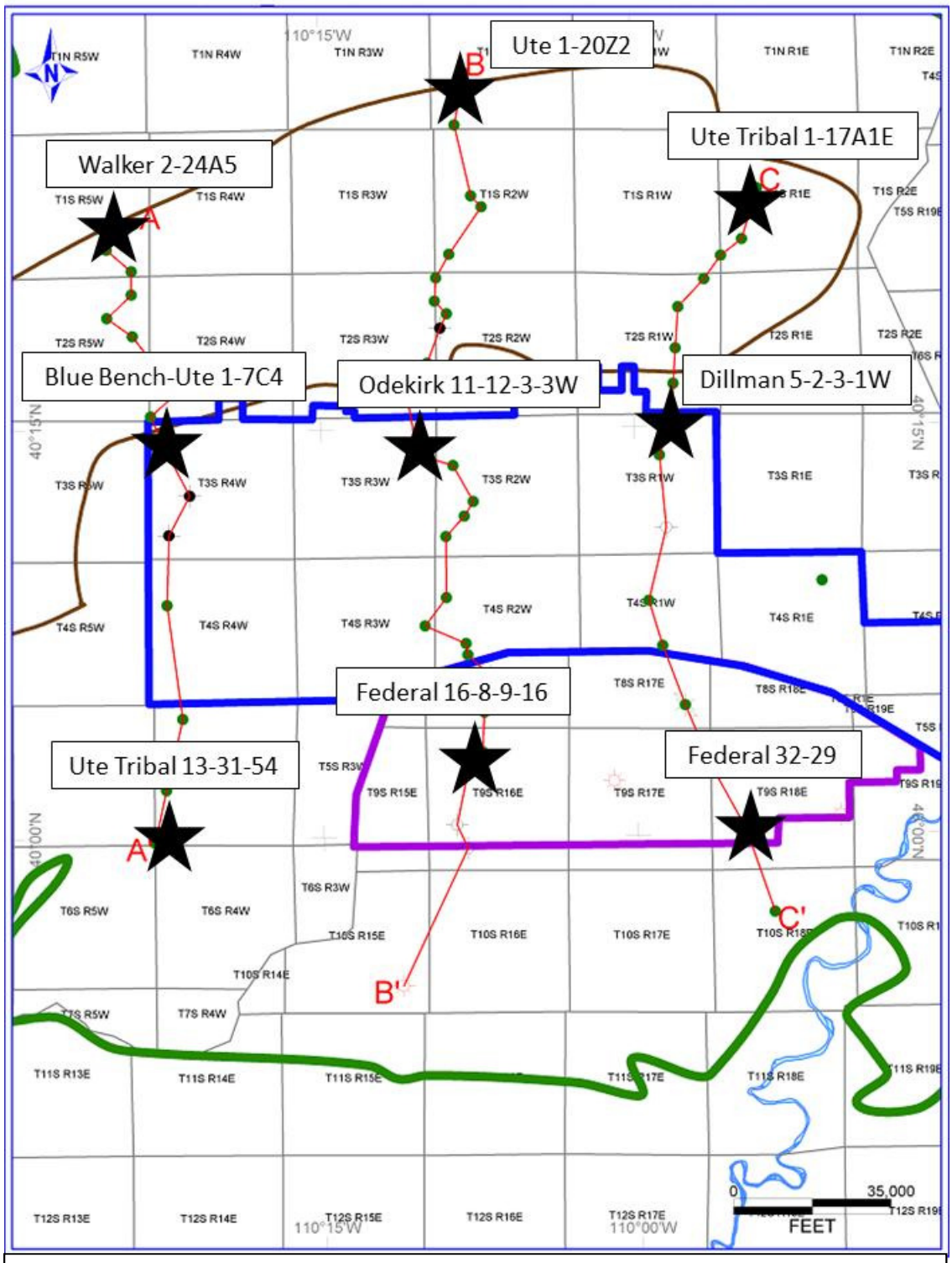


***Figure 11***: Locations of wells used to build the select 1-D models shown in this study. Three wells were selected from the northern, central, and southern portions of each line of section.

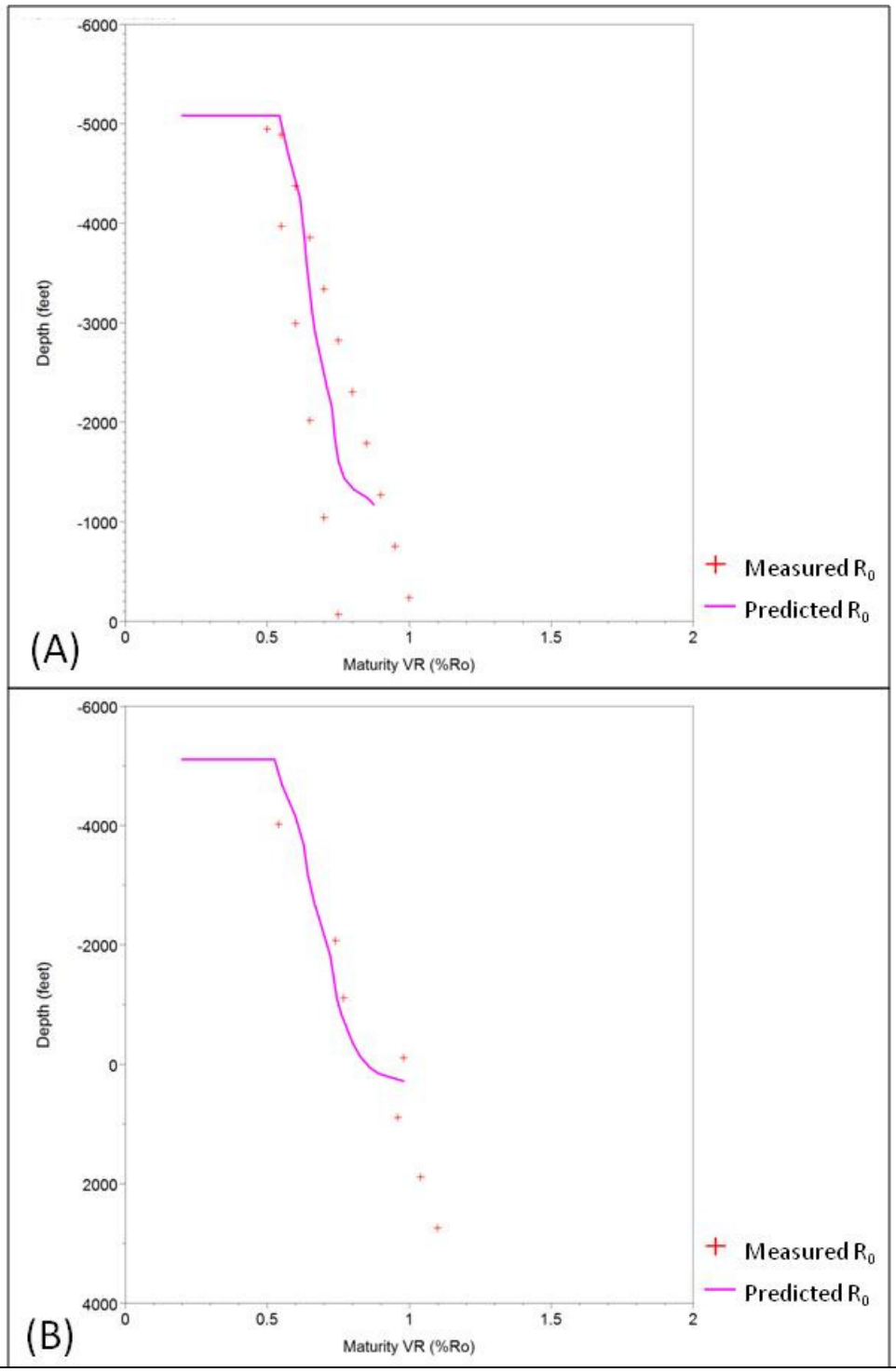


***Figure 12***: Model-predicted vitrinite reflectance with respect to depth compared with the measured vitrinite reflectance data from the southern and central areas of C-C'. (A) Measured $Vr_0$ from Beluga 5-16T-9-17 and Federal 15-24-9-18 compared with model-predicted $Vr_0$ at adjacent well Federal 12-7-9-18. (B) Measured $Vr_0$ from Ute Tribal 3-11-4-1E compared with model-predicted $Vr_0$ at adjacent well Lamb 13-10-4-1W.

the northern and western portions of the study area, the thermal structure is modeled after the heat flow trends determined by Chapman et al. (1984) and the thermal gradients determined by Anders et al. (1992).

## CHAPTER 4: Results

After the models are calibrated to the measured data, details involving the basin's thermal history and uplift can be inferred. Multiple iterations were attempted with eroded thicknesses ranging from approximately 5000 to 8000 ft (1524 to 2438 m) and corresponding heat flow values that range from 54 to 75 $mW/m^2$. In the following section, the results of the 1-D and 2-D models are discussed from east to west. The well locations from which 1-D models are captured are shown in Figure 11.

### 4.1 Line C-C'

A comparison of the model-predicted vitrinite reflectance with respect to depth with the measured vitrinite reflectance data from the southern and central areas of C-C' is shown in Figure 12. Vitrinite reflectance measurements are not available from wells directly on C-C', so calibration is done at the well nearest the data points. As a result, the southern portion of C-C' is calibrated to measured vitrinite reflectance data from wells Beluga 5-16R-9-17 and Federal 15-24-9-18 and the south-central segment of C-C' is calibrated to measured vitrinite reflectance from Ute Tribal 3-11-4-1E. Table 4 compares model-predicted transformation ratios with measured transformation ratios from Rock-Eval pyrolysis on samples from Dillman 5-2-3-1W.

**Table 4**: Transformation ratios determined from Rock-Eval pyrolysis compared with model-predicted transformation ratios at Dillman 5-2-3-1W.

| Dillman 5-2-3-1W | Rock Eval (TR) | Model (TR) |
|---|---|---|
| R8 | N/A | 0.055 |
| R7 | 0.01 | 0.059 |
| R6 | 0.07 | 0.08 |
| GG0 | 0.06 | 0.107 |
| GG | 0.27 | 0.121 |
| GG1 | 0.26 | 0.168 |
| GG2 | 0.33 | 0.314 |

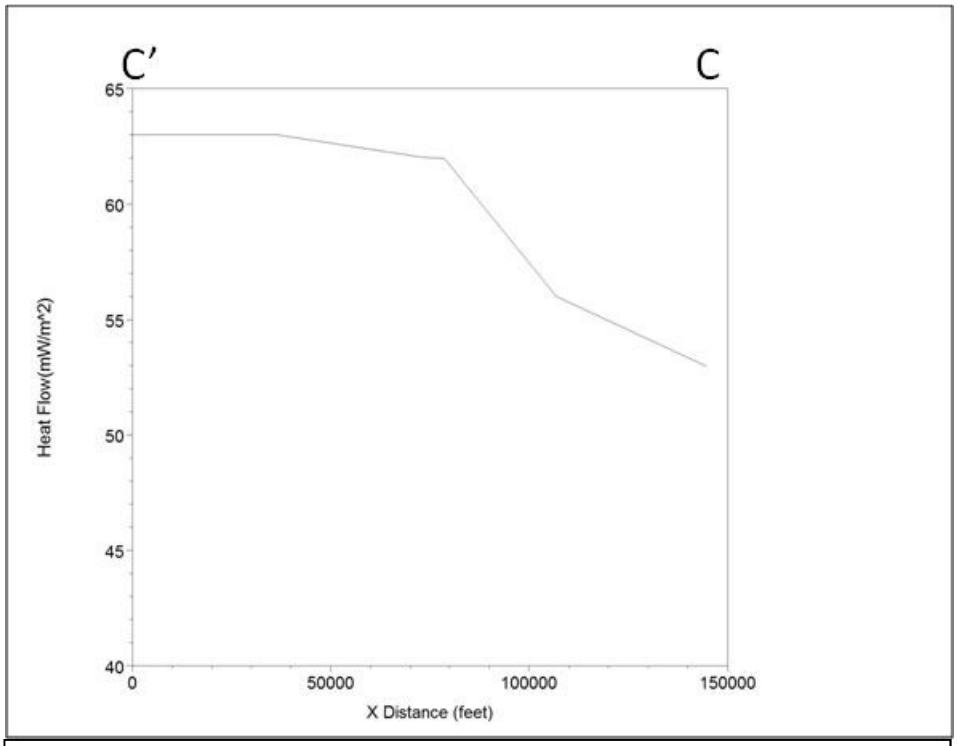


***Figure 13***: Variation in modeled heat flow along line C-C'.

Along cross section C-C', matching of model-predicted vitrinite reflectance and transformation ratios with measured data near the section is best achieved with an estimated eroded thickness of 7200 ft (2195 m) and heat flow values ranging from 53 $mW/m^2$ at the northern end of the cross section and 63 $mW/m^2$ at the southern end of the cross section. The systematic variation in heat flow from south to north along cross section C-C' is shown in Figure 13. The 1-D burial history for Federal 32 29, which is located on the southern end of C-C', is shown in Figure 14. A maximum burial depth of approximately 10,800 ft (3292 m) is achieved by 20 Ma prior to the onset of major uplift and erosion at this well location. Model predictions suggest that by 12.5 Ma, only the basal source interval (GG2) reaches maturity while the other source beds remain immature. Figure 15 compares the burial history with tectonic subsidence at this location. Tectonic subsidence accounts for 5440 ft (1658 m) of burial prior to the onset of major uplift at this location. The 1-D burial history for Dillman 5-2-3-1W, located toward the middle of line C-C', is shown in Figure 16. At this location, a maximum burial depth of approximately 14600 ft (4450 m) is achieved by 20 Ma prior to major uplift and erosion. Model predictions suggest that maturity is attained around 20 Ma for interval GG2, 12.5 Ma for intervals GG1 and GG, and 7.5 Ma for interval GG0, which reaches maturity during the early stages of uplift. The overlying rich zones R6-R8 remain immature at this location. Figure 17 compares the burial history with tectonic subsidence predicted at this well. Here, tectonic subsidence accounts for 6890 ft (2100 m) of burial before major uplift. The 1-D burial history for Ute Tribal 1-17A1E, located at the northern most point of section C-C', is shown in Figure 18. At this location, a maximum burial depth of approximately 16,400 ft (5000 m) is achieved at 20 Ma prior to major uplift and erosion.

Model predictions suggest that maturity is achieved around 22.5 Ma for intervals GG2 and GG1, 17.5 Ma for interval GG, 12.5 Ma for interval GG0, and 10 Ma for the R6 zone. The Mahogany R7 and R8 intervals are predicted to be immature at this location. Figure 19 compares the burial history with tectonic subsidence at this location. Here, tectonic subsidence accounts for 7580 ft (2310 m) of burial prior to the onset of uplift and erosion. For all three of these wells, uplift due to tectonic processes accounts for roughly 3800 ft (1158 m) of uplift from 10 Ma to the present. In addition, both the predicted total subsidence and tectonic subsidence increase northward toward the Uinta Uplift.

Figure 20 is a calculated 2-D cross section of line C-C' illustrating the lateral changes in model-predicted transformation ratios. Transformation ratios systematically increase from south to north along line C-C'. This trend is observed until the two northern most wells are encountered where predicted transformation ratios decrease. This can be attributed to the effects of decreasing heat flow outpacing the effects of greater burial depths toward the north. In this study, a transformation ratio of 0.1 or greater signifies the entry of a source rock into the maturity window. Maturity is greatest in between x distances 113000 and 133000 ft (34442 and 40538 m), which corresponds to the area in between wells Cook 1-26B1 and Ute Tribal 1-29A1E. Maturity of the GG2 and GG1 intervals is the most widespread, with zones of predicted immaturity existing only in the southern most portion of section C-C'. The predicted maturity for the GG and GG0 intervals spans roughly half of line C-C' from the midpoint to the northern most portion. Maturity predicted for the R6 and Mahogany R7 intervals is largely restricted to the northern most portions of line C-C'. Finally, widespread immaturity is predicted for the upper R8 interval. The positions along C-C' and the depths in which each of the

intervals of interest achieve a transformation ratio of 0.1 or greater are summarized in Table 5. Figure 21 is another calculated cross section illustrating the model-predicted migration vectors and the oil accumulated volume ratio (bbls/ acre*ft rock). In the northern and deepest portion of the section, model predictions suggest that hydrocarbons migrate to overlying stratigraphic intervals. From north to south, migration vectors indicate a progressive change from vertical migration to migration in an updip direction. However, migration to overlying stratigraphic intervals occurs from the basal source interval (GG2) throughout most of the section. As a result, the model predicts that accumulations may occur in areas where source beds are immature. The largest accumulations occur in the northern and deepest sections, in addition to the central portion of line C-C'. Accumulations in the central region are likely due to updip migration.

**Table 5**: Positions and depths along C-C' in which source rocks achieve a transformation ratio of 0.1 or greater.

| Source Interval | Distance x (ft) | Depth Subsurface (ft) | Depth Subsea (ft) |
|---|---|---|---|
| R8 | Immature | Immature | Immature |
| R7 | 128400 | 7394 | 2268 |
| R6 | 112700 | 6702 | 1681 |
| GG0 | 76800 | 4846 | -230 |
| GG | 59750 | 4305 | -795 |
| GG1 | 35100 | 3747 | -1330 |
| GG2 | 25600 | 3637 | -1480 |

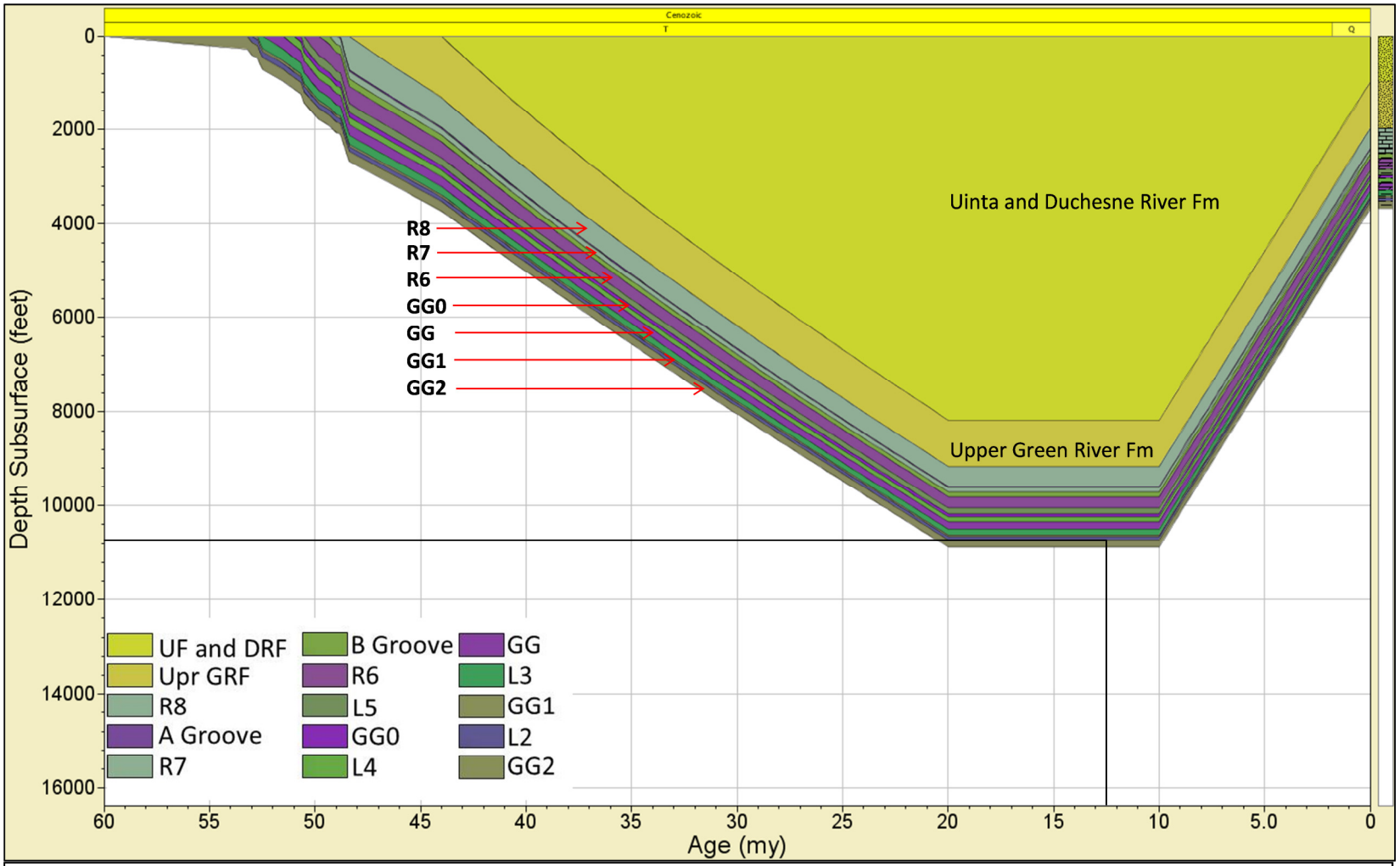


***Figure 14***: Burial history for Federal 32-29. The basal source interval (GG2) first enters the oil window around 12.5 Ma at a depth of approximately 10800 ft (3292 m).

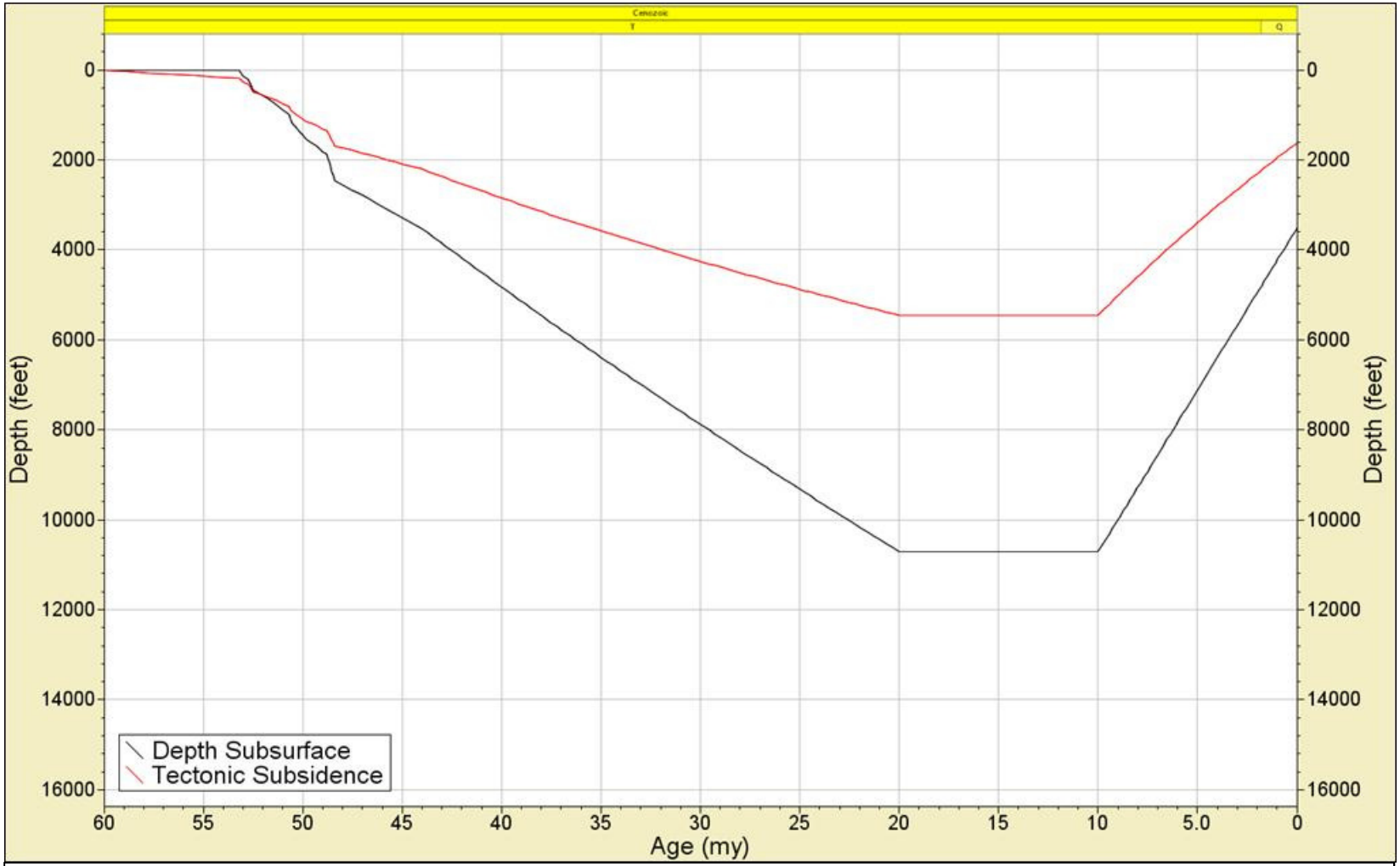


***Figure 15***: Burial history compared with tectonic subsidence at Federal 32-29. Tectonic subsidence accounts for 5440 ft (1658 m) of burial prior to the onset of major uplift at this location.

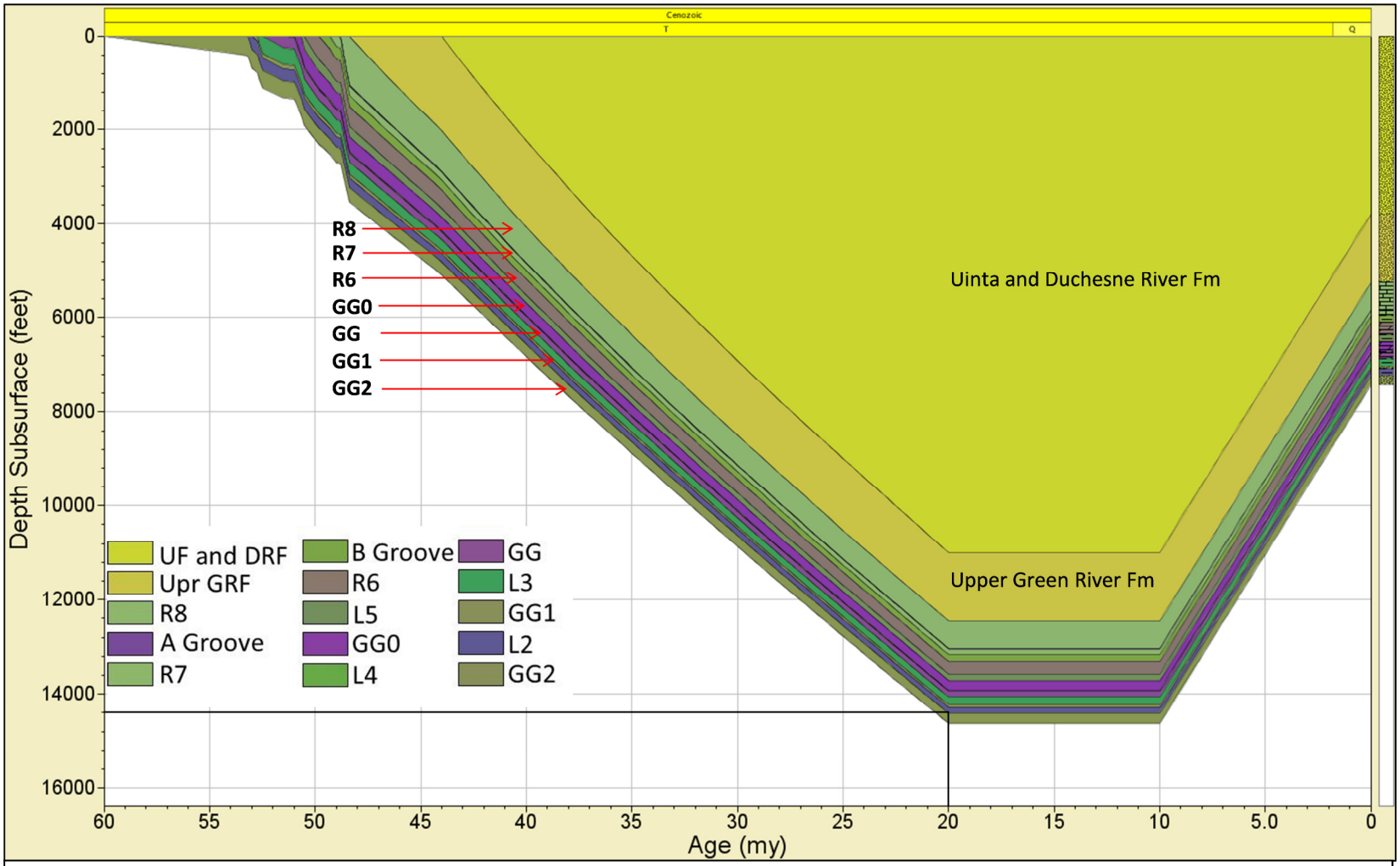


***Figure 16***: Burial history for Dillman 5-2-3-1W. The basal source interval (GG2) first enters the oil window around 20 Ma at a depth of approximately 14400 ft (4389 m).


***Figure 17***: Burial history compared with tectonic subsidence at Dillman 5-2-3-1W. Tectonic subsidence accounts for 6890 ft (2100 m) of burial prior to the onset of major uplift at this location.

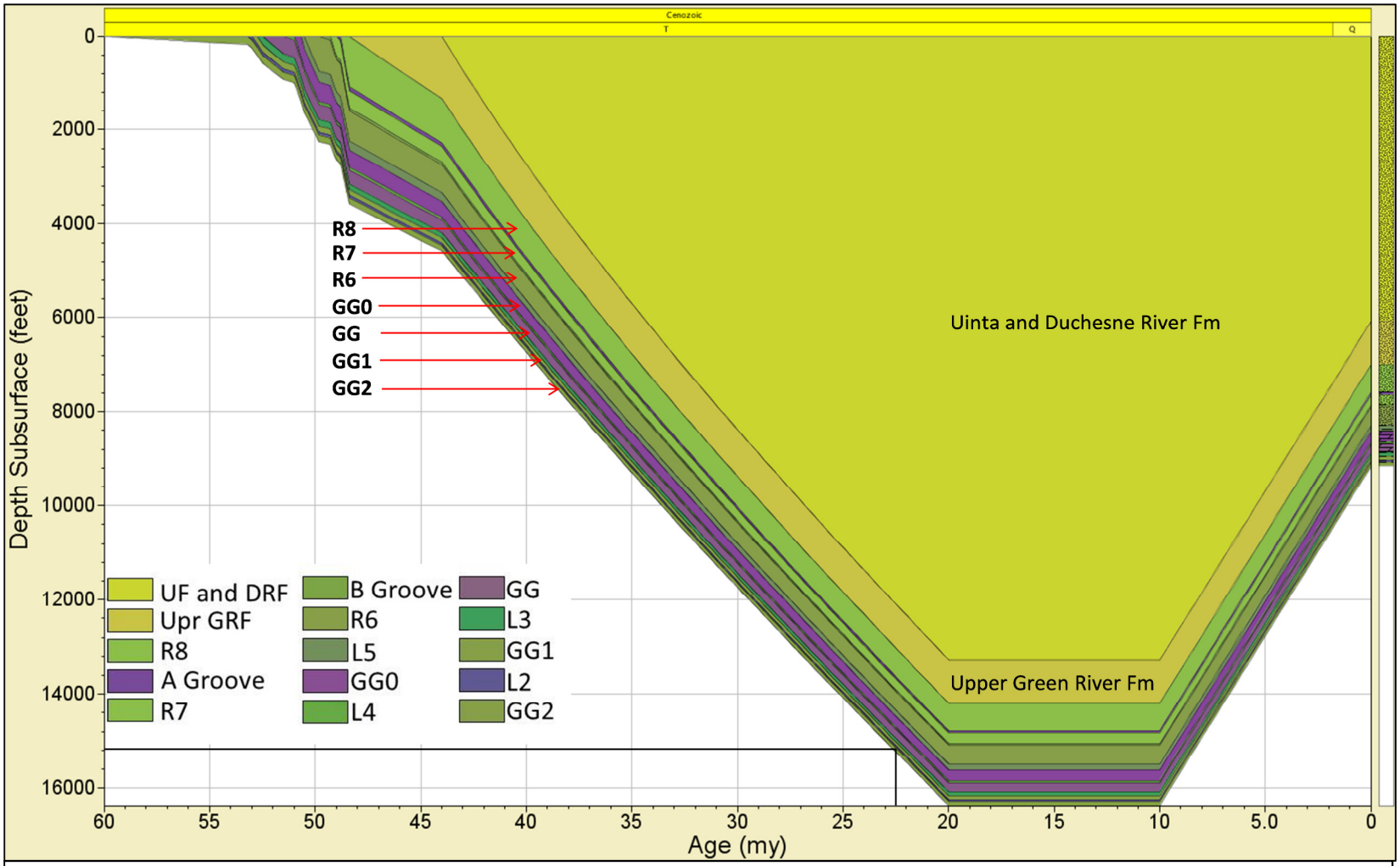


***Figure 18***: Burial history for Ute Tribal 1-17A1E. The basal source interval (GG2) first enters the oil window around 22.5 Ma at a depth of approximately 15200 ft (4633 m).

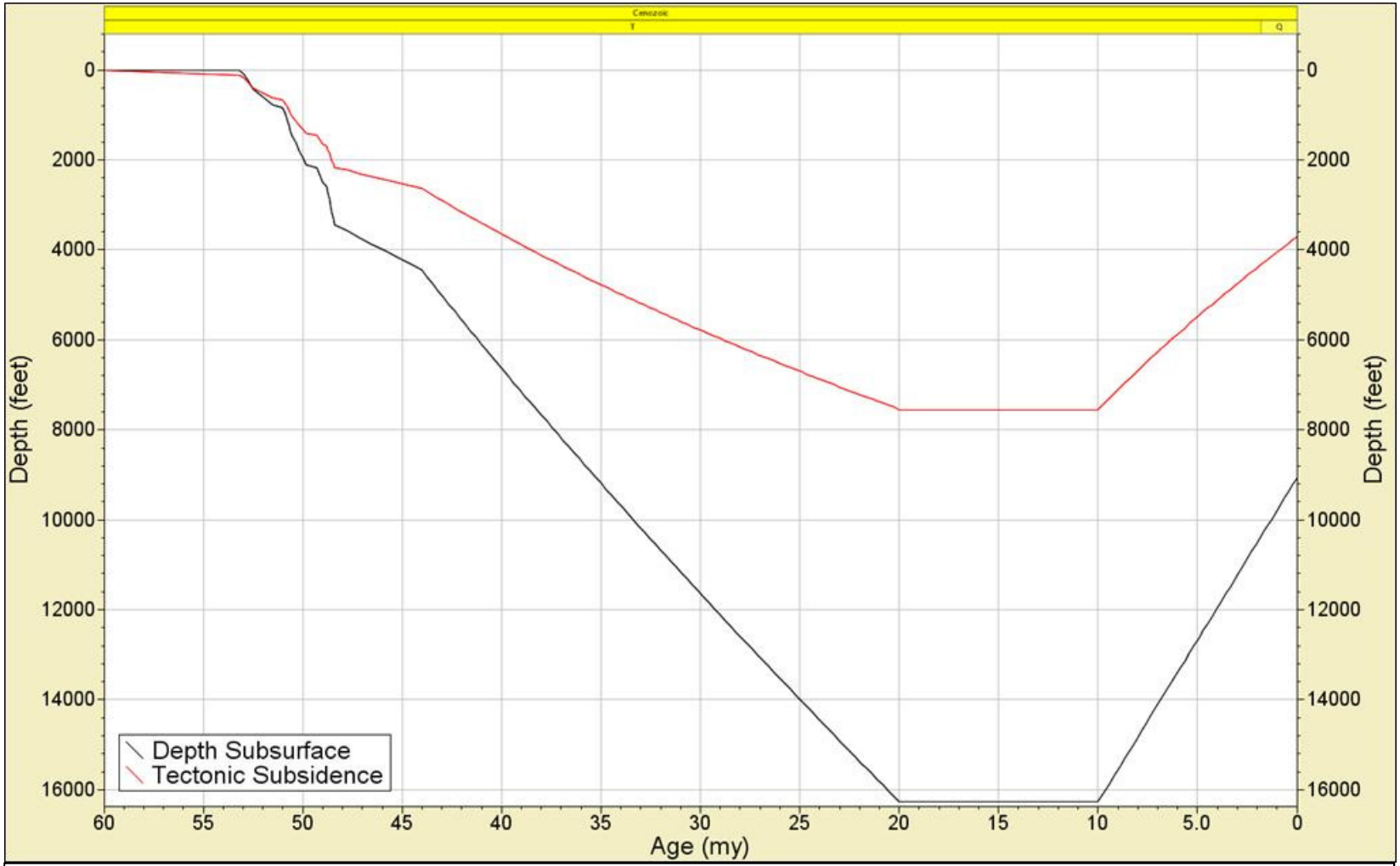


***Figure 19:*** Burial history compared with tectonic subsidence at Ute Tribal 1-17A1E. Tectonic subsidence accounts for 7580 ft (2310 m) of burial prior to the onset of major uplift at this location.

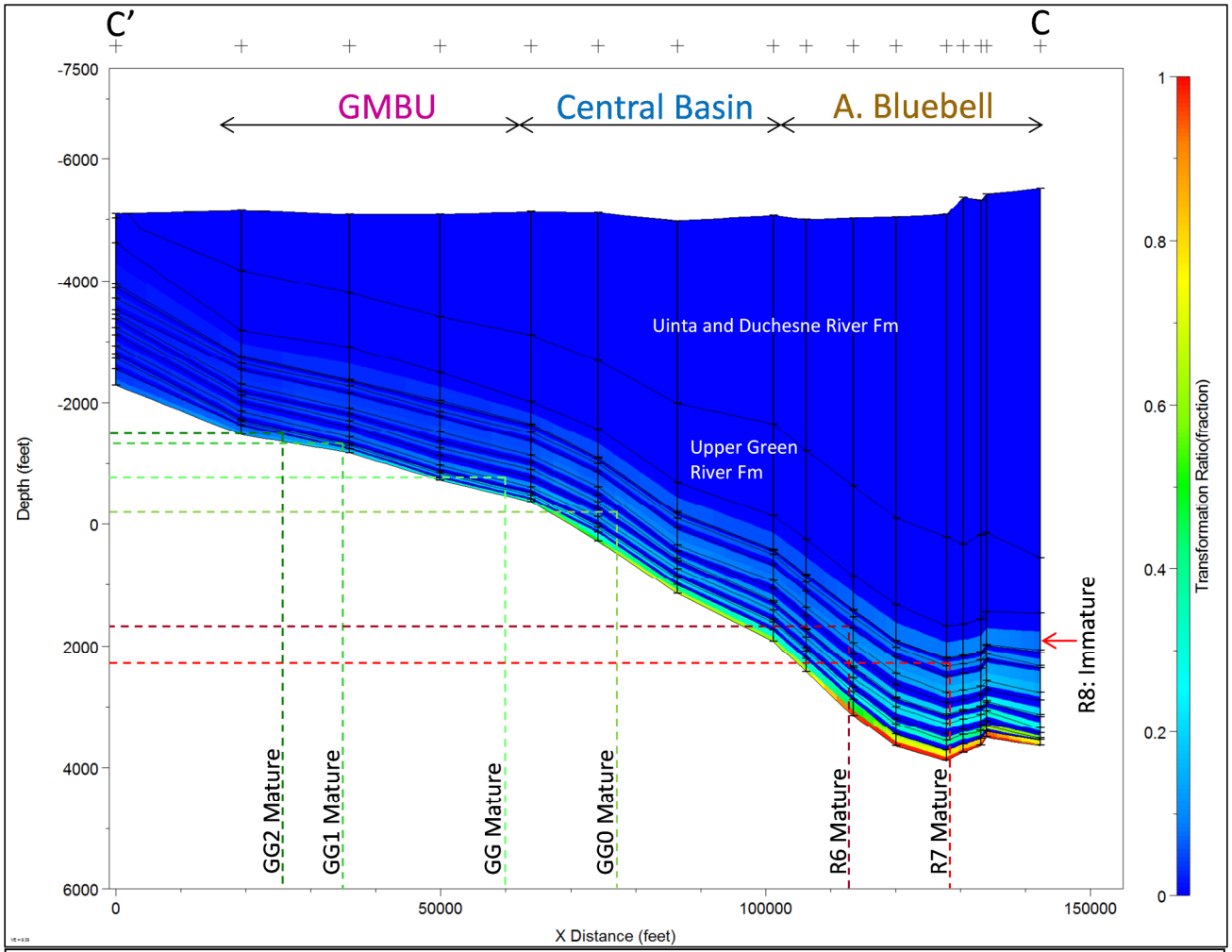


***Figure 20***: Calculated 2-D cross section of C-C' showing lateral changes in model-predicted transformation ratios. The position and depth in which each interval achieves a transformation ratio of 0.1 of greater is marked. Note depth scale is subsea.

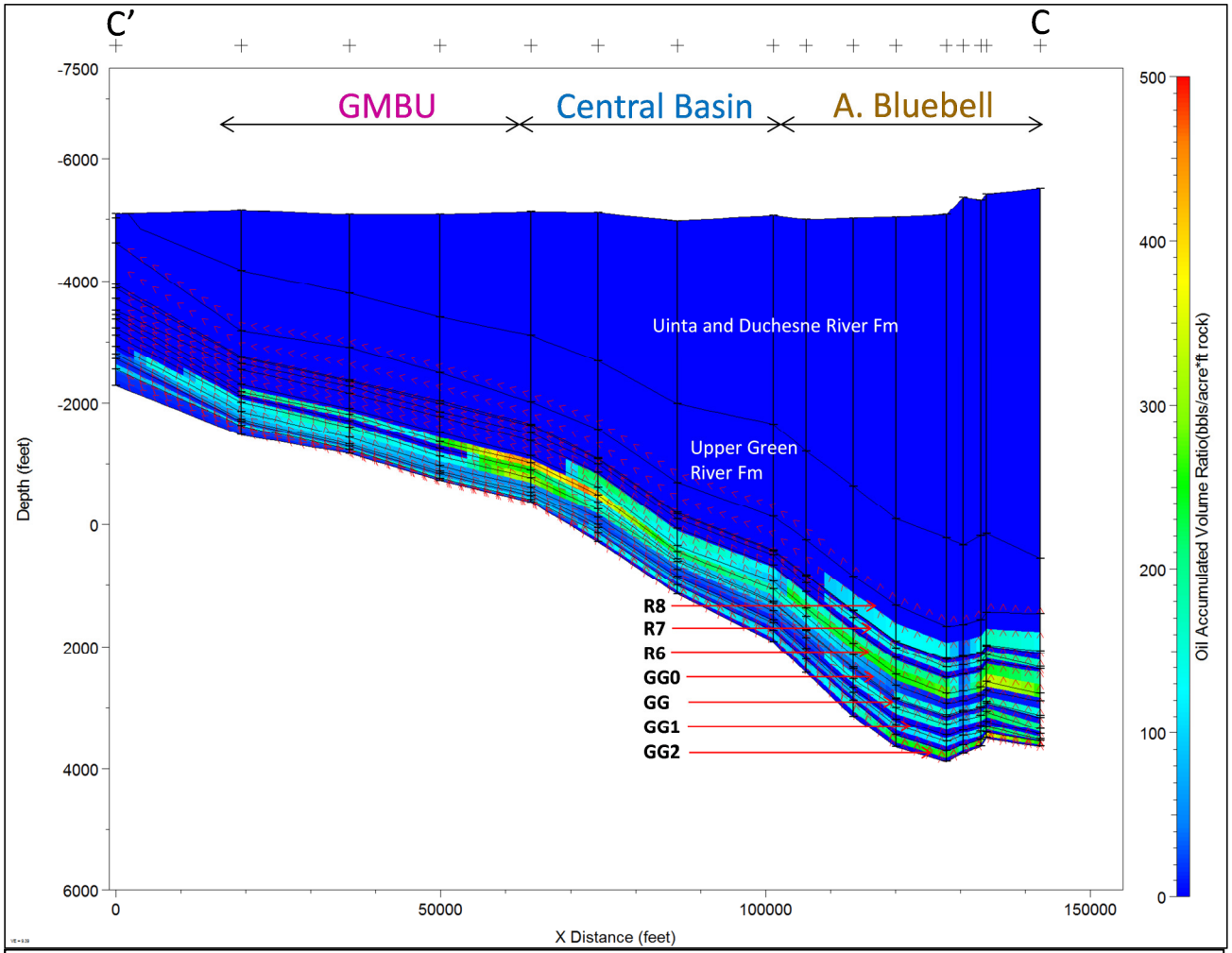


***Figure 21***: Calculated 2-D cross section of C-C' showing model-predicted migration vectors (red arrows) and oil accumulated volume ratio (bbls/ acre*ft rock).

### 4.2 Line B-B'

A comparison of model-predicted vitrinite reflectance with respect to depth with measured vitrinite reflectance data from line B-B' is shown in Figure 22. Vitrinite reflectance data used to calibrate the southern and central portions of line B-B' is taken from wells Beluga 5-16R-9-17 and Ute Tribal 15-13-4-3W, respectively. In the central area of B-B', calibration to the measured vitrinite reflectance data from well Ute Tribal 15-13-4-3W is difficult due to the scattered nature of the data, so measured transformation ratios are used as the primary calibration tool at this well. As a result, only a moderate match exists between the model-predicted and measured vitrinite reflectance. It is feasible that samples from this well experienced abnormal thermal conditions, possibly related to hydrothermal fluids sourced from greater depths along the Duchesne Fault System. Table 6 compares model-predicted transformation ratios with transformation ratios obtained from Rock-Eval conducted on samples from Murphy 2-31-3-2W and Ute Tribal 15-13-4-3W.

Along cross section B-B', calibration of the models with measured data is best achieved with an eroded thickness of 6700 ft (2042 m) and heat flow values ranging from 45 $mW/m^2$ at the sections northern end to 65 $mW/m^2$ at the sections southern end. The systematic variation in modeled heat flow from south to north along section B-B' is shown in Figure 23. The 1-D burial history for Federal 16-8-9-16, located toward the southern end of B-B', is shown in Figure 24. Here, a maximum burial depth of approximately 10800 ft (3292 m) is achieved by 20 Ma prior to major uplift and erosion. Model predictions at this well indicate that every source rock remains immature throughout the burial history. Figure 25 compares the burial history with tectonic

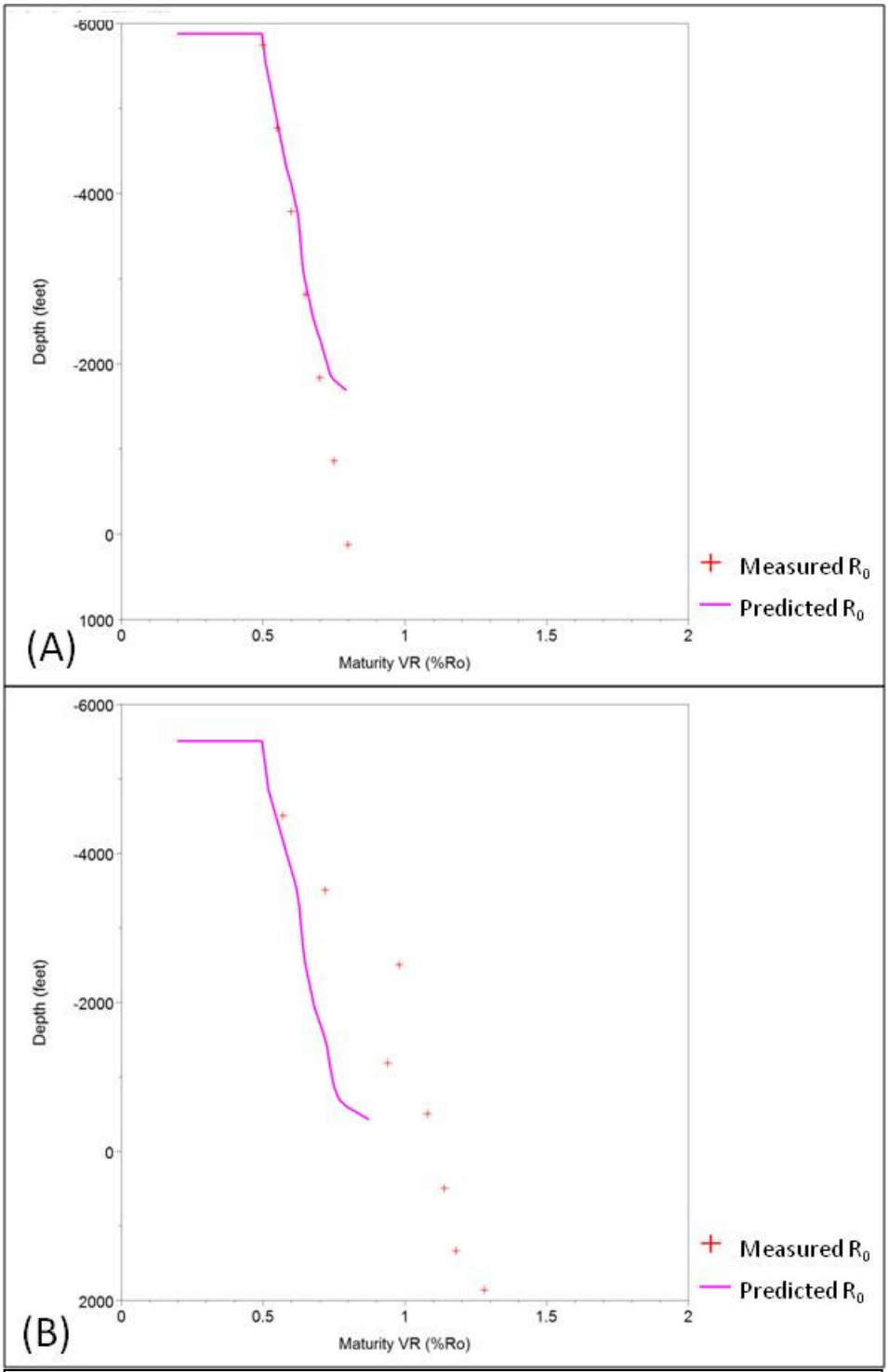


***Figure 22***: Model-predicted vitrinite reflectance with respect to depth compared with the measured vitrinite reflectance data from the southern and central areas of B-B'. (A) Measured Vr0 from Beluga 5-16T-9-compared with model-predicted Vr0 at adjacent well Federal 16-8-9-16. (B) Measured Vr0 compared with model-predicted $Vr_0$ at Ute Tribal 15-13-4-3W.

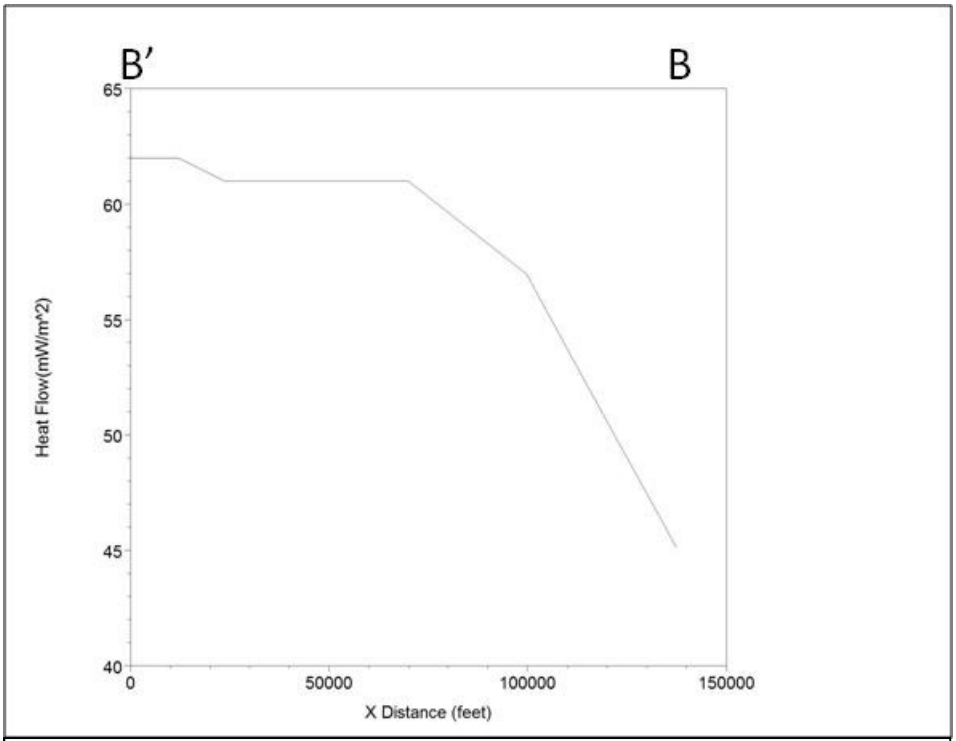


***Figure 23***: Variation in modeled heat flow along line B-B'.

**Table 6**: Transformation ratios determined from Rock-Eval pyrolysis compared with model-predicted transformation ratios at Ute Tribal 15-13-4-3W and Murphy 2-31-3-2W.

| Ute Tribal 15-13-4-3W | Rock Eval (TR) | Model (TR) | Murphy 2-31-3-2W | Rock Eval (TR) | Model (TR) |
|---|---|---|---|---|---|
| R8 | 0.06 | 0.024 | R8 | N/A | 0.061 |
| R7 | 0.04 | 0.027 | R7 | 0.03 | 0.065 |
| R6 | 0.05 | 0.035 | R6 | 0.09 | 0.081 |
| GG0 | 0.12 | 0.043 | GG0 | 0.16 | 0.105 |
| GG | 0.07 | 0.052 | GG | 0.18 | 0.123 |
| GG1 | 0.12 | 0.1 | GG1 | Lean Samples | 0.171 |
| GG2 | 0.13 | 0.14 | GG2 | 0.4 | 0.351 |

subsidence at this well. Subsidence due to tectonic processes accounts for about 5400 ft (1646 m) of burial before major uplift. The 1-D burial history for Odekirk 11-12-3-3W, located in the central portion of line B-B', is shown in Figure 26. At this location, a maximum burial depth of about 13800 ft (4206 m) is achieved prior to major uplift and erosion. Model predictions suggest that maturity is achieved by 20 Ma for interval GG2, 12.5 Ma for intervals GG1 and GG, and 7.5 Ma for interval GG0. The remaining intervals spanning from the R6 through the R8 are predicted to remain immature throughout the burial history. Figure 27 compares the burial history with model-predicted tectonic subsidence at this well. Here, tectonic subsidence accounts for 6630 ft (2021 m) of burial before major uplift. The 1-D burial history for well Ute 1-20Z2, located at the northern end of B-B', is shown in Figure 28. At this location, a maximum burial depth of just over 18400 ft (5608 m) is achieved prior to the onset of major uplift and erosion. Model predictions suggest that maturity is achieved by 22.5 Ma for intervals GG2 and GG1, 17.5 Ma for interval GG, 12.5 Ma for interval GG0, and 10 Ma for interval R6. The Mahogany R7 and R8 intervals are predicted to remain immature throughout the burial history. Figure 29 compares the burial history with tectonic subsidence predicted at this location. Here, tectonic subsidence accounts for 8260 ft (2518 m) of burial before major uplift. For all three wells, the models predict that approximately 3600 ft (1097 m) of uplift from 10 Ma to present is due to tectonic processes. Similar to line C-C', predicted maximum burial depths and subsidence due to tectonic processes systematically increase from south to north.

Figure 30 is a calculated 2-D cross section of line B-B' illustrating the lateral changes in model-predicted transformation ratios. Transformation ratios systematically

increase from south to north along B-B' and are greatest in between x distances of 85000 and 115000 ft (25908 and 35052 m), which corresponds to the positions of wells Odekirk 11-12-3-3W and Swykes 2-21A2, respectively. Farther to the north, past an x distance of 115000 ft (35052 m), transformation ratios begin to progressively decrease until the southern end of B-B' is encountered. Here, the effects of decreasing heat flow are outweighing the effects of greater burial depth and this is much more pronounced with respect to line C-C'. Intervals GG2 and GG1 exhibit the most widespread maturity, but are predicted to be immature within the southern third of line B-B'. Similar to line C-C', predicted maturity for intervals GG and GG0 spans roughly half of line B-B', from the midpoint to the northern portion. Maturity of intervals R6 and Mahogany R7 is largely restricted to zones in between x distances of 85000 and 115000 ft (25908 and 35052 m). The R8 interval remains largely immature, with a narrow zone of predicted maturity occurring between x distances of 110600 and 115000 ft (33711 and 35052 m). The positions along B-B' and the depths where each of the intervals of interest achieve a transformation ratio of 0.1 or greater are summarized in Table 7. Figure 31 is another calculated cross section illustrating the model-predicted migration vectors and the oil accumulated volume ratio (bbls/ acre*ft rock). In general, the trends mimic those of line C-C' with migration occurring dominantly to overlying stratigraphic intervals within the northern portions of the section and then transitioning to primarily updip migration toward the south. The largest accumulations are predicted to occur in the northern section of line B-B' where transformation ratios are greatest and in the southern section of the line. The presence of large accumulations in the southern most portions of line B-B'

indicates that large amounts of updip migration are predicted. In general, the intervals shown in the 2-D model of B-B' are more steeply dipping with respect to those of C-C'.

**Table 7**: Positions and depths along B-B' in which source rocks achieve a transformation ratio of 0.1 or greater.

| Source Interval | Distance x (ft) | Depth Subsurface (ft) | Depth Subsea (ft) |
|---|---|---|---|
| R8 | 110600 | 7872 | 1828 |
| R7 | 97500 | 7084 | 1252 |
| R6 | 88558 | 6302 | 890 |
| GG0 | 66880 | 5485 | 289 |
| GG | 65960 | 5640 | 423 |
| GG1 | 55411 | 4770 | -720 |
| GG2 | 51020 | 4750 | -689 |

### 4.3 Line A-A'

For line A-A', no measured data is available for model calibration. Estimated amounts of erosion for lines C-C' and B-B' easily fall within the range of values suggested by previous researchers (Narr and Currie, 1982; Sweeney et al., 1987; Anders et al., 1992; and Johnson and Nuccio, 1993). Heat flow values determined from the calibration process agree with values determined by Chapman et al. (1984) and Swanberg and Morgan (1985). As a result, the estimated erosion and heat flow for A-A' will be based on the work of previous researchers. Amounts of uplift and erosion determined by Sweeney et al. (1987) range from 5000 – 10000 ft (1524 – 3048 m) in townships that surround the area of line A-A'. It is probable that erosion did not vary considerably over the distance between the three cross sections, so the value of 7000 ft (2134 m) is used because it is close to values estimated for lines C-C' and B-B' and falls in the middle of

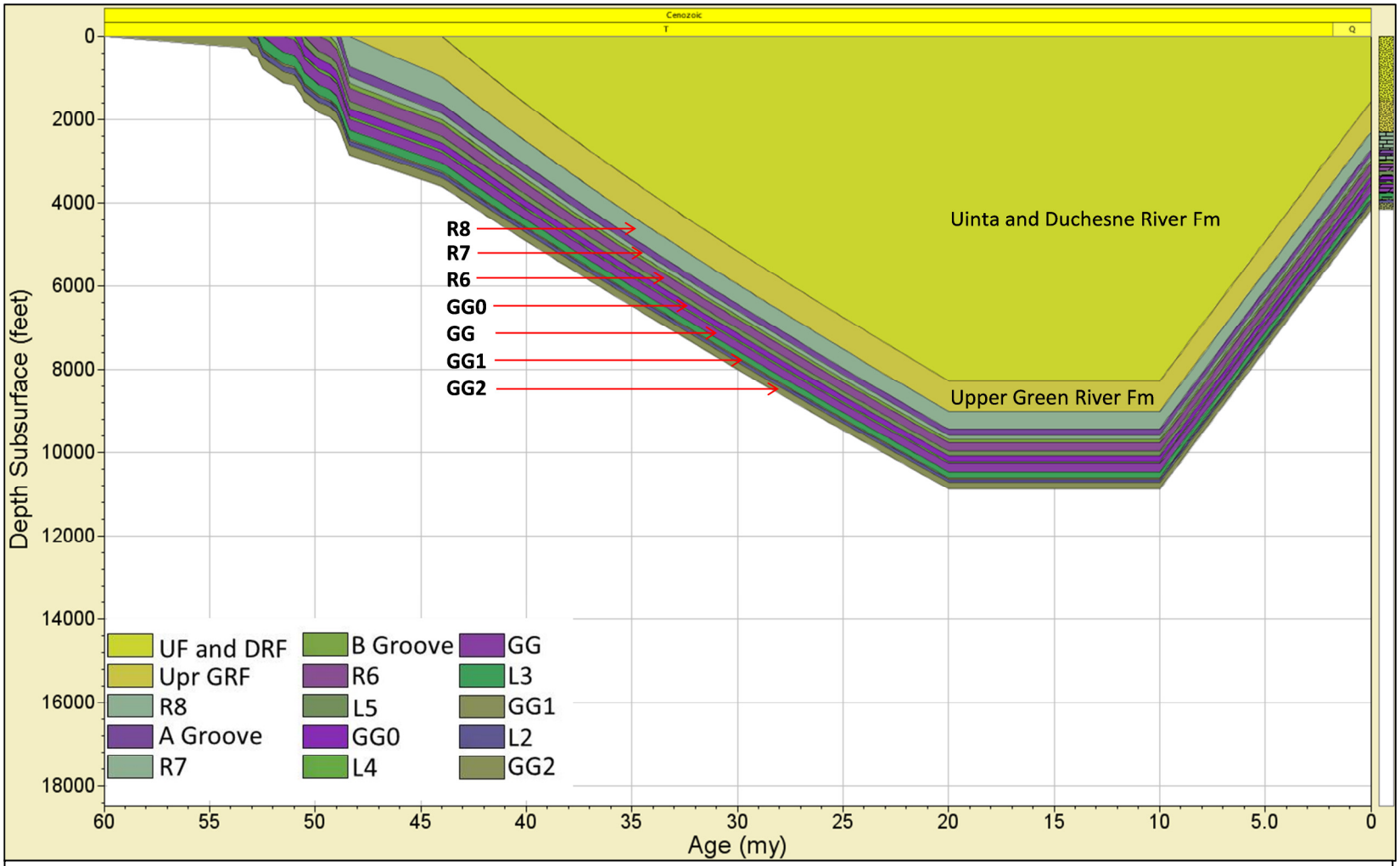


***Figure 24***: Burial history for Federal 16-8-6-16. All source rocks are predicted to remain immature during burial at this location.

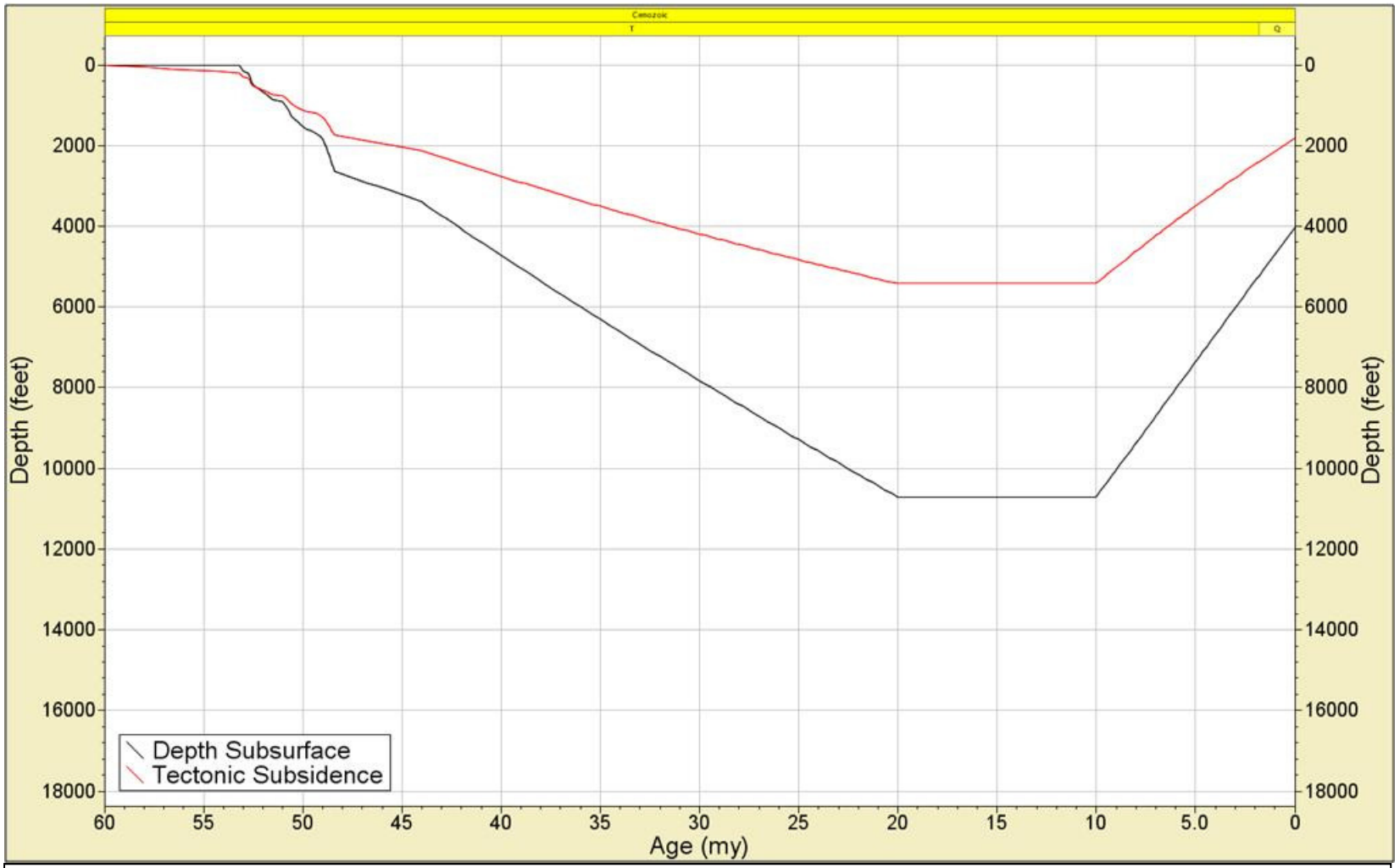


***Figure 25***: Burial history compared with tectonic subsidence at Federal 16-8-6-16. Tectonic subsidence accounts for 5400 ft (1646 m) of burial prior to the onset of major uplift at this location.

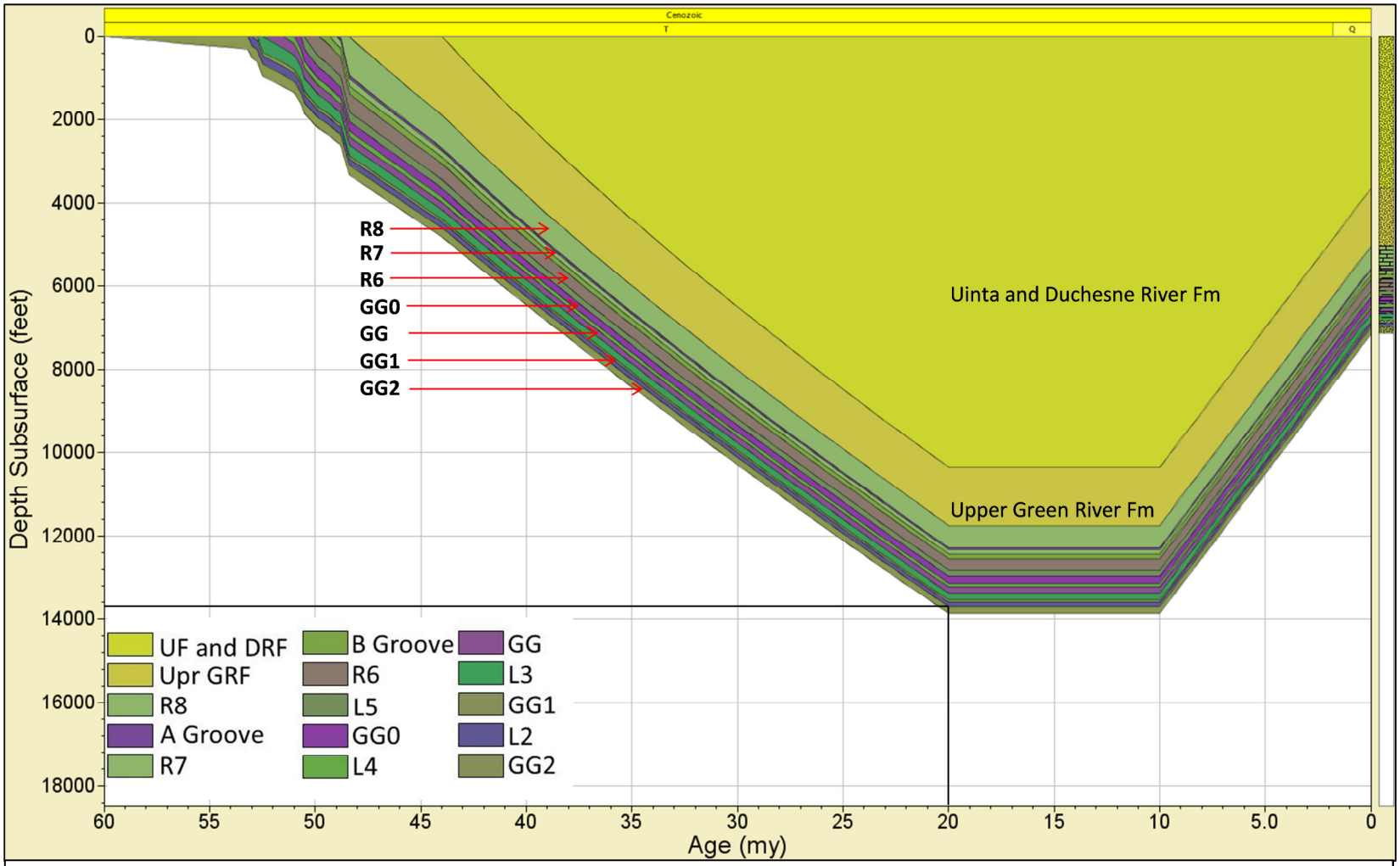


**Figure 26**: Burial history for Odekirk 11-12-3-3W. The basal source interval (GG2) first enters the oil window around 20 Ma at a depth of approximately 13600 ft (4145 m).

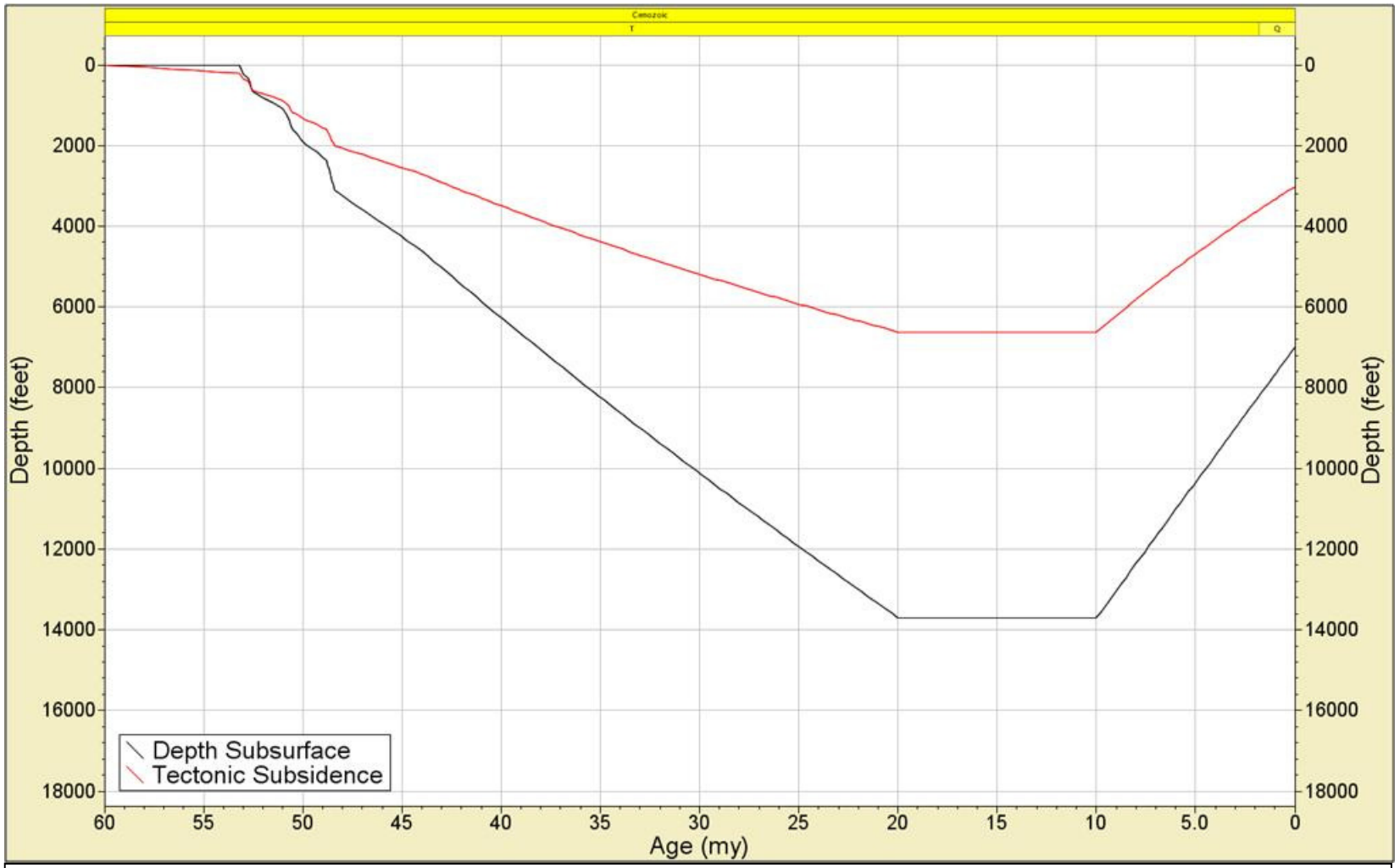


***Figure 27***: Burial history compared with tectonic subsidence at Odekirk 11-12-3-3W. Tectonic subsidence accounts for 6630 ft (2021 m) of burial prior to the onset of major uplift at this location.

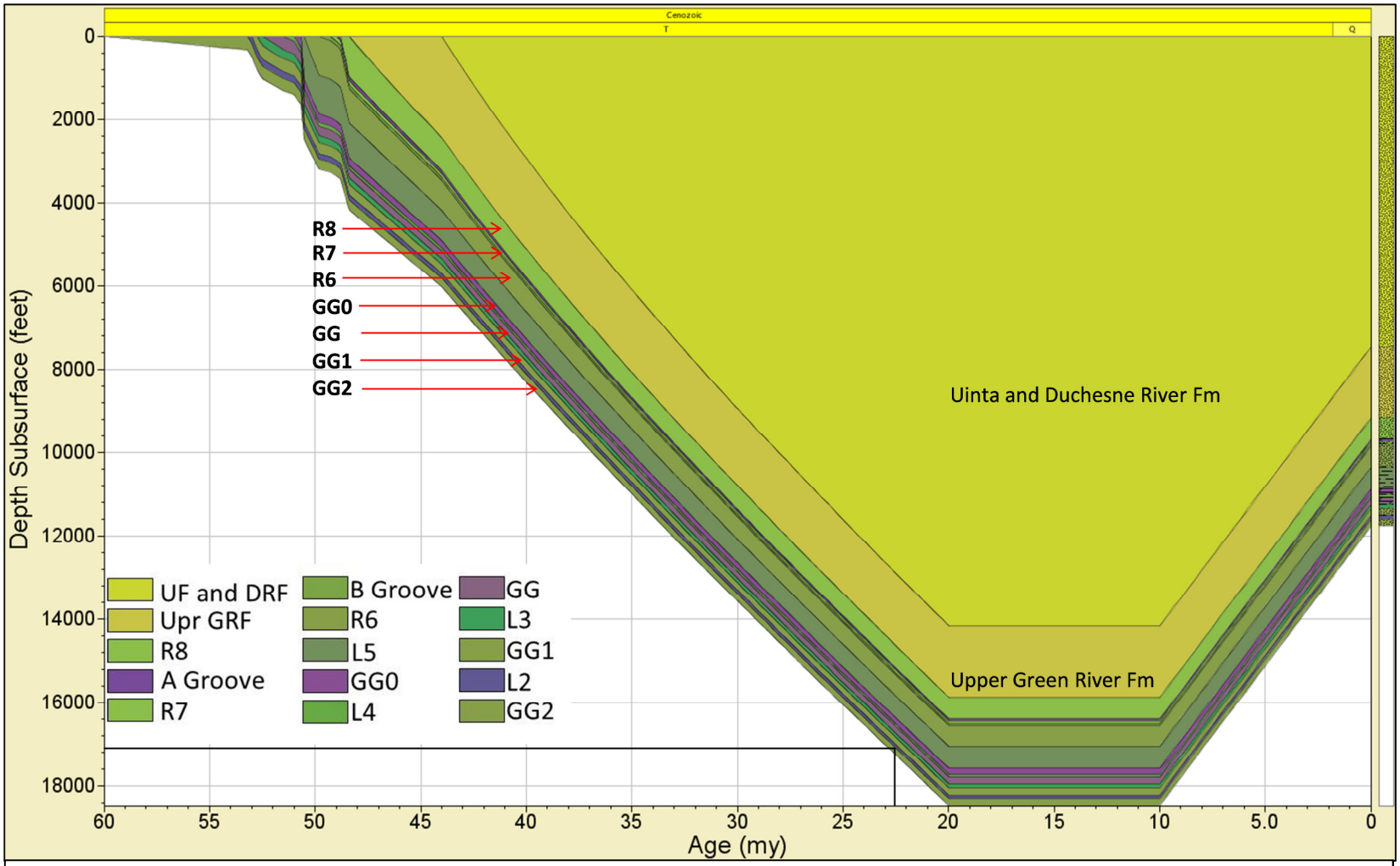


***Figure 28***: Burial history for Ute 1-20Z2. The basal source interval (GG2) first enters the oil window around 22.5 Ma at a depth of just under 17200ft (5243 m).

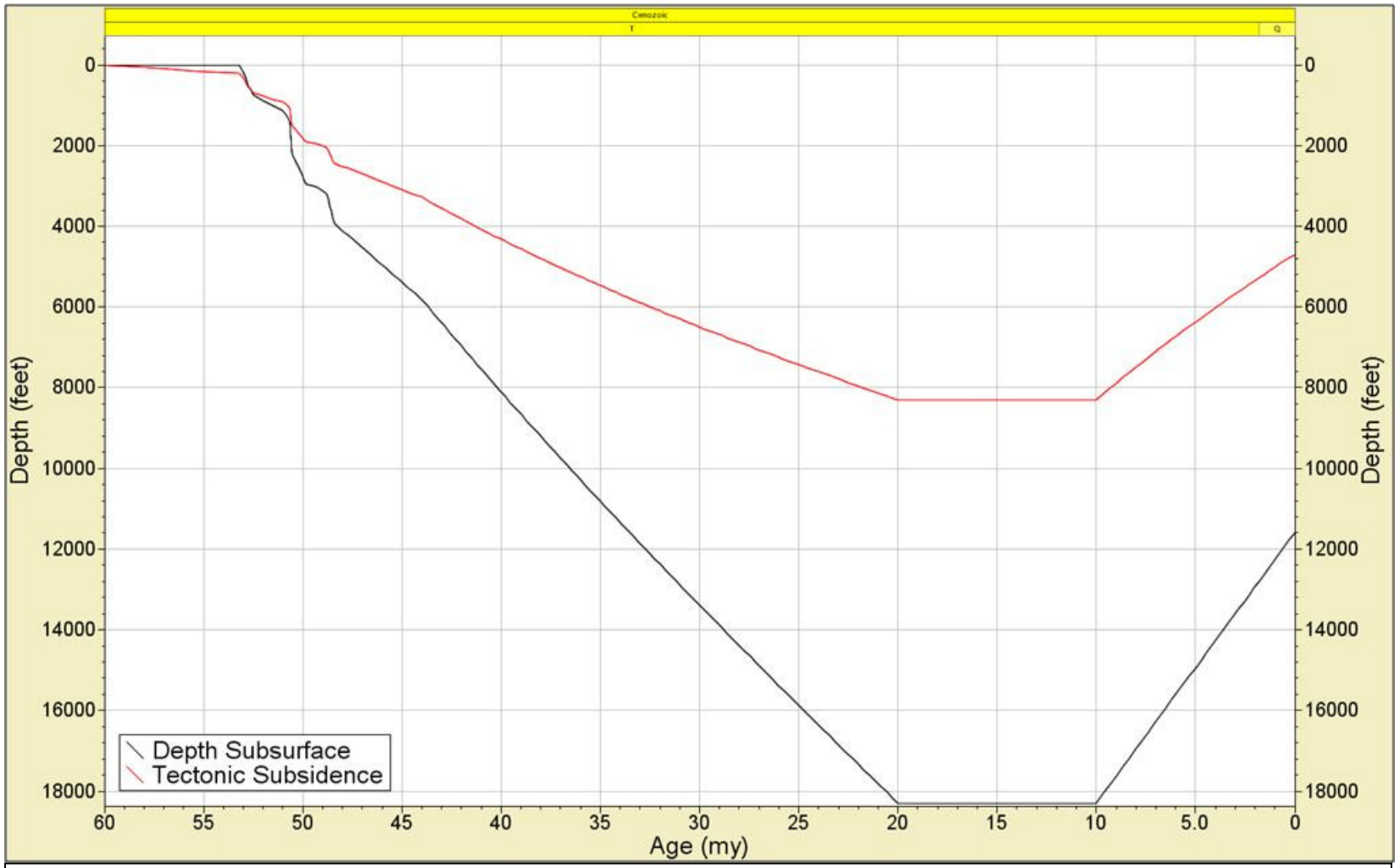


***Figure 29***: Burial history compared with tectonic subsidence at Ute 1-20Z2. Tectonic subsidence accounts for 8260 ft (2518 m) of burial prior to the onset of major uplift at this location.

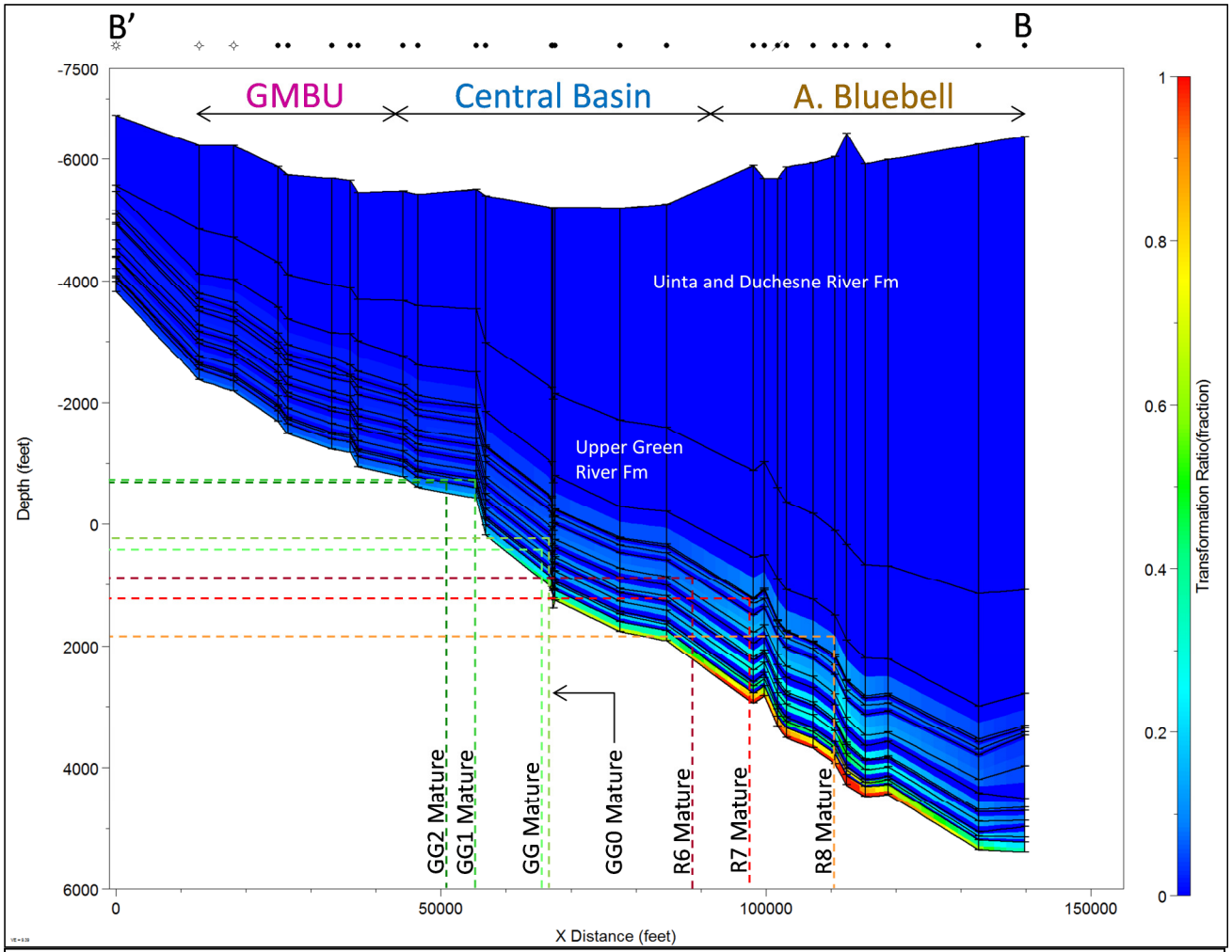


***Figure 30***: Calculated 2-D cross section of B-B' showing lateral changes in model-predicted transformation ratios. The position and depth in which each interval achieves a transformation ratio of 0.1 of greater is marked. Note depth scale is subsea.

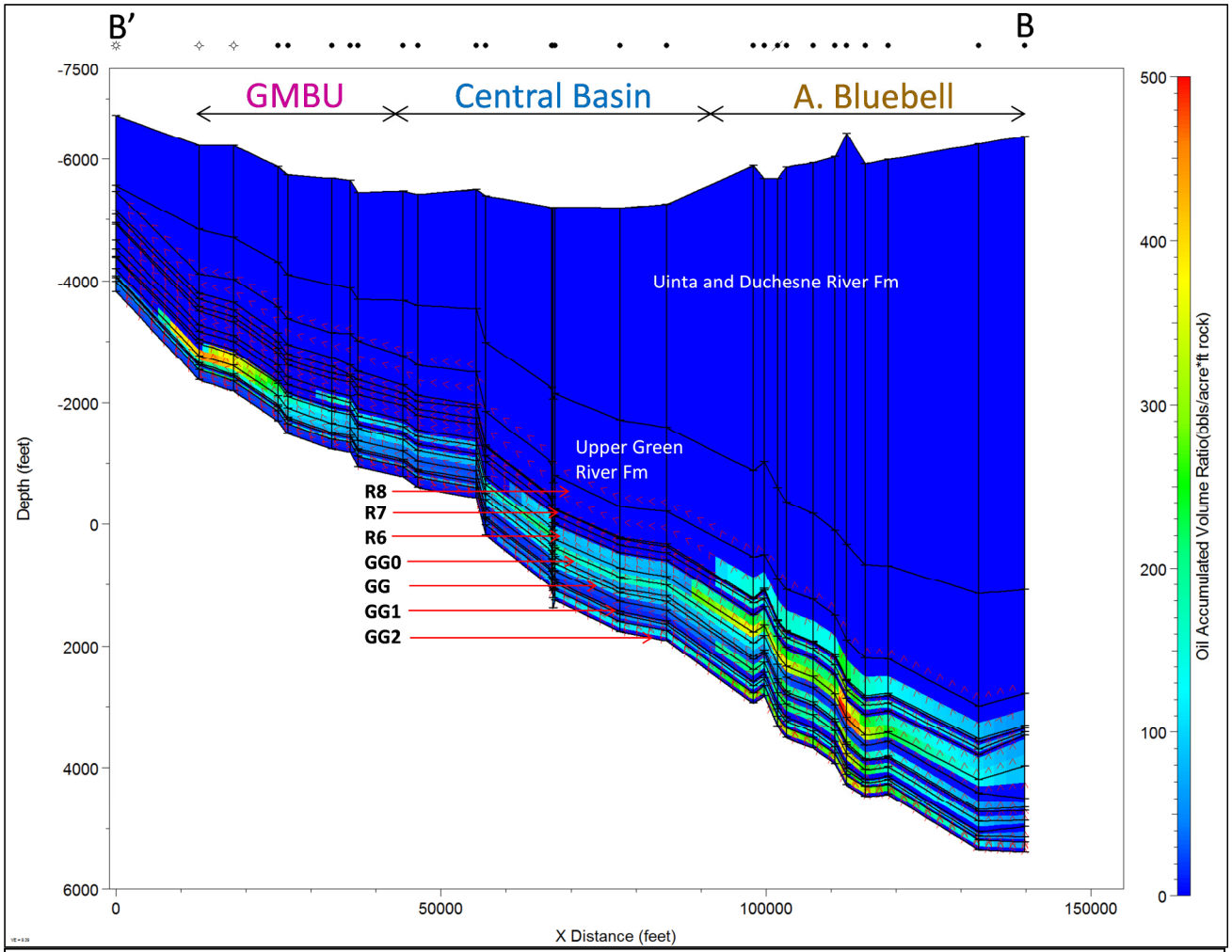


***Figure 31***: Calculated 2-D cross section of B-B' showing model-predicted migration vectors (red arrows) and oil accumulated volume ratio (bbls/ acre*ft rock).

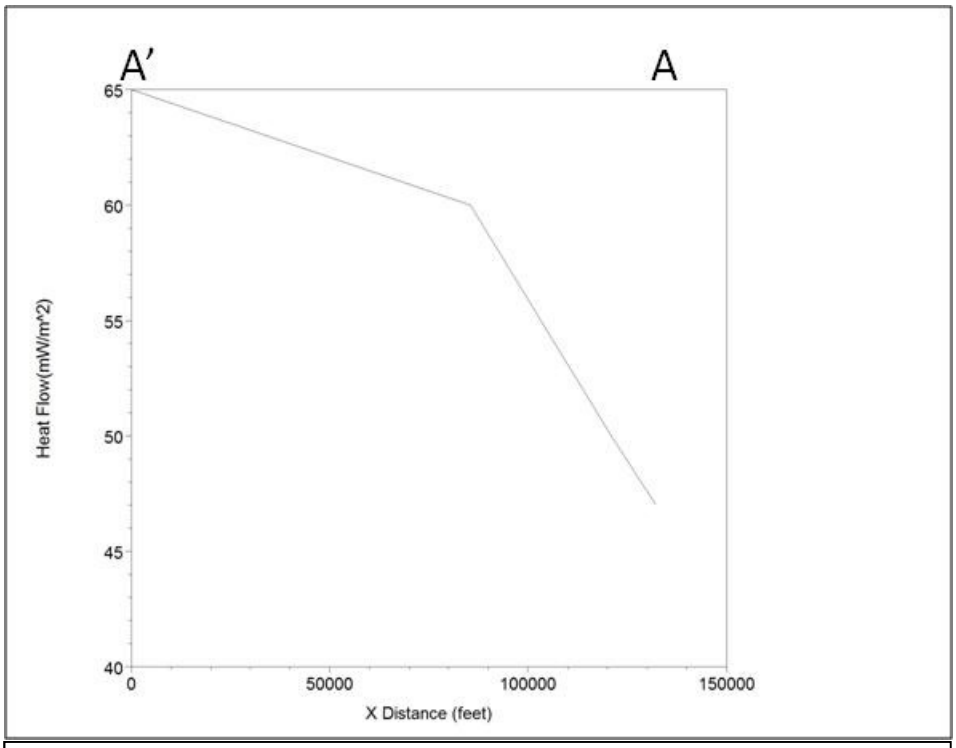


***Figure 32***: Variation in modeled heat flow along line A-A'.

the proposed range of Sweeney et al. (1987). The thermal structure for A-A' is largely reconstructed from the data of Chapman et al. (1984) and Anders et al. (1992). The variation in heat flow from south to north, constrained from these previous works, is shown in Figure 32.

The 1-D burial history for well Ute Tribal 13-31-54, located in the southern most position of A-A', is shown in Figure 33. A maximum burial depth of approximately 10800 ft (3292 m) is achieved by 20 Ma prior to major uplift and erosion at this location. Model predictions suggest that by 15 Ma, only the GG2 interval reaches maturity and the remaining source intervals are immature throughout the burial history. Figure 34 compares the burial history with tectonic subsidence for this well. Tectonic subsidence accounts for 5420 ft (1652 m) of burial prior to major uplift and erosion. The 1-D burial

history for well Blue Bench-Ute 1-7C4, located in the central portion of A-A', is shown in Figure 35. At this location, a maximum burial depth of just over 14800 ft (4511 m) is achieved by 20 Ma before uplift and erosion. Maturity is achieved by 25 Ma for interval GG2, 22.5 Ma for interval GG1, 17.5 Ma for intervals GG and GG0, 15 Ma for interval R6, and by 12.5 Ma for the Mahogany R7 interval. The R8 remains immature throughout the burial history at this location. Figure 36 compares the burial history with tectonic subsidence at this location. Tectonic subsidence accounts for 6960 ft (2121 m) of burial at this well before major uplift occurs. The 1-D burial history for well Walker 2-24A5, located in the northern most end of section of A-A', is shown in Figure 37. Here, a maximum burial depth of approximately 18400 ft (5608 m) is achieved by 20 Ma prior to major uplift and erosion. Model predictions suggest maturity is achieved around 20 Ma for interval GG2, 17.5 Ma for interval GG1, and 12.5 Ma for interval GG. The overlying GG0-R8 intervals remain immature throughout the burial predicted for this location. The burial history is compared with tectonic subsidence at this location in Figure 38. Here, tectonic subsidence accounts for 8200 ft (2500 m) of burial prior to major uplift and erosion. For all wells along A-A', the models predict that uplift due to tectonic processes accounts for roughly 3760 ft (1146 m) of uplift from 10 Ma to present. Also, predicted total subsidence and tectonic subsidence increase from south to north along A-A'.

Figure 39 is a calculated 2-D cross section of line A-A' illustrating the lateral changes in model-predicted transformation ratios. Transformation ratios increase from south to north with the largest transformation ratios existing between x distances of 70000 and 120000 ft (21336 and 36576 m), or between wells Moon Tribal 1-30C4 and Ehrich 3-11B5. This trend reverses after an x distance of about 120000 ft (36576 m)

when transformation ratios begin to decrease toward the north. Again, this is due to the effects of decreasing heat flow outweighing the effects of increased burial depths. In general, this model predicts more widespread maturity with respect to the models of B-B' and C-C'. This is likely due to the use of published heat flow values that tend to be slightly higher (from the south to the central portions of A-A') than the heat flow values determined from calibrating models to measured data. On line A-A', the southernmost position of the area associated with the greatest maturity possesses a heat flow of 61 $mW/m^2$. By comparison, lines B-B' and C-C' possess respective heat flow values of 58.2 $mW/m^2$ and 55.5 $mW/m^2$ in similar positions. In this model, interval GG2 is predicted to be mature throughout the entire section. Intervals GG1-Mahogany R7 progressively achieve maturity between the $4^{th}$ and $6^{th}$ wells from the southern end of A-A'. Interval R8 is predicted to be immature throughout the whole section. The positions and the depths along A-A' in which each of the intervals of interest achieve a transformation ratio of 0.1 or greater are summarized in Table 8.

**Table 8**: Positions and depths along B-B' in which source rocks achieve a transformation ratio of 0.1 or greater.

| Source Interval | Distance x (ft) | Depth Subsurface (ft) | Depth Subsea (ft) |
|---|---|---|---|
| R8 | Immature | Immature | Immature |
| R7 | 73500 | 5853 | -305 |
| R6 | 65950 | 5182 | -618 |
| GG0 | 62600 | 5296 | -520 |
| GG | 50050 | 4434 | -1566 |
| GG1 | 40000 | 4353 | -1781 |
| GG2 | Mature | Mature | Mature |

Figure 40 is another calculated cross section illustrating the model-predicted migration vectors and the oil accumulated volume ratio (bbls/ acre*ft rock). In general, the trends mimic those of lines B-B' and C-C' with migration occurring dominantly to overlying stratigraphic intervals within the northern portions of the section and then transitioning to primarily updip migration toward the south. Accumulations are present in zones to the north and south where source intervals are predicted to be immature due to migration within the system. To a larger degree than in previous models, A-A' predicts massive amounts of updip migration toward the south where the largest accumulations occur. This is influenced by the greater heat flow values utilized in this model.

The results of the three 2-D models are summarized in a series of maps that show how heat flow, tectonic subsidence, and model-predicted maturity for each source interval vary across the study area. Maturity maps are the byproduct of the best estimations of erosion and heat flow determined by the calibration process. Figure 41 shows the spatial variation in heat flow as determined from calibration to measured thermal indicators. Heat flow gradually decreases from the southern to central portion of the study area. Heat flow is greatest in the southeast and southwest corners and shows a slight decrease toward the south central portion of the study area. From the central to northern most portions of the study area, heat flow decreases more rapidly with distance as the Uinta Uplift is approached. However, this trend is less pronounced toward the northeast near C-C'. In the north-central area, isotherms are deflected north, resulting in greater heat flow values toward the east and west. Figure 42 is a contour map illustrating variations in predicted tectonic subsidence prior to major uplift. Tectonic subsidence

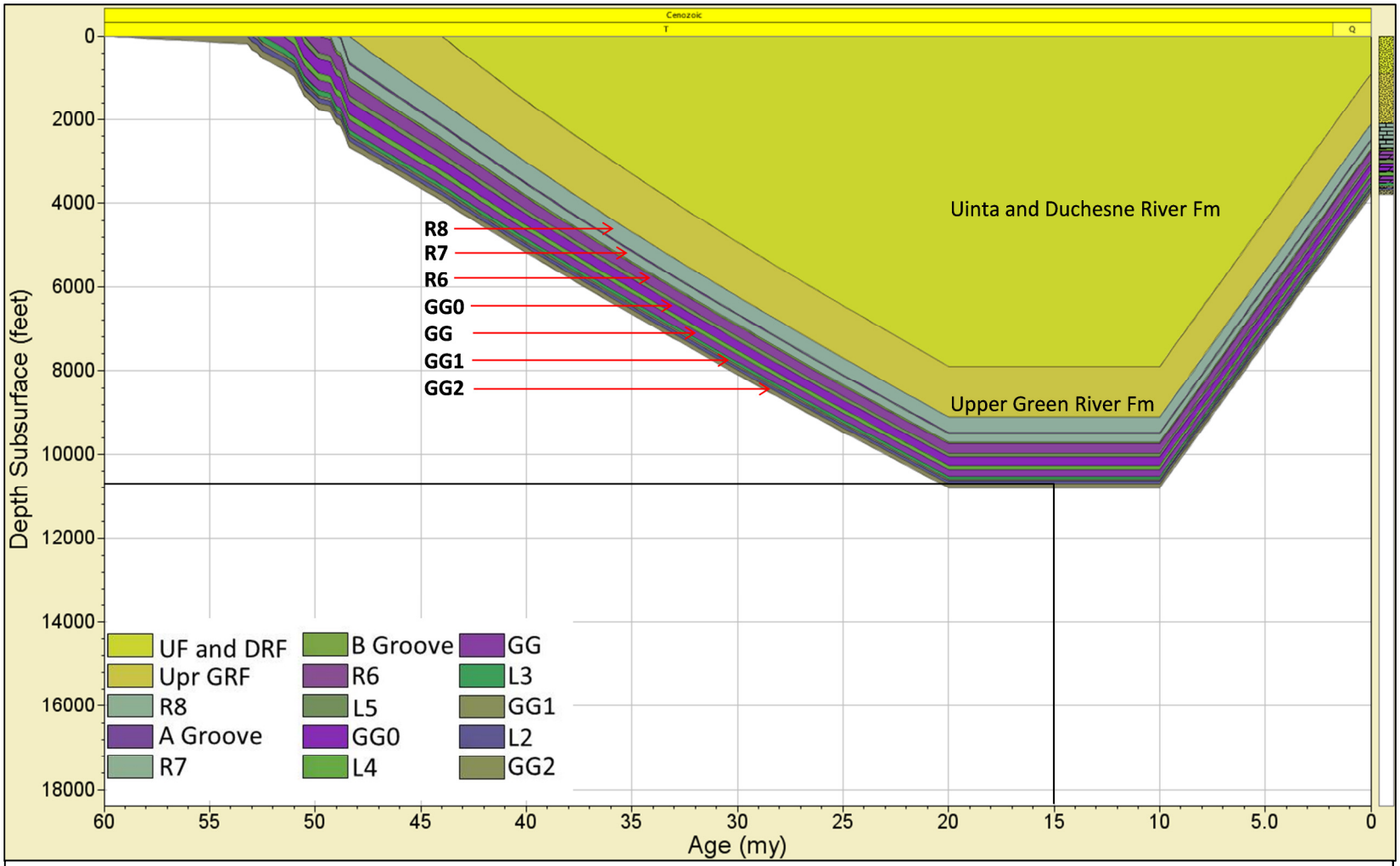


***Figure 33***: Burial history for Ute Tribal 13-31-54. The basal source interval (GG2) first enters the oil window around 15 Ma at a depth of approximately 10800 ft (3292 m).

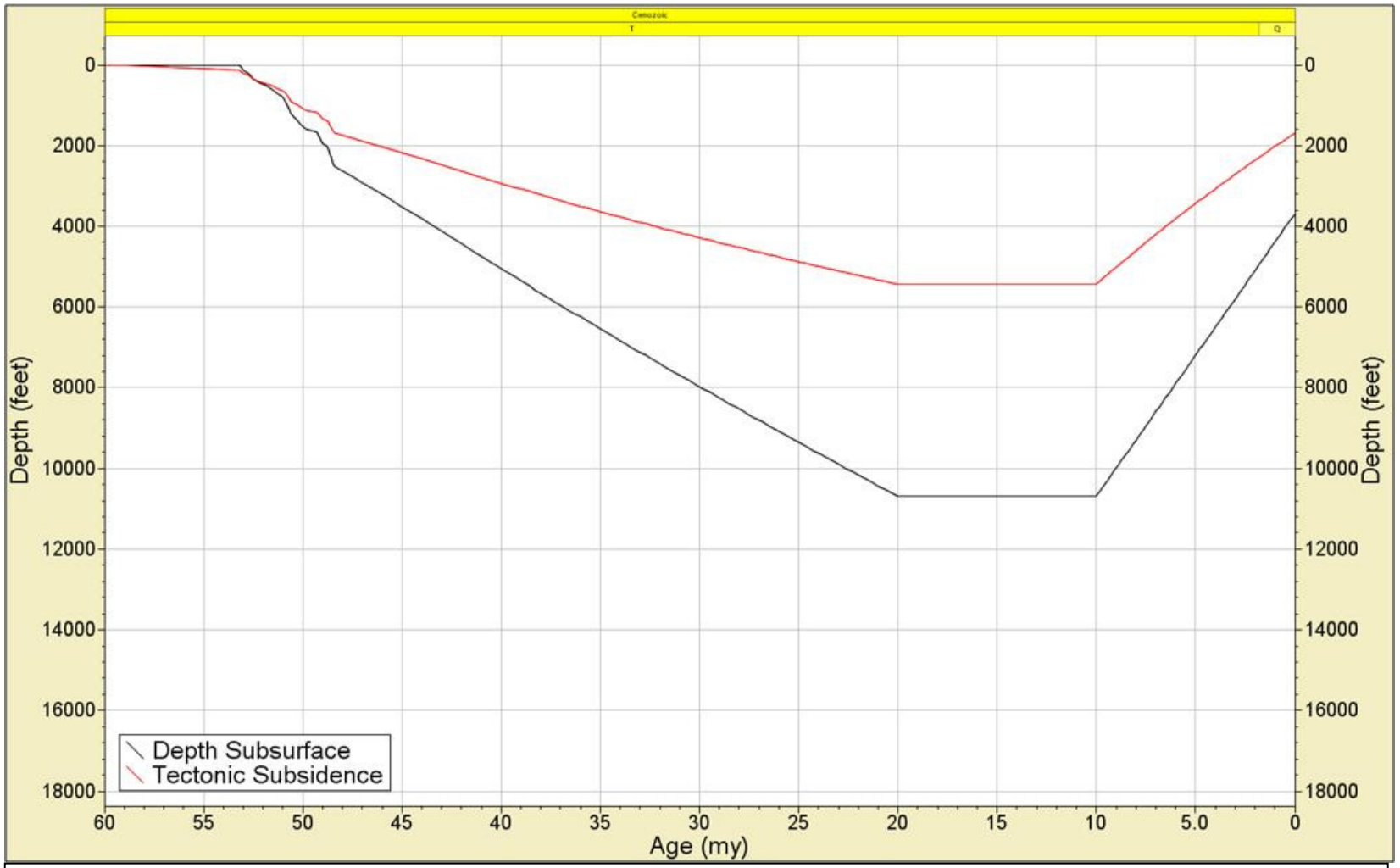


***Figure 34***: Burial history compared with tectonic subsidence at Ute Tribal 13-31-54. Tectonic subsidence accounts for 5420 ft (1652 m) of burial prior to the onset of major uplift at this location.

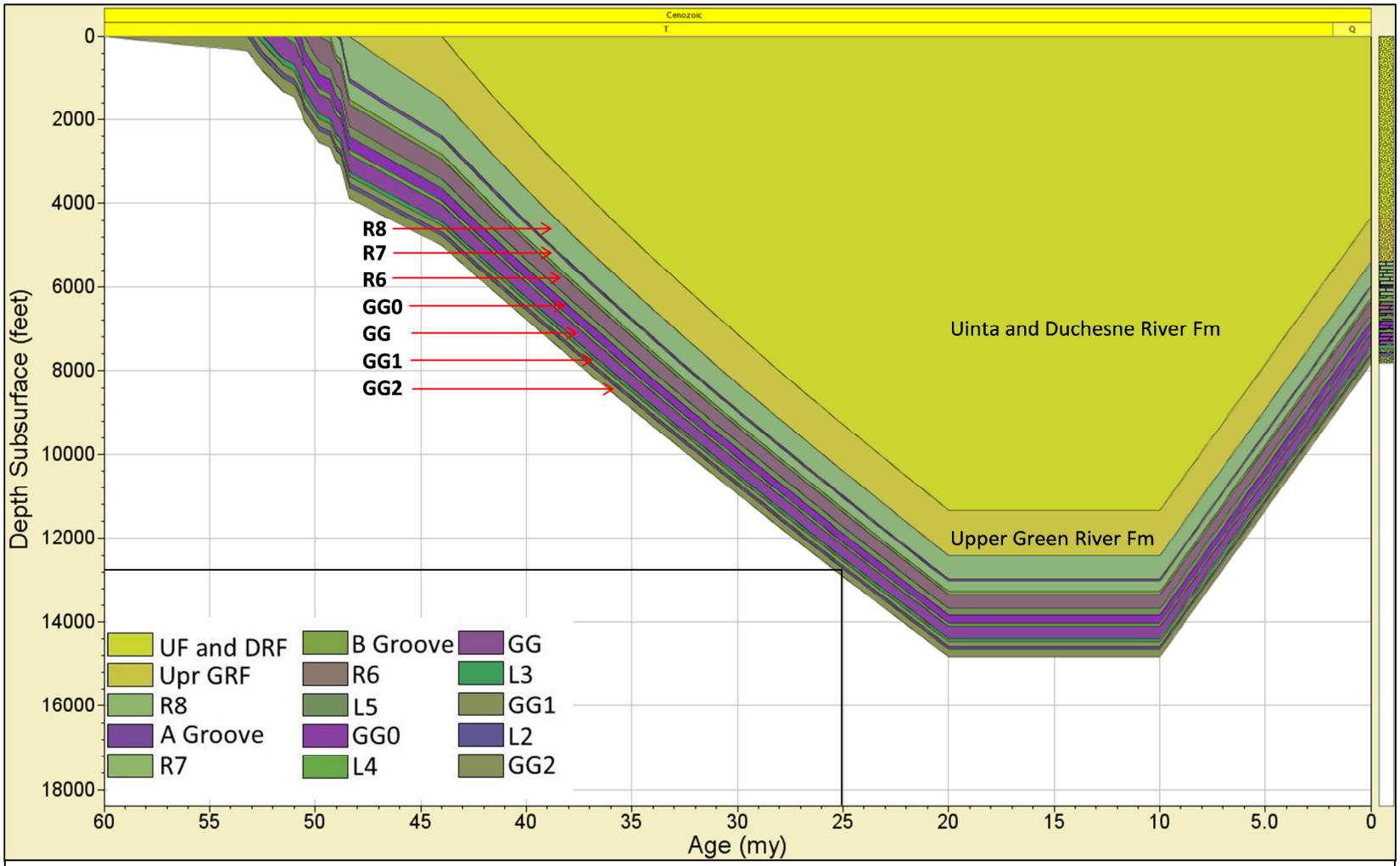


***Figure 35***: Burial history for Blue Bench-Ute 1-7C4. The basal source interval (GG2) first enters the oil window around 25 Ma at a depth of approximately 12800 ft (3900 m).


***Figure 36***: Burial history compared with tectonic subsidence at Blue Bench-Ute 1-7C4. Tectonic subsidence accounts for 6960 ft (2121 m) of burial prior to the onset of major uplift at this location.

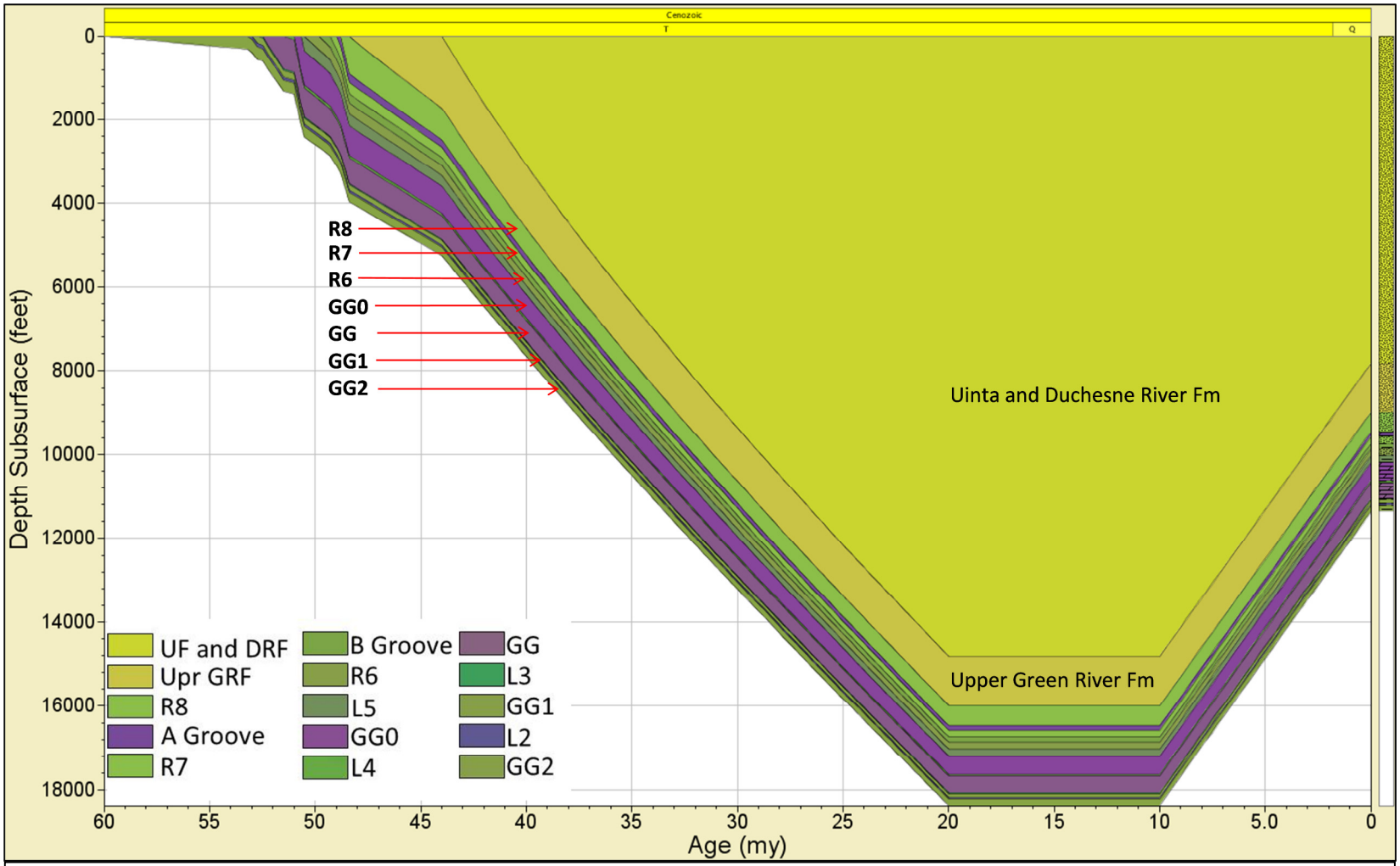


***Figure 37***: Burial history for Walker 2-24A5. The basal source interval (GG2) first enters the oil window around 20 Ma at a depth of approximately 18400 ft (5608 m).

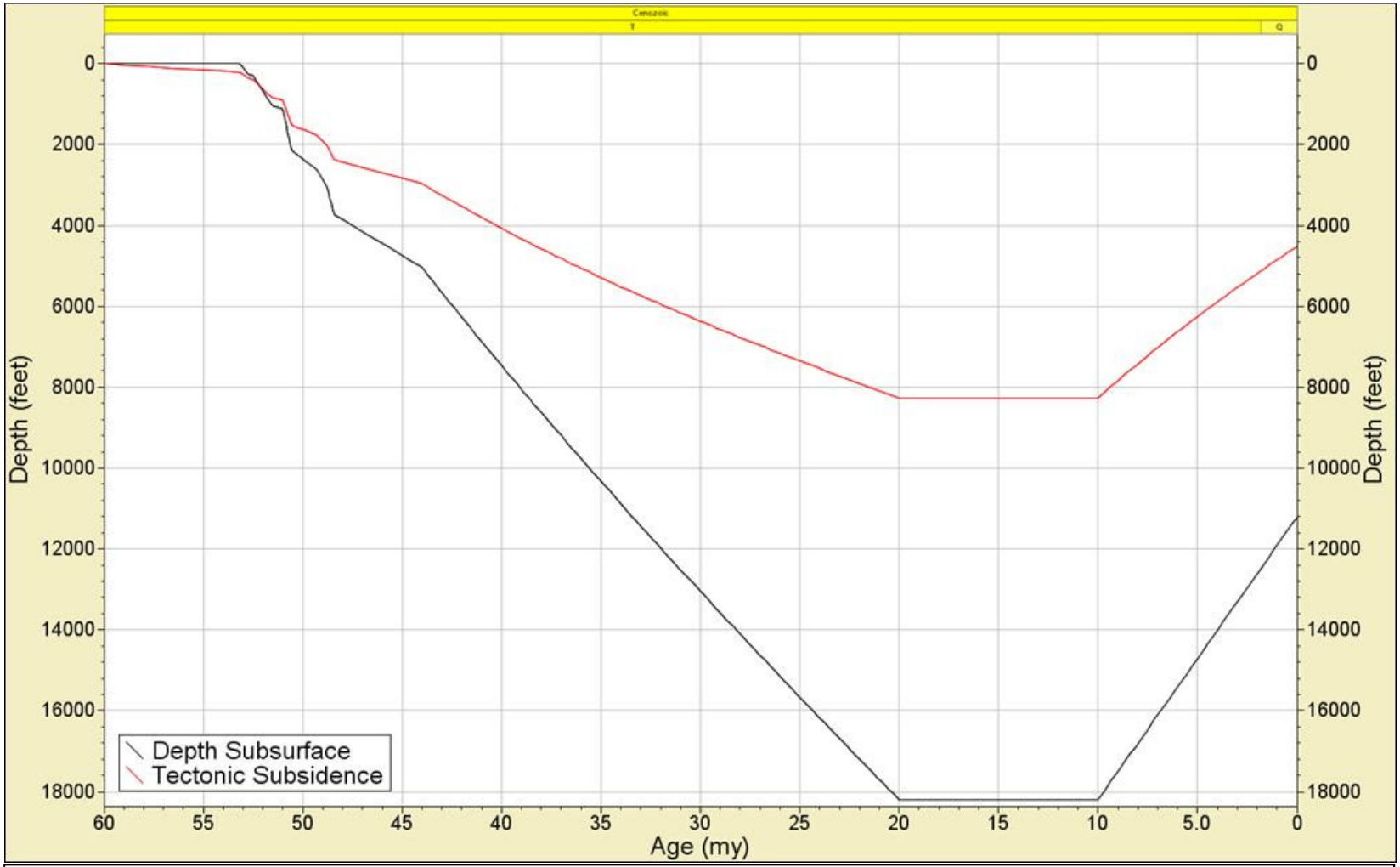


***Figure 38***: Burial history compared with tectonic subsidence at Walker 2-24A5. Tectonic subsidence accounts for 8200 ft (2500 m) of burial prior to the onset of major uplift at this location.

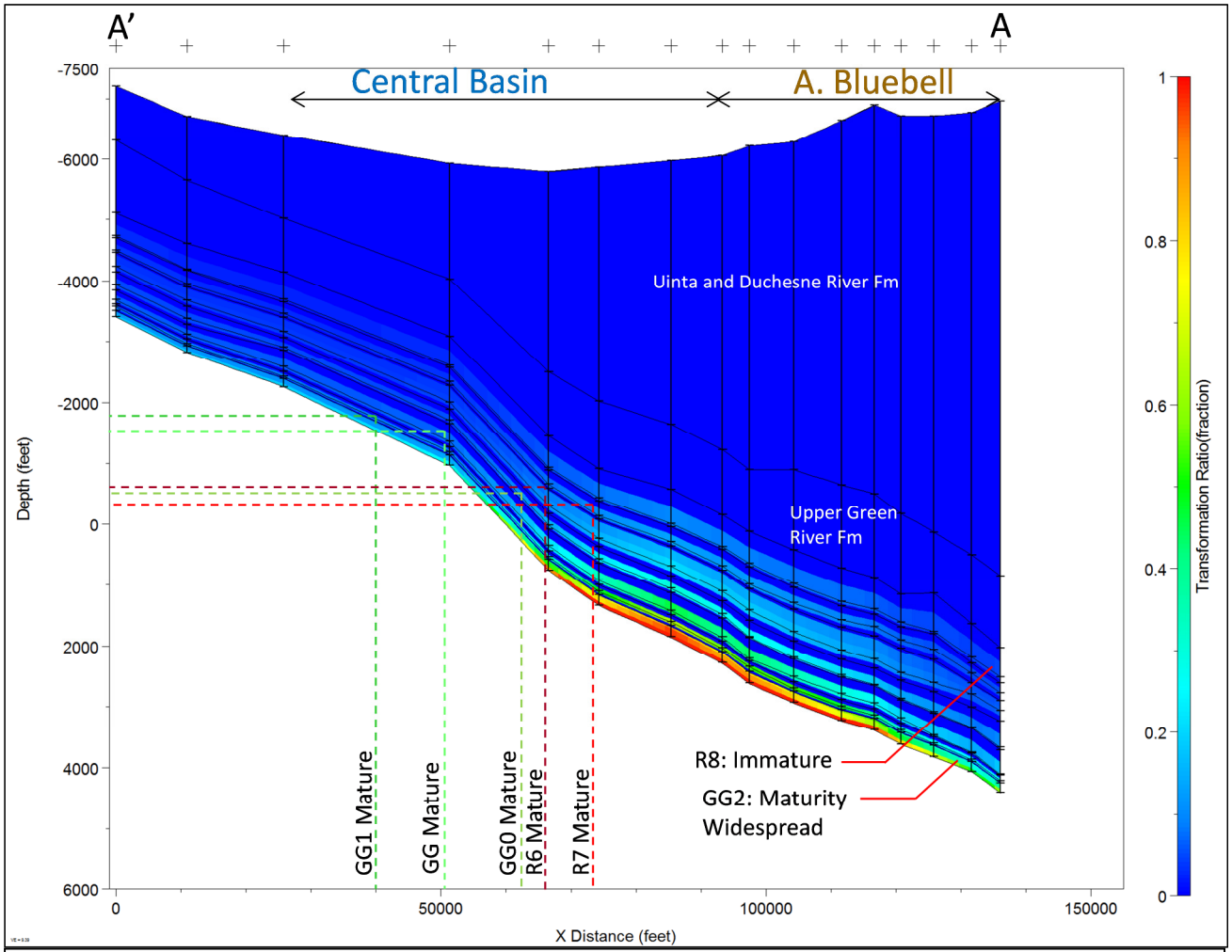


***Figure 39***: Calculated 2-D cross section of A-A' showing lateral changes in model-predicted transformation ratios. The position and depth in which each interval achieves a transformation ratio of 0.1 of greater is marked. Note depth scale is subsea.

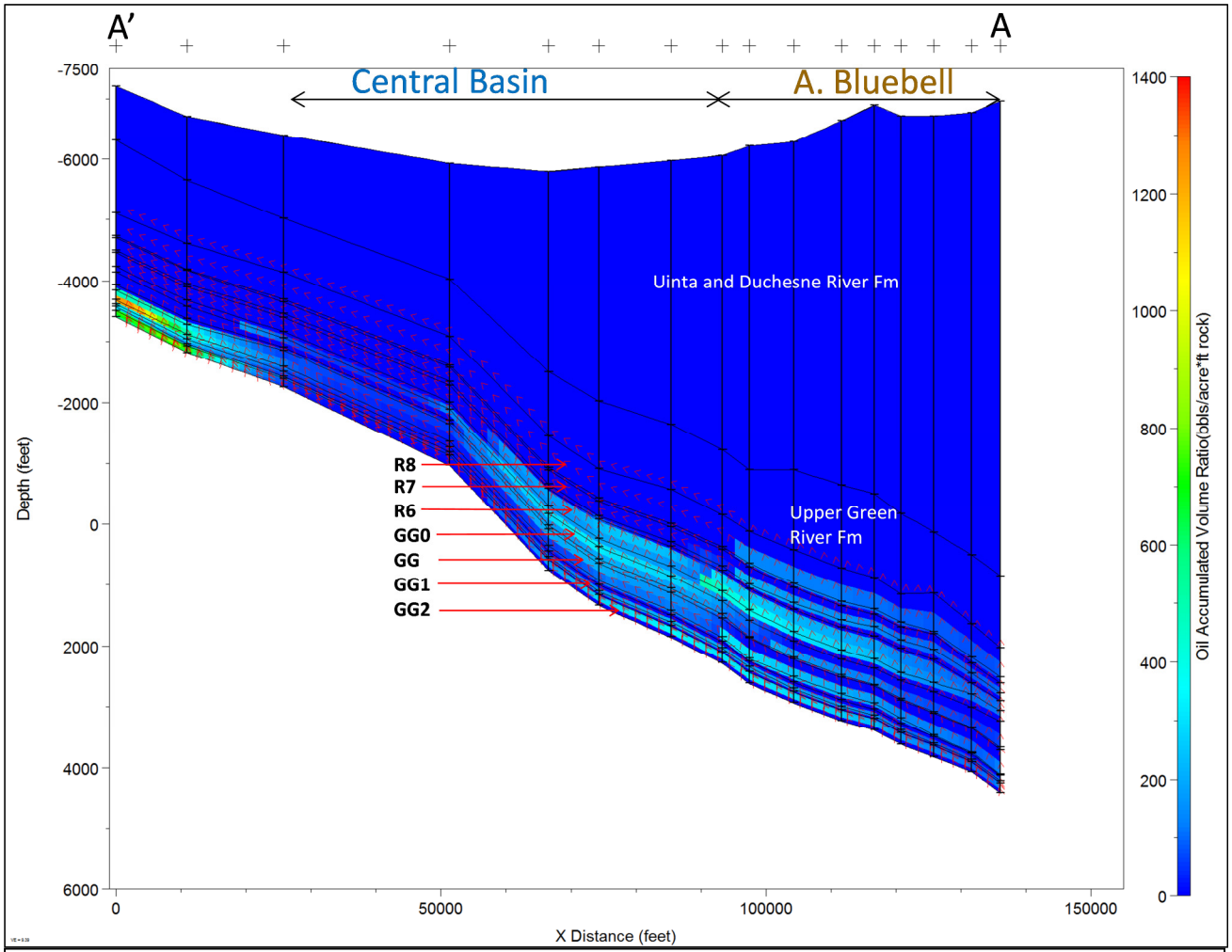


***Figure 40***: Calculated 2-D cross section of B-B' showing model-predicted migration vectors (red arrows) and oil accumulated volume ratio (bbls/ acre*ft rock).

increases from south to north with the largest subsidence occurring in the north-west corner of the study area. In general, the northern parts of A-A' and B-B' have experienced the largest tectonic subsidence. Also, these areas correspond to the lowest heat flow values. Conversely, the northern part of C-C' experienced slightly less tectonic subsidence and higher heat flow (compare figures 41 and 42).

### 4.4 Maturity Trends of the Uinta Basin

Model-predicted maturity for the GG2 source interval suggests that this source bed has reached temperature conditions to generate hydrocarbons throughout most of the study area. Predicted maturity is far reaching from the north to the south-east and south-west portions of the study area. The south-central area is predicted to be immature and corresponds with the lower heat flow fairway that extends through the south central portions of the study area (Figure 43). Model-predicted maturity for the GG1 source interval suggests that this source interval is largely mature through the study area as well. This source interval shows similar trends to GG2, but with a larger area of predicted immaturity toward the south (Figure 44). Model-predicted maturity for the GG source interval suggests that this source bed remains largely immature in the southern third of the study area, including the Greater Monument Butte oil field. The GG interval is predicted to be mature from the eastern and western portions of the central basin area (blue outline) to just south of the northern extent of the study area (Figure 45). Model-predicted maturity for the GG0 source interval suggests that this source bed is immature across the entire southern half of the study area. Maturity is restricted to the areas north of the central portions of the central basin area except in small zones near the northern

extent of lines A-A' and B-B'. These northern zones of immaturity correspond to the lowest predicted heat flow values (Figure 46). Model-predicted maturity for the R6 source interval suggests that this source interval possesses maturity that is restricted to the northern third of the study area, which includes the area that spans from the northern portions of the central basin area to the Altamont Bluebell oil field. With respect to the GG0, a larger zone of immaturity also exists in the north central and northwest portions of the study area. This is due to the low heat flow values associated with this area but it also driven by the shallower burial depths associated with the R6 interval (Figure 47). Model-predicted maturity for the Mahogany R7 source interval indicates that this source rock is largely immature throughout the study area except in select areas associated with the northwest corner of central basin, the central portions of the Altamont Bluebell oil field, and a small area in the eastern most portion of the Altamont Bluebell oil field. Maturity of this source rock is largely affected by the rapid decrease in heat flow toward the north. For areas with higher heat flow, this interval is not buried to sufficient depth to generate hydrocarbons. Alternatively, in zones where it may be buried deep enough to generate hydrocarbons, the effects of the decreasing heat flow quickly outweigh the effects of increased burial depth from south to north. As a result, only a small window of maturity exits, which is dictated by the burial depth and heat flow conditions (Figure 48). Model-predicted maturity for the R8 interval suggests that this interval remains immature throughout the entire study area except for a small region along B-B'. Model predictions suggest that this interval never experienced sufficient burial depth and heat flow to generate significant hydrocarbons (Figure 49).

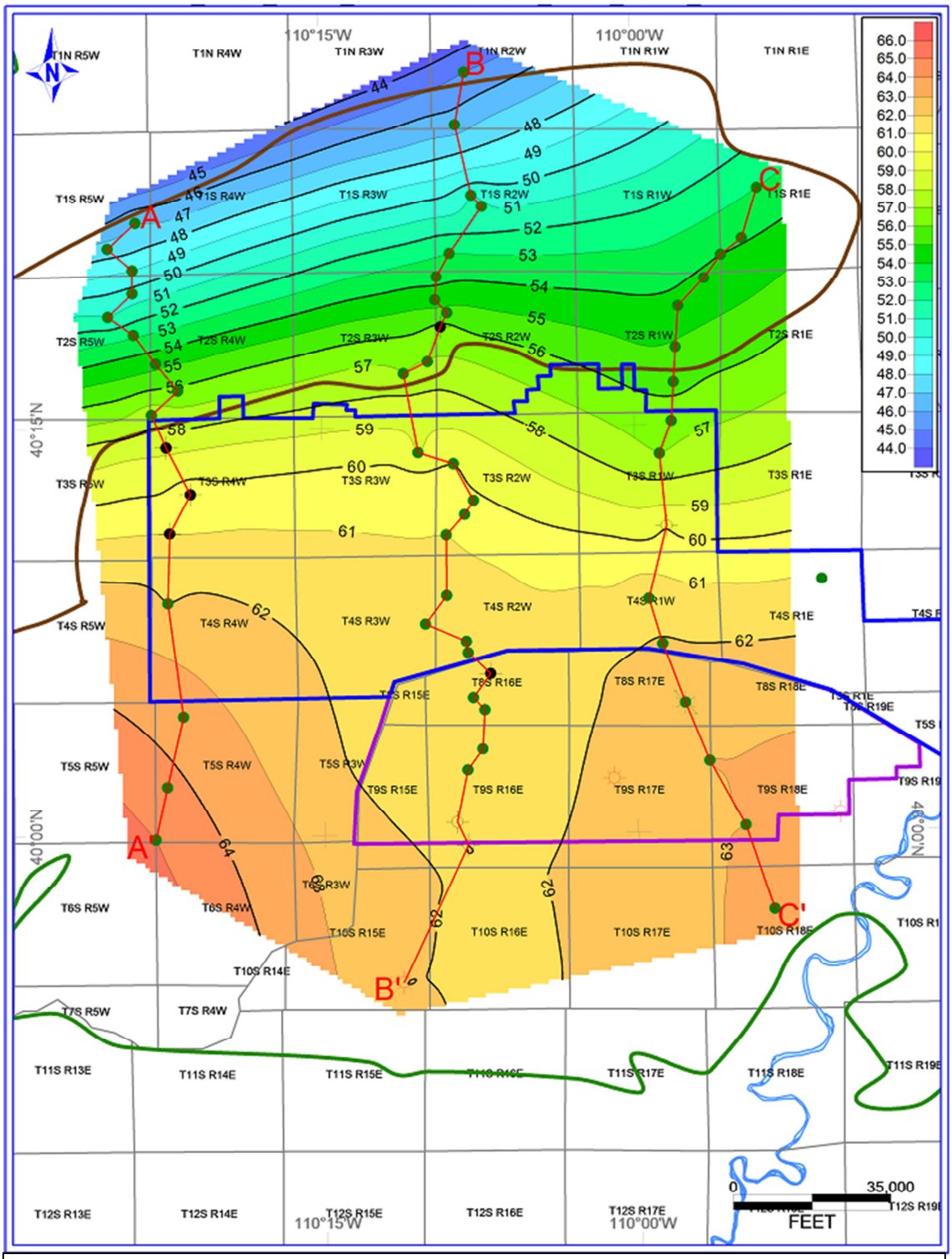


***Figure 41***: The spatial variation in heat flow ($mW/m^2$) as determined from calibration to measured thermal indicators.

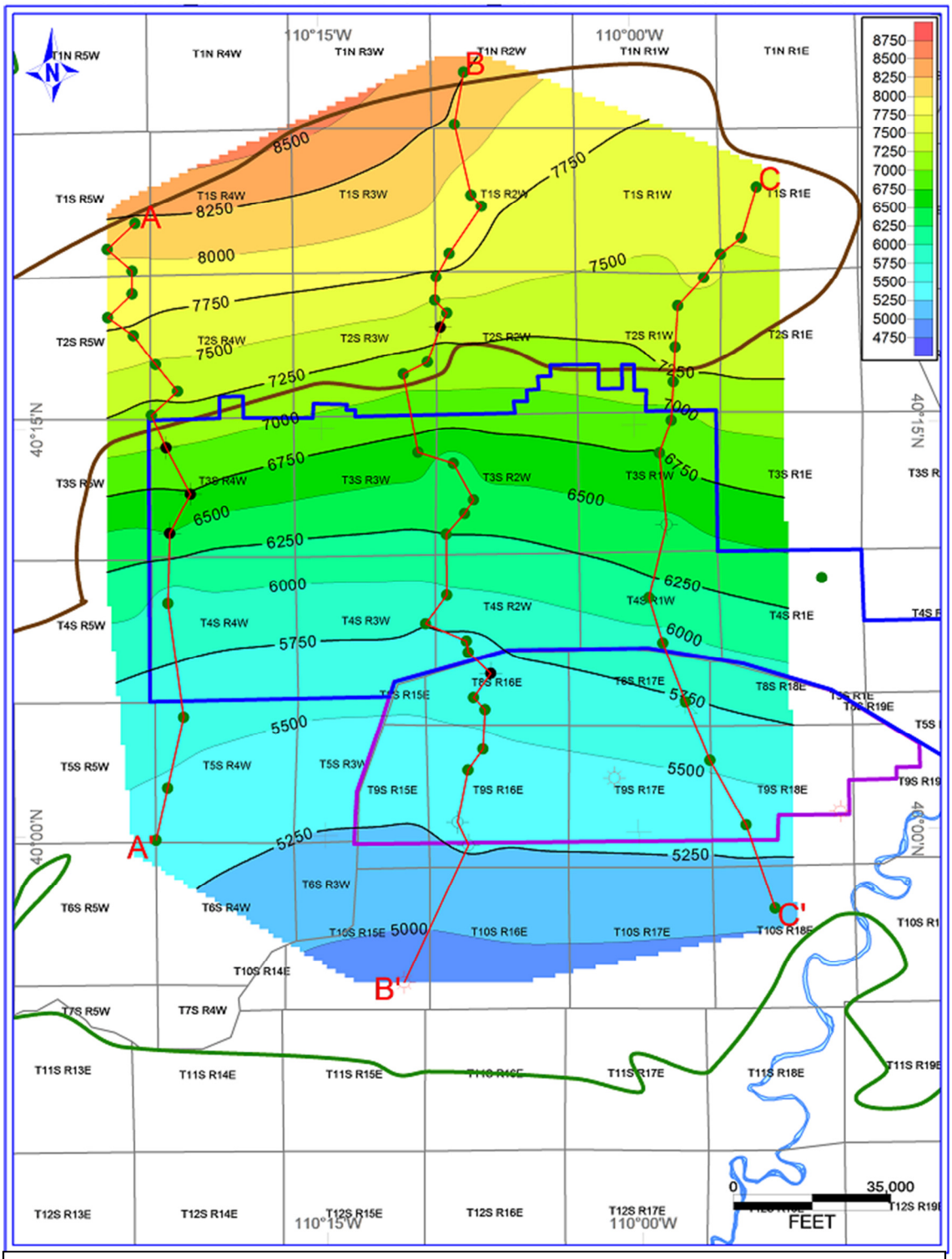


***Figure 42***: Variations in predicted tectonic subsidence (ft) prior to major uplift.

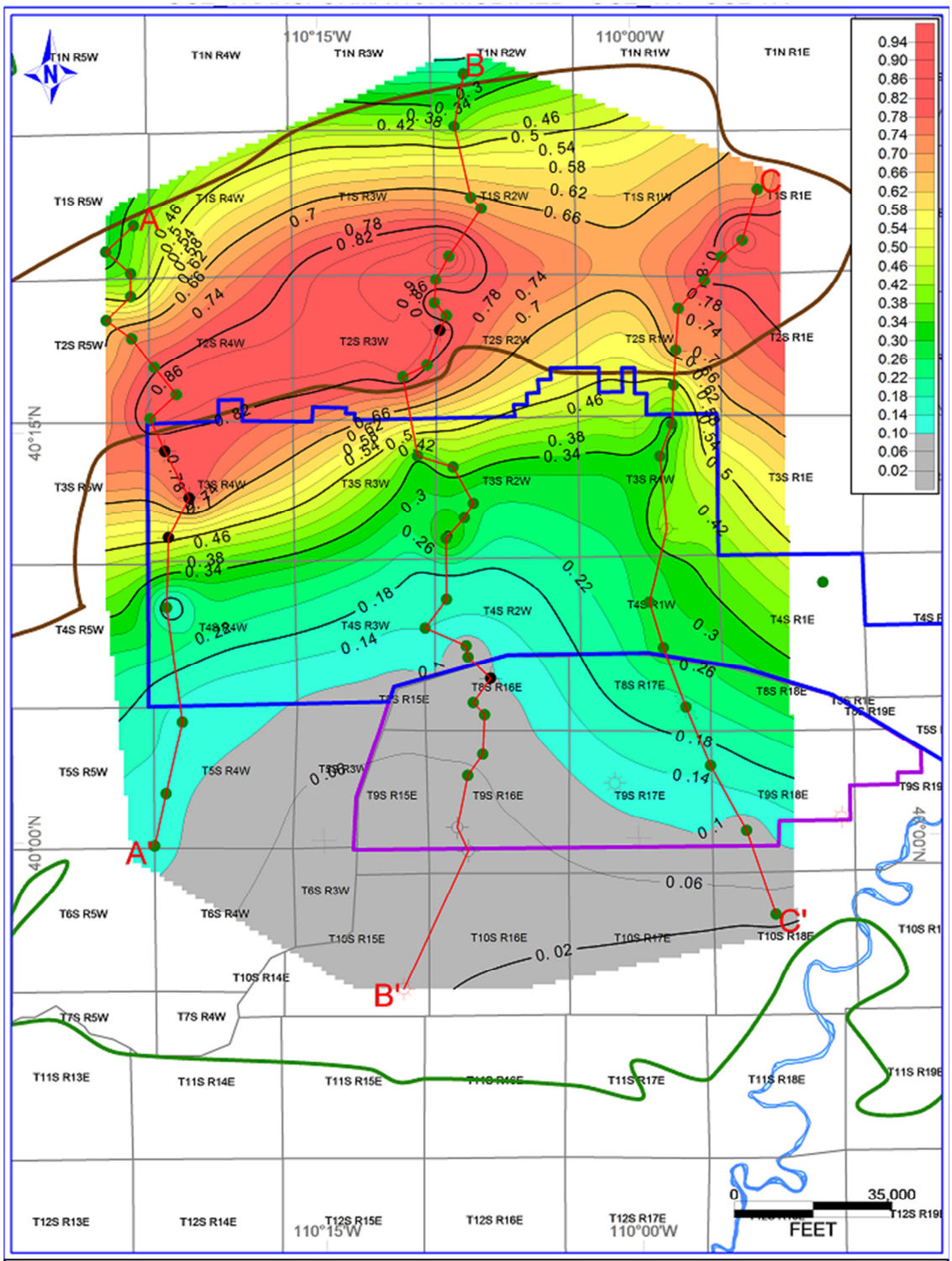


***Figure 43***: Spatial distribution of model-predicted transformation ratios for interval GG2. Transformation ratios of 0.1 or greater are considered mature. The grey area represents immature source rock.

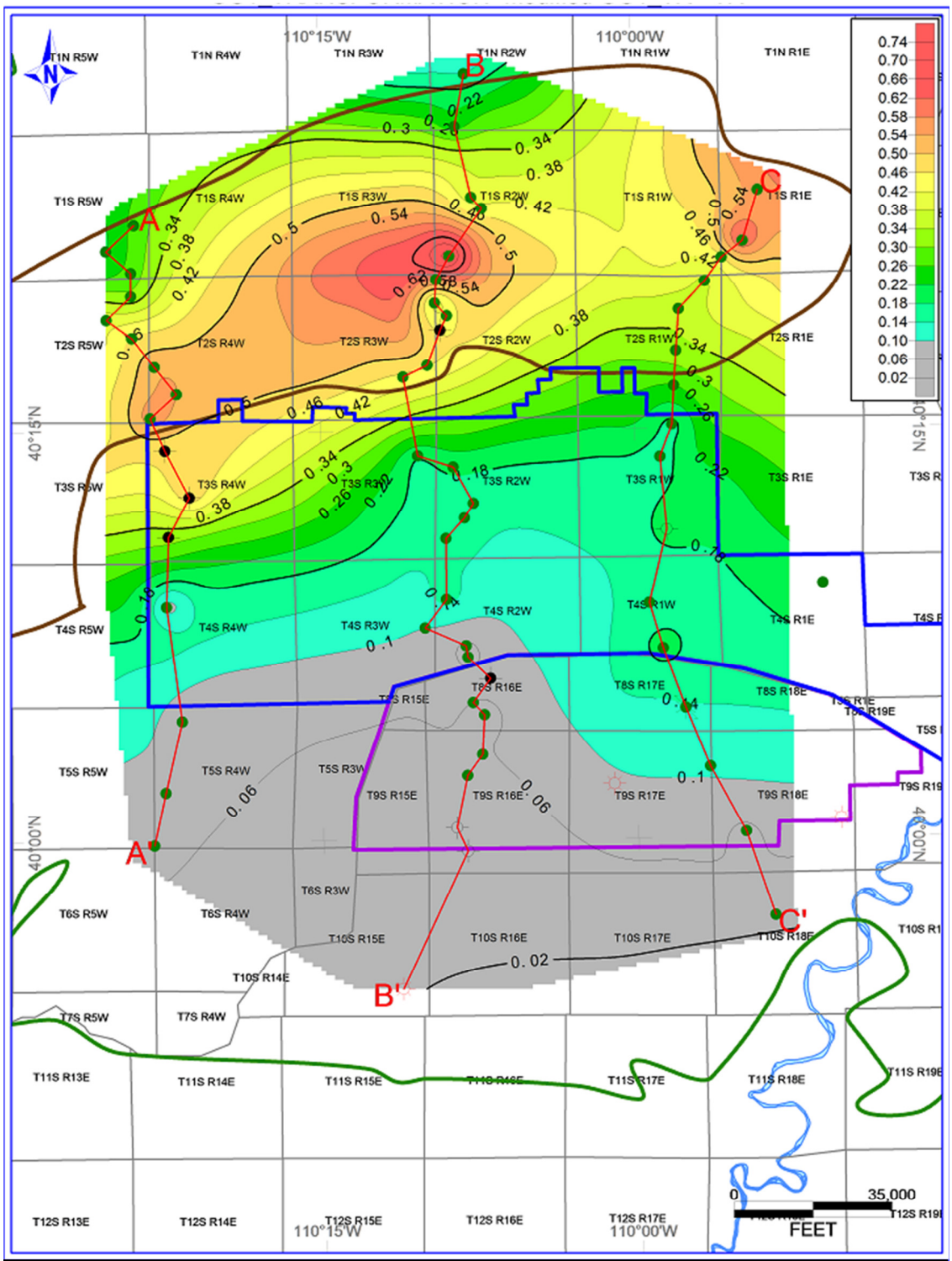


***Figure 44***: Spatial distribution of model-predicted transformation ratios for interval GG1. Transformation ratios of 0.1 or greater are considered mature. The grey area represents immature source rock.

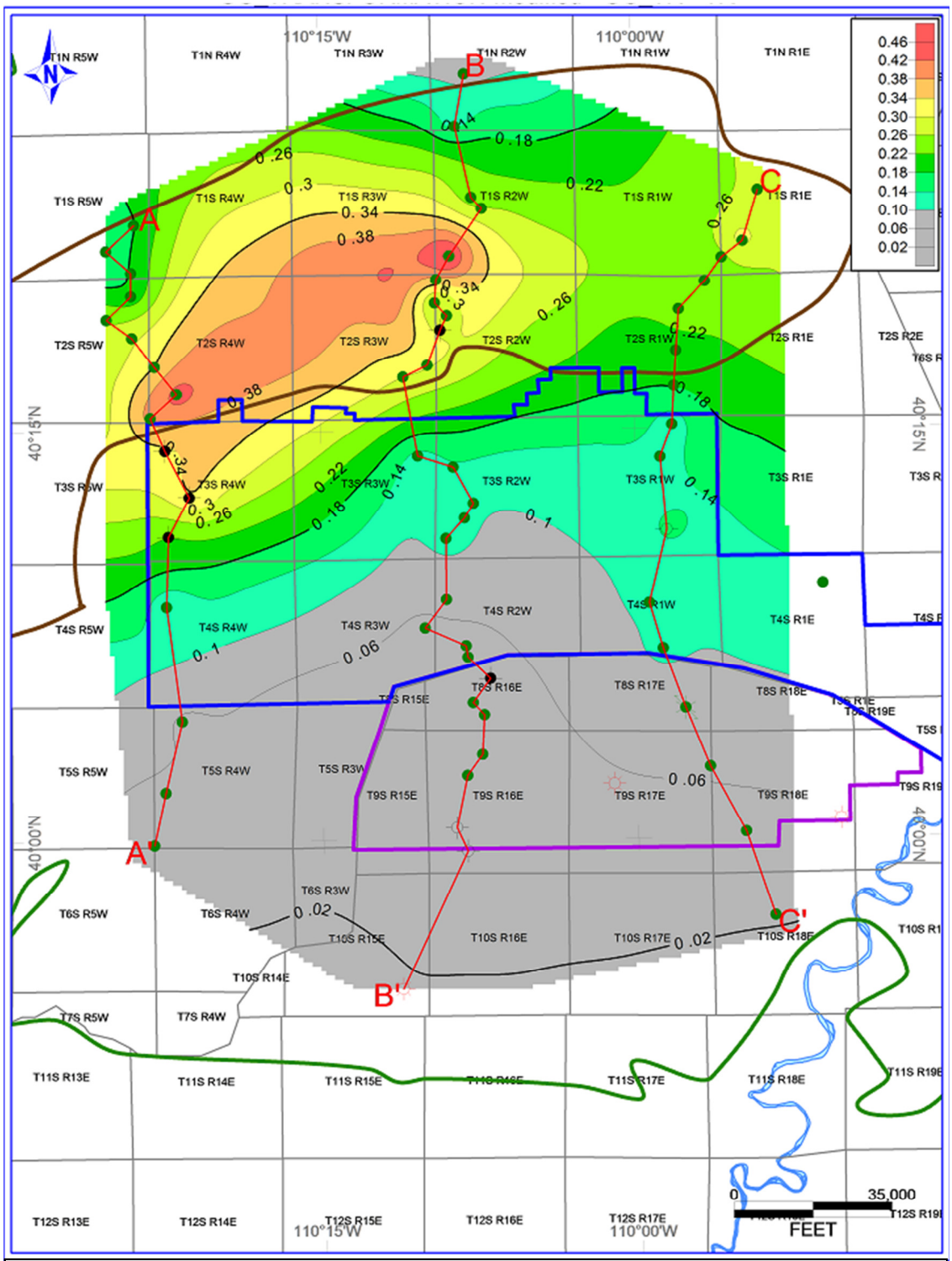


***Figure 45***: Spatial distribution of model-predicted transformation ratios for interval GG. Transformation ratios of 0.1 or greater are considered mature. The grey area represents immature source rock.

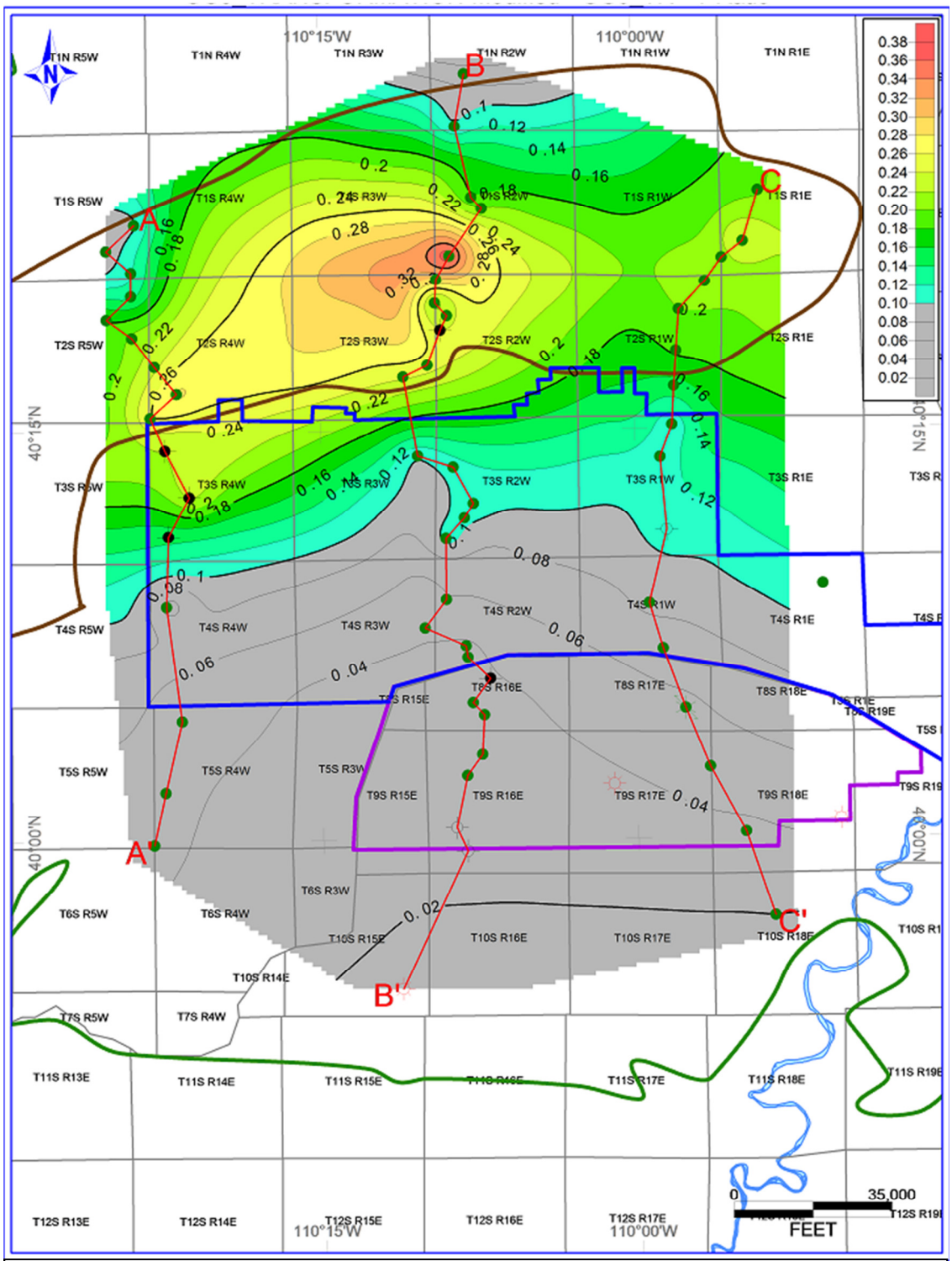


***Figure 46***: Spatial distribution of model-predicted transformation ratios for interval GG0. Transformation ratios of 0.1 or greater are considered mature. The grey area represents immature source rock.

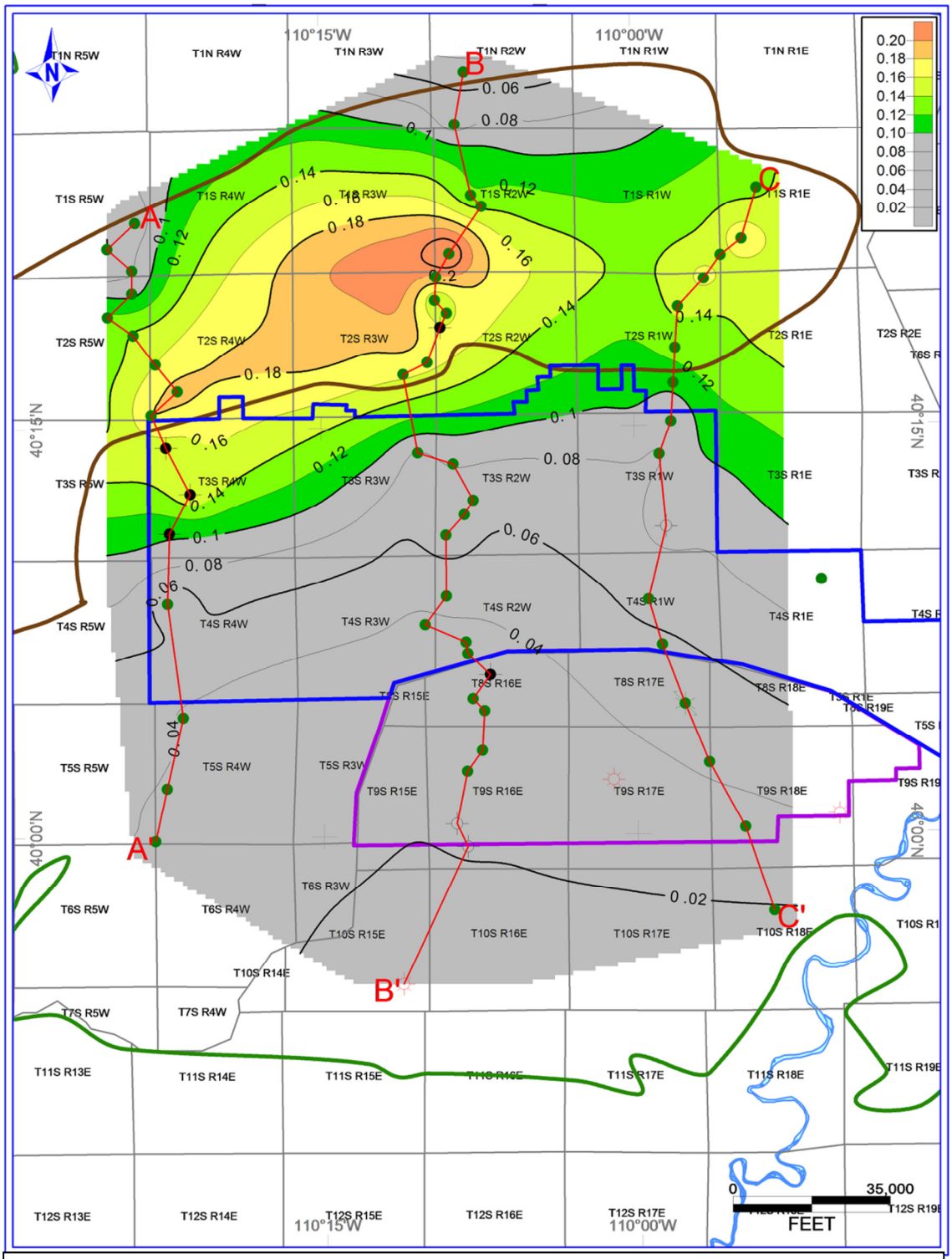


***Figure 47***: Spatial distribution of model-predicted transformation ratios for interval R6. Transformation ratios of 0.1 or greater are considered mature. The grey area represents immature source rock.

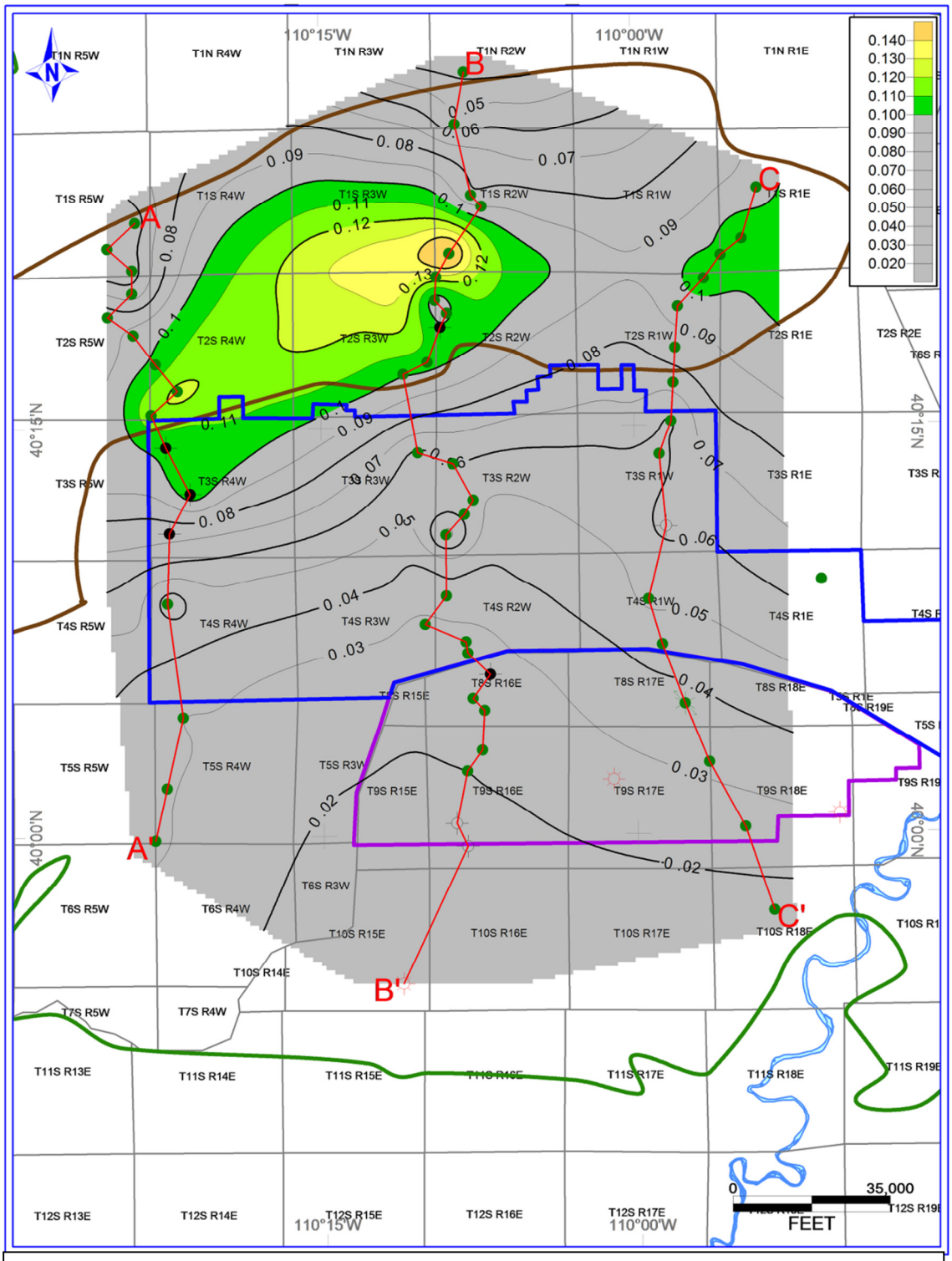


***Figure 48***: Spatial distribution of model-predicted transformation ratios for interval R7. Transformation ratios of 0.1 or greater are considered mature. The grey area represents immature source rock.

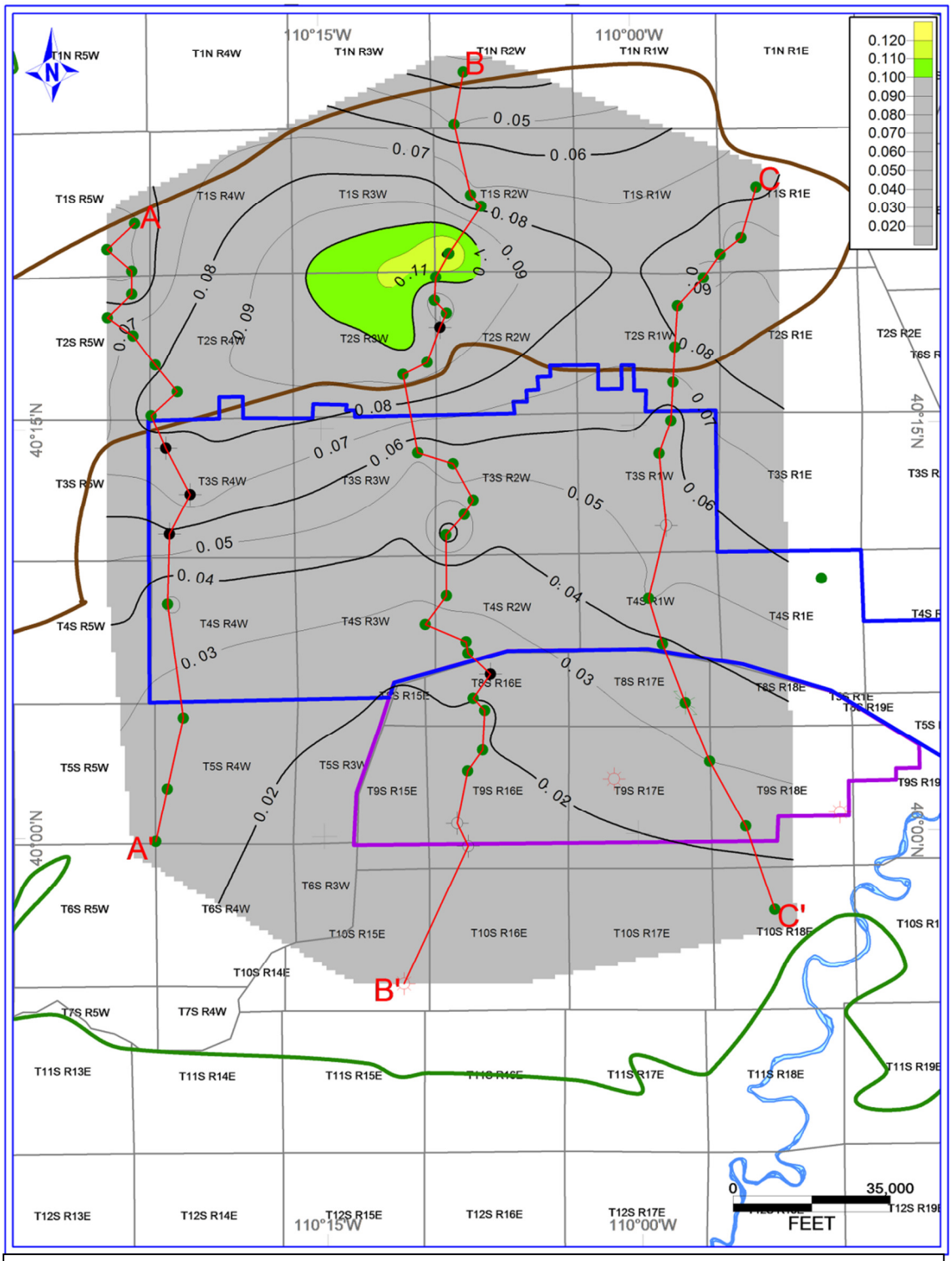


***Figure 49***: Spatial distribution of model-predicted transformation ratios for interval R8. Transformation ratios of 0.1 or greater are considered mature. The grey area represents immature source rock.

## CHAPTER 5: Discussion

### 5.1 Uplift and Erosion of the Northern Colorado Plateau

Calibration of the 2-D models provides a means for which uplift and erosion can be estimated in the Uinta Basin. As previously discussed, preceding estimations for the amount of uplift and erosion range from 1000 – 11000 ft (305 – 3353 m) depending on the researcher. Present day heat flow values and geothermal gradients are well constrained from the works of Chapman et al. (1984), Anders et al. (1992), and Swanberg and Morgan (1985). The "average" paleo-geotherms determined from the model calibration process match reasonably well with the present day geotherms with the eroded thicknesses from the best-case scenario. This satisfies the assumption that heat flow has not changed significantly throughout the Uinta Basin's burial history. Temperature vs. depth profiles predicted from modeled heat flow values are compared with present day geotherms determined by Anders et al. (1992) in Figure 50. As a result, eroded thicknesses that yield a thermal structure that falls within the accepted range established by previous workers and generates a match between predicted and measured maturity, may be considered geologically reasonable. The results discussed in the previous section represent the uplift/erosion and thermal structure that yielded model-predicted maturity that best matches with measured maturity indicators and satisfies the assumption that heat flow has not changed significantly throughout the Uinta Basin's Cenozoic history. During the calibration process, multiple iterations were attempted with various uplift/erosion values and heat flow was adjusted to bring forth agreement between predicted and measured data. Although our results describe the best-fit match between measured and predicted maturity based on the assumption that heat flow is constant through time, there

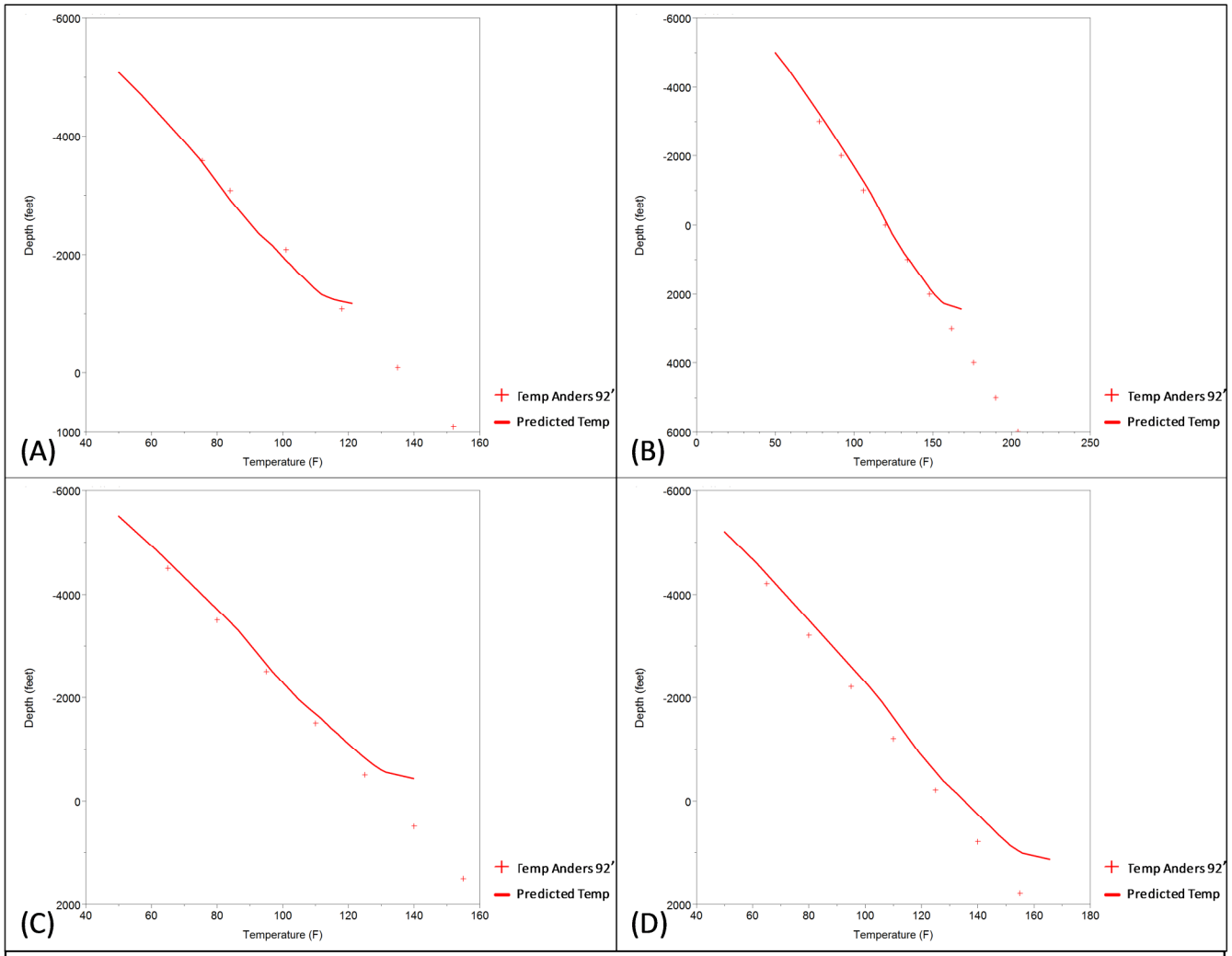


***Figure 50***: Predicted thermal gradients compared with thermal gradients of Anders et al. (1992) at wells Federal 12-7-9-18 (A), Dillman 5-2-3-1W (B), Ute Tribal 15-13-4-3W (C), and Murphy 2-31-3-2W (D).

also exists a range of values that we consider geologically reasonable which largely result in the same maturity predictions. Although these input values did not necessarily produce the best match with measured data (described in the results), they matched extremely well and provide some insight into an acceptable range of estimated eroded thicknesses that characterize the Uinta Basin. If a given amount of erosion yielded a heat flow estimation that is reasonably close to heat flow determined from previous researchers, then this estimate of erosion is considered geologically reasonable. A proposed range of reasonable estimates of erosion and corresponding heat flow values for the Uinta Basin is shown in Figure 51 along with iteration attempts that fall outside the reasonable range. Reasonable estimates of erosion range from 6000 – 7200 ft (1830 – 2195 m) and correspond to heat flow values of 61-66 $mW/m^2$ within the regions of the study area where measured data is available. Cases with higher heat flow values correspond with lower amounts of erosion along the trend shown in Figure 51. If the average paleogeotherm is greater than the present day geotherm, then less erosion is required to give rise to the same maturity situation. As a result, it is possible that less erosion may have occurred than suggested by the best case scenario if heat flow was higher in the past. Generally, these heat flow values are close to those determined by previous researchers in the study area. However, some amounts of estimated erosion yielded heat flow values and average paleogeotherms that may be too high or low for the areas where measured geochemical data is available. For example, an iteration was attempted on line C-C' with 5700 ft (1737 m) of erosion. The heat flow required to obtain a match with the measured data was 75 $mW/m^2$, which is likely too high. As a result, 5700 ft (1737 m) of erosion is considered unreasonable. Alternatively, in an iteration on line B-B', 7600 ft

(2316 m) of erosion was attempted. Heat flow required to obtain a match with the measured data was 54 $mW/m^2$, which is too low when compared with present day heat flow measurements from the study area. The different scenarios represented by Figure 51 result in virtually identical maturity predictions, and therefore provide a range of reasonable eroded thicknesses and heat flow values that may characterize the Uinta Basin.

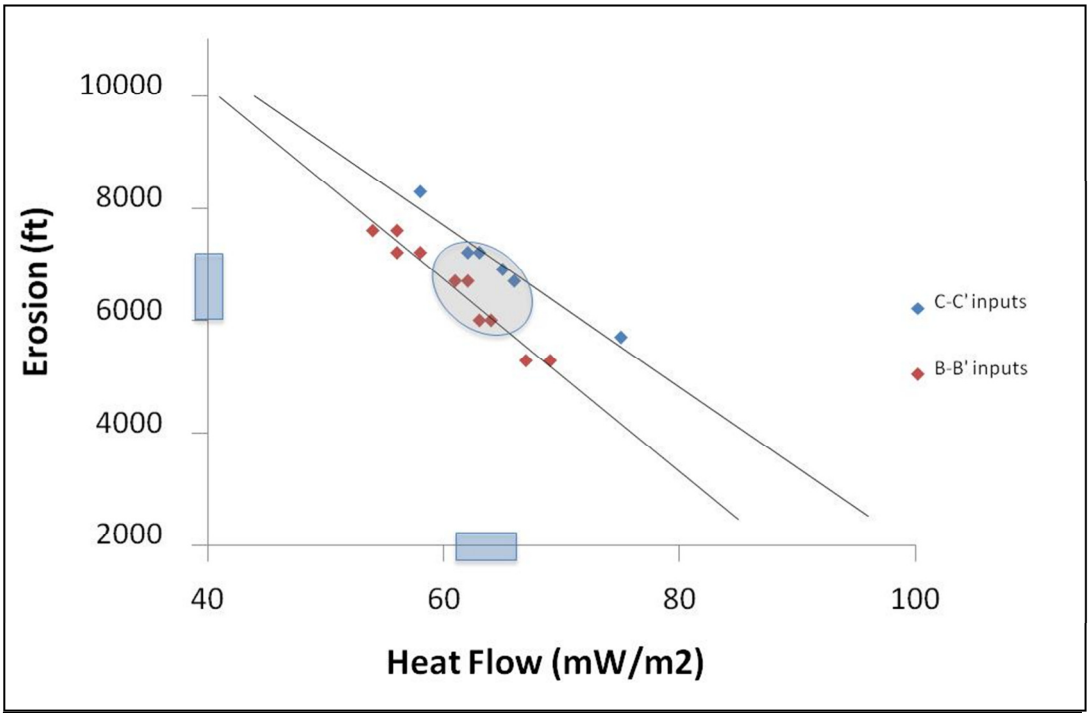


***Figure 51***: Erosion and corresponding heat flow values from various model iterations. The grey oval represents iterations that required reasonable values for heat flow and erosion to bring forth agreement between model-predicted and measured maturity.

Estimations of uplift and erosion determined from this study most closely agree with the values independently determined by Sweeney et al. (1987). They suggested that interval velocities in shales are related to density and porosity, which provide a record of a rock intervals' maximum burial depth or degree of compaction. Through comparison of

interval velocity data with respect to depth in areas with no erosion and areas with an unknown amount of erosion, roughly 5000 – 10000 ft (1524 – 3048 m) of erosion was estimated from different parts of the basin within the study area (Sweeney et al., 1987). Particularly, the average range of eroded thicknesses from areas in close proximity to the three cross sections is 5584 – 7757 ft (1700 – 2364 m), which is close to our suggested range of 6000 – 7200 ft (1830 – 2195 m). Methods of Johnson and Nuccio (1986) and Anders et al. (1992) involved subtracting the present day Kelly bushing elevation from the elevation of surfaces that are thought to preserve maximum sediment accumulation. In the Uinta Basin, it has been suggested that the Gilbert Peak erosion surface may represent the surface of maximum aggradation at an elevation of 10000 ft (3048 m). If this method is utilized, estimated eroded thicknesses from the wells within the three cross sections will range from 2793 to 5021 ft (850 to 1530 m). Calibration to measured data using these estimated thicknesses of eroded material would require heat flow values in excess of 90 $mW/m^2$ which is more characteristic of the southern, eastern, and western margins of the Colorado Plateau, rather than the northern margin (Swanberg and Morgan, 1985). Extrapolation of vitrinite reflectance profiles to 0.2 % $R_0$ yields estimations that range from about 2000 – 6000 ft (610 – 1830 m). As concluded by Johnson and Nuccio (1993), this method yields an unacceptably large range in eroded thicknesses, and therefore, an unacceptably large range in heat flow.

### 5.2 Predicted Maturity

The predicted maturity represents the best estimation of the spatial distribution of mature source rocks in the Parachute Creek Member with the available geochemical data.

Predicted maturity for each interval of interest follows the general trend of increasing maturity from south to north until the northern most margin of the study area is encountered. Local variations in maturity that deviate from the general trend most likely occur due to the effects of decreasing heat flow outweighing the effects of increased burial depth toward the north. Previous modeling efforts near the study area have largely been concentrated on the well Shell 1-11B4 Brotherson, located in T2S R4W, and predicted different situations for middle-upper Green River maturity. Modeling results of Sweeney et al. (1987) show the Mahogany R7 reaching a maximum burial depth of approximately 14400 ft (4390 m) by 30 Ma at well Shell 1-11B4 Brotherson. Their kinetic and thermal model suggests that the Mahogany R7 was within or just entering the earliest stages of oil generation at this depth. Models generated for the same well by Anders et al. (1992) suggest that the onset for oil generation in type 1 kerogen is 11200 ft (3414 m). They generated two models at this well that predicted both a mature and immature situation for the Mahogany R7. In a model where erosion is determined from the surface of maximum aggradation, the Mahogany R7 is predicted to reach depths of 11770 ft (3587 m) when it entered the oil window sometime between 15 Ma – 20 Ma. In a model where erosion is determined from calibration to vitrinite reflectance, the Mahogany R7 is predicted to remain immature. Using the same well, a model generated by Fouch et al. (1994) shows the Mahogany R7 in the early stages of maturity by 10 Ma. Their model assumed no erosion and a larger average paleogeotherm for model calibration. Ruble et al. (2001) developed two models for the Shell 1-11B4 Brotherson well in the Altamont-Bluebell oil field. Utilizing the estimations of erosion determined by Sweeney et al. (1987) and the geotherms of Anders et al. (1992), they tested the effect of

kinetics derived from hydrous pyrolysis and Rock-Eval pyrolysis. The hydrous pyrolysis kinetic model, which utilizes a single activation energy of 68.7 kcal/mol, indicates that oil generation is restricted to intervals below a present day depth of 10500 ft (3200 m) and that the Parachute Creek Member remains immature. The Rock-Eval kinetic model, similar to the one utilized in this study, indicates that both the upper and lower portions of the Green River Formation are predicted to generate hydrocarbons. In this model, the Mahogany R7 achieves a transformation ratio of about 0.2.

The results of the three 2-D models generated in this study suggest that the Mahogany R7 is in the early stages of maturity in select areas within the northern portion of the study area. The highest predicted transformation ratio attained by the Mahogany is 0.14 and this only occurs around one well located along B-B'. In township TS2 R4W, where the Shell 1-11B4 Brotherson well is located, the models predict that the Mahogany R7 just entered the early maturity window, as evidenced by transformation ratios of 0.10 to 0.11.

In order to investigate the effects of erosion on maturity, the three 2-D models were re-calculated with 6400 ft (1950 m), 6100 ft (1860 m), and 6600 ft (2010 m) of uplift and erosion for lines A-A', B-B', and C-C', respectively. All other parameters were held constant from the best-case scenario. Decreasing eroded thicknesses by 600 ft (183 m) on each cross section results in a large difference in predicted maturity. For a comparison of the spatial distribution of maturity, compare extent of maturity in Figures 52-54 with maturity maps (Figures 43-49). In line A-A', maturity of the GG2 interval is pushed north into T4S R4W and intervals GG1-GG0 do not achieve maturity until T3S R4W. The intervals R6-R8 are all immature except for portions of the lower R6 in

between x distances of 80000 – 100000 ft (24384 – 30480 m). In line B-B', GG2 maturity is pushed north just south of T3S R2W, GG1 maturity is pushed north to the central portion of T3S R2W, and GG and GG0 maturity is pushed north into the southern portion of T2S R3W or the northern portion of T3S R3W. The R6-R8 intervals are largely immature except for some discontinuous zones associated with the R6 between x distances of approximately 100000 – 115000 ft (30480 – 35052 m). In line C-C', GG2 maturity is pushed north into T8S R17E, GG1 maturity is pushed north to the northern margin of the Greater Monument Butte field near T4S R1W or T8S R17E where maturity is discontinuous until the northern portion of T3S R1W, and GG and GG0 maturity is pushed north into T2S R1W. The intervals R6-R8 are all predicted to be immature except in the northern most section where patchy zones of maturity exit for the R6.

The purpose of this is not only to demonstrate the effect of eroded thickness on maturity, but to suggest that the Mahogany R7, the richest oil shale in the Uinta Basin, could be within close proximity to the oil window. In this case, with erosion decreased by 600 ft (183 m), the Mahogany R7 is predicted to transition from just below the oil window, as suggested by the best-case scenario, to just above the oil window with transformation ratios approaching 0.1 but never exceeding this value. If changing the eroded thickness by 600 ft (183 m) dictates the difference between a totally immature Mahogany R7 versus a Mahogany R7 within the early stages of maturity, then we feel uncertainty may surround other parameters. Rock properties or the thermal structure could also largely influence maturity if the source bed is indeed near the fringes of the oil window. Although quantifying uncertainty associated with other parameters that impact maturity, such as heat flow or rock thermal conductivities, is difficult, it is feasible that

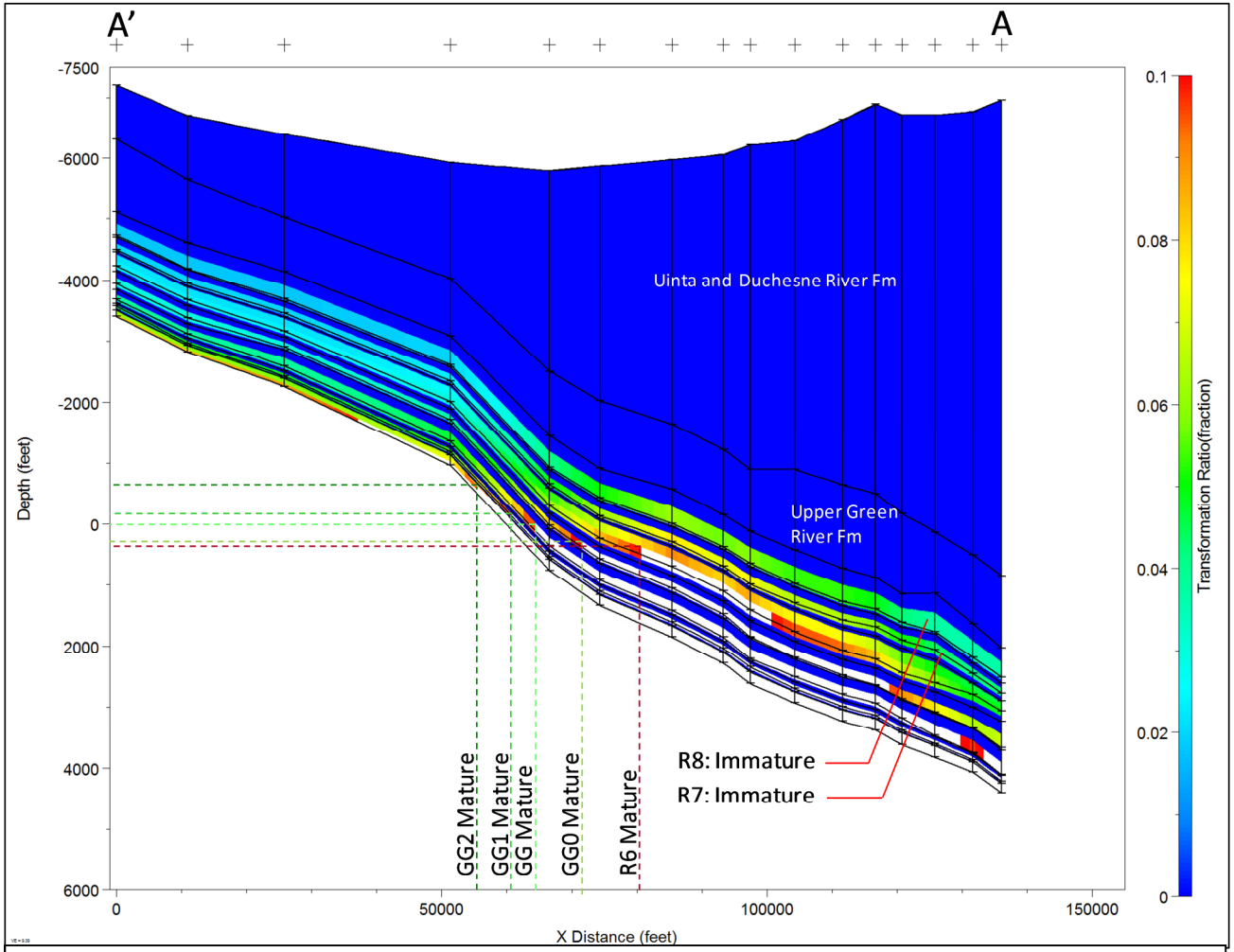


***Figure 52***: Calculated 2-D cross section of A-A' showing lateral changes in model-predicted transformation ratios. The position and depth in which each interval achieves a transformation ratio of 0.1 of greater is marked. This case assumes 6400 ft (1950 m) of erosion. White areas represent mature source rock. Note depth scale is subsea.

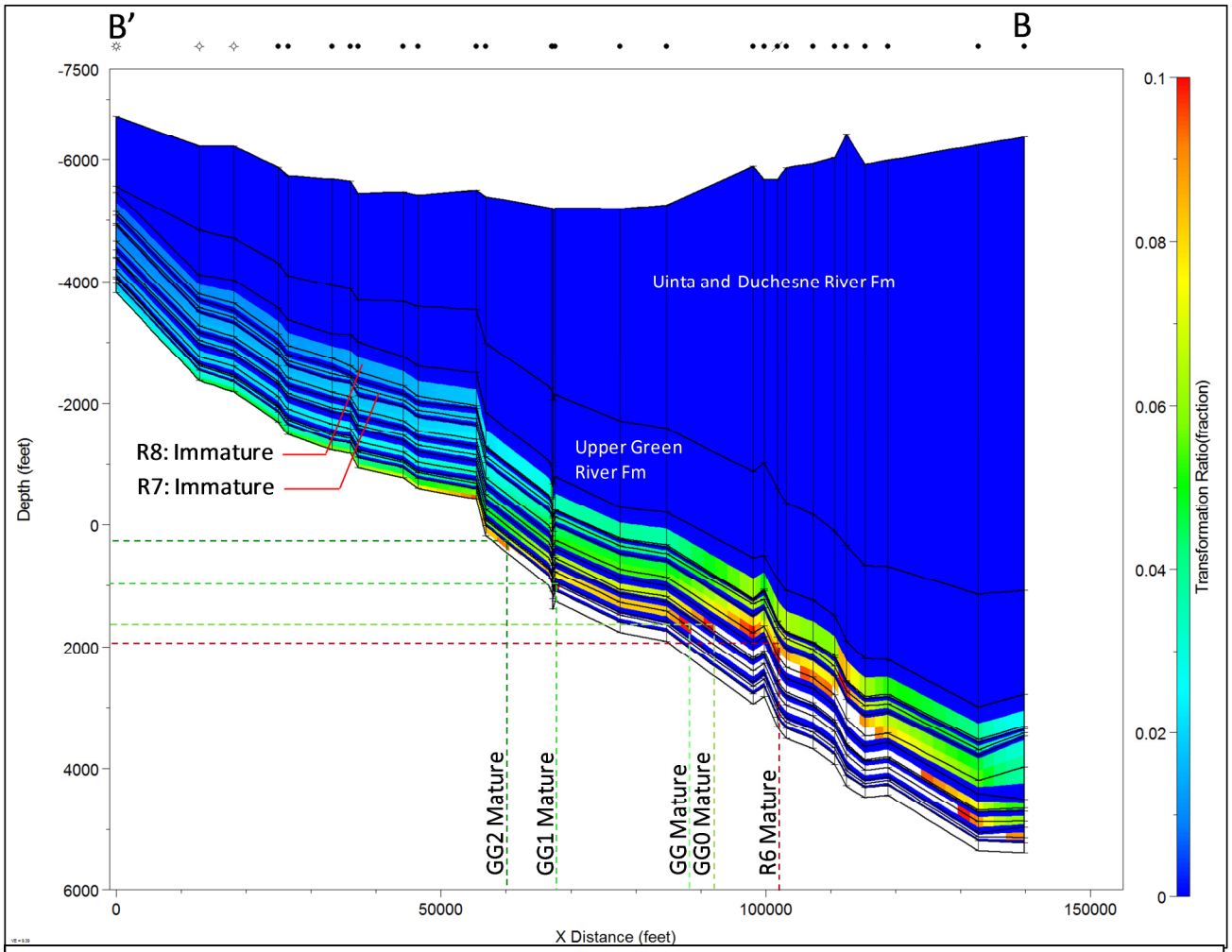


***Figure 53***: Calculated 2-D cross section of B-B' showing lateral changes in model-predicted transformation ratios. The position and depth in which each interval achieves a transformation ratio of 0.1 of greater is marked. This case assumes 6100 ft (1860 m) of erosion. White areas represent mature source rock. Note depth scale is subsea.

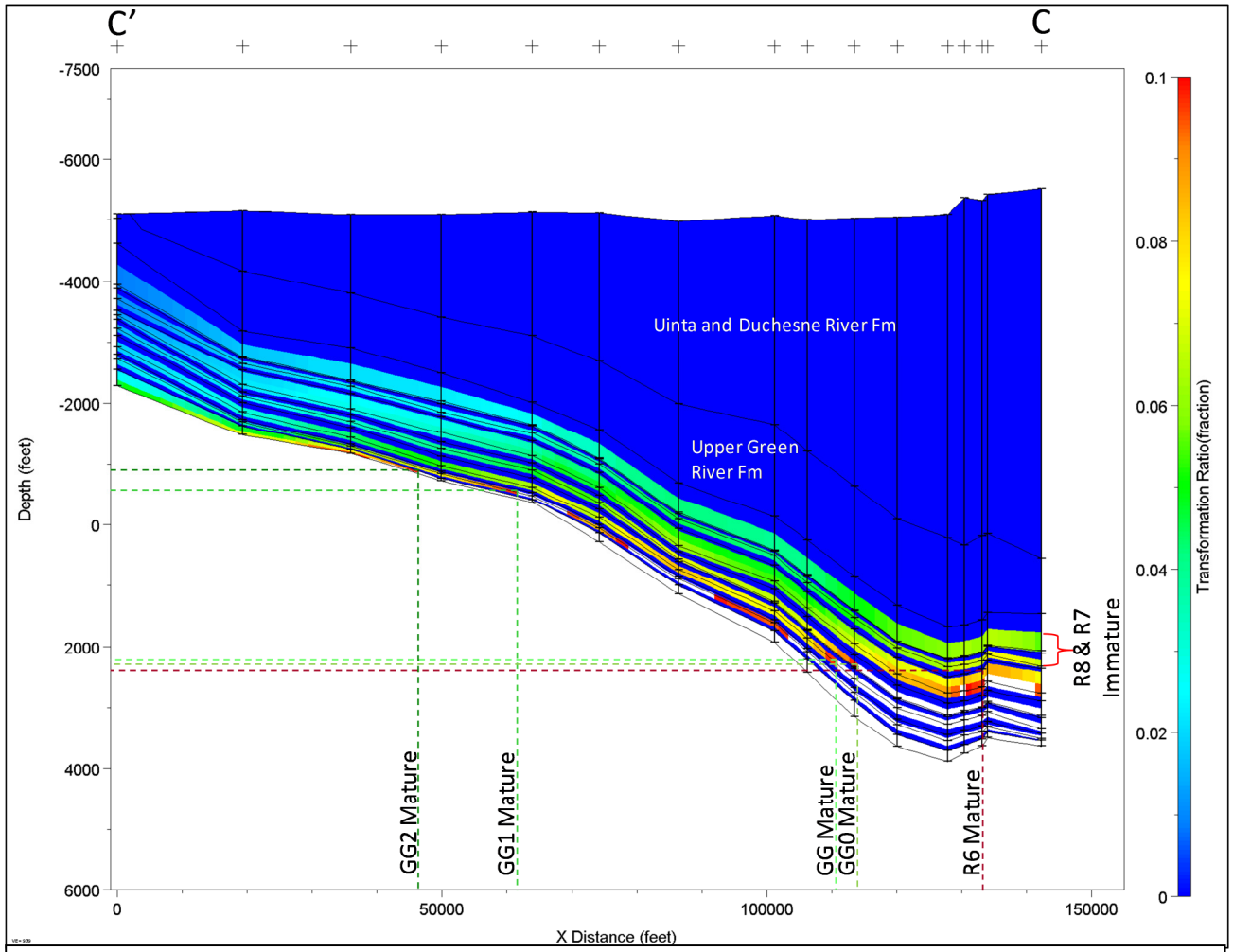


***Figure 54***: Calculated 2-D cross section of C-C' showing lateral changes in model-predicted transformation ratios. The position and depth in which each interval achieves a transformation ratio of 0.1 of greater is marked. This case assumes 6600 ft (2010 m) of erosion. White areas represent mature source rock. Note depth scale is subsea.

minor changes in these could result in major changes in predicted maturity for the Mahogany R7. Improvements to the model predictions could be made by obtaining laboratory measurements of thermal conductivity, conducting detailed analysis of source interval mineral compositions, and acquiring additional measured thermal maturity indicators, particularly toward the north and western portions of the study area. Model-predicted heat flow from the southern and central portions of the study area largely resembled heat flow values determined by Chapman et al. (1984). Availability of maturity indicators obtained from the northern portion would provide a means to verify if the heat flow trends continue to agree with previously suggested values while using our current estimations of uplift and erosion.

## CHAPTER 6: Conclusions

A basin modeling analysis provides a useful means for evaluating how heat flow and uplift or erosion influence the maturation of source beds within the Parachute Creek Member of the Green River Formation in the Uinta Basin. Model calibration to measured vitrinite reflectance and Rock-Eval data from within the study area indicates that reasonable estimations for uplift and erosion range from 6000 – 7200 ft (1830 – 2195 m), depending on the average paleogeotherm. If heat flow remained largely constant through time, as assumed in the best case scenario, then predicted erosion and uplift is 7000 ft (2134 m), 6700 ft (2042 m), and 7200 ft (2195 m) for lines A-A', B-B', and C-C', respectively. The assumption of constant heat flow over time is based on the lack of significant recent magmatic activity within the Uinta Basin. If heat flow was greater in the past, then the amount of erosion and uplift would be less than predicted and would

fall somewhere along the trend shown in Figure 51. The heat flow values and corresponding amounts of uplift and erosion shown in Figure 51 result in similar maturity predictions. Predicted maturity of the GG2-GG0 is generally widespread with GG2 maturity extending across most of the study area and GG0 maturity extending from the northern margin of the study area to the central portions of the central basin area. Maturity of the GG1 and GG is located spatially in between the extent of the underlying GG2 and overlying GG0. Maturity of the R6 interval is mostly concentrated in areas north of the central basin outline and maturity of the Mahogany R7 is predicted in narrower zones in the northeast and northwest portions of the study area. The R8 interval remains largely immature with maturity predicted at only two well locations along B-B'. Maturity is very sensitive to model input parameters such as eroded thicknesses. As demonstrated, the maturity of the Mahogany R7, the richest oil shale in the Uinta Basin, is largely affected by changes in eroded thickness. As a result, it is hypothesized that this source bed lies in close proximity to the oil window. Although results indicate that portions of the Mahogany R7 are in the early stages of maturation, minor changes in eroded thicknesses and other maturity controlling parameters largely dictate whether or not this source interval is mature. Improvements on estimated uplift, heat flow, and predicted maturity are possible with additional data that could better constrain lithologies and rock properties such as thermal conductivity. Finally, additional measured thermal maturity indicators would provide improved control over heat flow and erosion determined during calibration.

# APPENDIX

Odekirk 11-12-3-3W

| Event Name | End Age (Ma) | Top Depth | Present Thickness | Eroded Thickness | Lithology (%) | Kerogen Type | TOC (%) |
|---|---|---|---|---|---|---|---|
| Erosion | 0 | | | -6700 | | | |
| Hiatus | 10 | | | | | | |
| Uinta and Duchesne Rvr Fms | 20 | 0 | 3655.722 | | 90ss/ 10slt | | |
| Grn Rvr Fm | 44 | 3655.72191 | 1389.72031 | | 66ss/ 24sh/ 10evap | | |
| R8 | 48.4 | 5045.44222 | 533.75589 | | 31ss/ 31sh/ 38ls | Type 1 Tissot 87' | 2.28 |
| A Groove | 48.8 | 5579.19811 | 42.33233 | | 10ss/ 30sh/ 60dol | | |
| R7 | 49 | 5621.53044 | 104.3391 | | 31ss/ 31sh/ 38ls | Type 1 Tissot 87' | 4.89 |
| B Groove | 49.3 | 5725.86954 | 118.15171 | | 35ss/ 50sh/ 15dol | | |
| R6 | 49.83 | 5844.02125 | 270.94457 | | 31ss/ 30sh/ 39dol | Type 1 Tissot 87' | 2.75 |
| L5 | 50.53 | 6114.96582 | 146.41656 | | 25ss/ 50sh/ 25dol | | |
| GG0 | 50.68 | 6261.38238 | 171.04142 | | 15ss/ 15sh/ 70dol | Type 1 Tissot 87' | 4.37 |
| L4 | 51 | 6432.4238 | 90.71257 | | 25ss/ 65sh/ 10dol | | |
| GG | 51.5 | 6523.13637 | 147.61834 | | 20ss/ 20sh/ 60dol | Type 1 Tissot 87' | 1.75 |
| L3 | 52.5 | 6670.75471 | 170.8375 | | 90sh/ 10dol | | |
| GG1 | 52.75 | 6841.59221 | 51.13775 | | 38ss/ 38sh/ 24dol | Type 1 Tissot 87' | 2.33 |
| L2 | 53 | 6892.72996 | 105.73885 | | 50sh/ 50 dol | | |
| GG2 | 53.2 | 6998.46881 | 56.59119 | | 38ss/ 38sh/ 24dol | Type 1 Tissot 87' | 2.36 |

**Table 1:** Example of the type of data used in the construction of the basin models consolidated into one table. For each of the 60 1-D models, a table similar to this one is filled out in order to describe the ages, depths, thicknesses, erosion, lithology, kerogen type, and total organic carbon (TOC) associated with each interval at a given well. This data was used to construct the burial history curve for Odekirk 11-12-3-3W, which is located in the central portion of the study area. Depths and thicknesses are in feet. Kerogen types are from Tissot et al. (1987). ss = sandstone, slt = siltstone, sh = shale, ls = limestone, dol = dolomite, and evap = evaporite.

**References:**


Abbott, W., 1957, Tertiary of the Uinta basin, *in* O.G. Seal, ed., Guidebook to the geology of the Uinta basin: Intermountain Association of Petroleum Geologists 8th Annual Field Conference Guidebook, p. 102-109.

Allmendinger, R. W., and Jordan, T. E., 1981, Mesozoic evolution, hinterland of the Sevier orogenic belt: Geology, v. 9, p. 308-313.

Anders, D. E., Palacas, J. G., and Johnson, R. C., 1992, Thermal maturity of rocks and hydrocarbon deposits, Uinta Basin, Utah, in Fouch, T.D., Nuccio, V.F., and Chidsey, T.C., Hydrocarbon and Mineral Resources of the Uinta Basin, Utah and Colorado: Utah Geological Association Guidebook 20: Salt Lake City, Utah, p. 53-76.

Bader, J. W., 2009, Structural and tectonic evolution of the Douglas Creek arch, the Douglas Creek fault zone, and environs, northwestern Colorado and northeastern Utah: Implications for petroleum accumulation in the Piceance and Uinta Basins: Rocky Mountain Geology, v.44, no. 2, p. 121-145.

Bartis, J. T., LaTourrette, T., Dixon, L., Peterson, D. J., and Cecchine, G., 2005, Oil shale development in the United States, prospects and policy issues: Report prepared for the National Energy Technology Laboratory of the U.S. Department of Energy, p. 1-68.

Baur, F., Littke, R., Wielens, H., and Lampe, C., Fuchs, T., 2009, Basin modeling meets rift analysis, a numerical modeling study from the Jeanne d'Arc Basin, offshore Newfoundland, Canada: Marine and Petroleum Geology, v. 27, p. 585-599.

Beghoul, N., and Barazangi, M., 1989, Mapping high *Pn* velocity beneath the Colorado Plateau constrains uplift models: Journal of Geophysical Research, v. 94, p. 7083–7104, doi: 10.1029/JB094iB06p07083.

Birgenheier, L. P., Plink-Bjorklund, P., and Golab, J., 2009, Geochemical and sedimentary record of climate change from the Paleocene-Eocene Colton and Green River Formations, Southwestern Uinta Basin, Utah: Abstracts Volume, American Association of Petroleum Geologists Annual Meeting, Denver, CO, June 7-10, p. 24.

Birgenheier, L. P. and Vanden Berg, M. D., 2011, Core-based integrated sedimentologic, stratigraphic, and geochemical analysis of the oil shale bearing Green River Formation, Uinta Basin, Utah: Topical Report, University of Utah Institute for Clean and Secure Energy 155 South 1452 East, Room 380 Salt Lake City, UT 84112, p. 1-30.

Bird, P., 1984, Laramide crustal thickening event in the Rocky Mountain foreland and Great Plains: Tectonics, v. 3, p. 741–758, doi: 10.1029/TC003i007p00741.

Bradley, W. H., and Eugster, H. P., 1969, Geochemistry and paleolimnology of the trona deposits and associated authigenic minerals of the Green River Formation of Wyoming: U.S. Geological Survey Professional Paper 496-B, 71 p.

Bryant, B., Naeser, C. W., Marvin, R. F., and Mehnert, H. H., 1989, Upper Cretaceous and Paleogene sedimentary rocks and isotopic ages of Paleogene tuffs, Uinta Basin, Utah: U.S. Geological Survey Bulletin 1787-J, 22 p.

Cashion, W. B., 1964, The distribution and quality of oil shale in the Green River Formation of the Uinta Basin, Utah-Colorado: U.S. Geological Survey Professional Paper 501-D, p. D86–D89.

Chapman, D. S., Keho, T. H., Bauer, M. S., and Picard, M. D., 1984, Heat flow in the Uinta Basin determined from bottom hole temperature (BHT) data: Geophysics, v. 49, no. 4, p. 453-466.

Deming, D., and Chapman, D. S., 1989, Thermal histories and hydrocarbon generation: example from Utah-Wyoming thrust belt: American Association of Petroleum Geologists Bulletin, v. 73, no. 12, p. 1455-1471.

Dickinson, W. R., Klute, M. A., Hayes, M. J., Janecke, S. U., Lundin, E. R., McKittrick, M. A., and Olivares, M. D., 1988, Paleogeographic and paleotectonic setting of Laramide sedimentary basins in central Rocky Mountain region: Geological Society of America Bulletin, v. 100, p. 1023-1039.

Dow, W. G., 1977, Kerogen studies and geological interpretations: Journal of Geochemical Exploration, v. 7, p. 79-99.

Dubiel, R. F., 2003, Geology, depositional models, and oil and gas assessment of the Green River total petroleum system, Uinta-Piceance province, eastern Utah and western Colorado: U.S. Geological Survey Digital Data Series DDS-69-B.

Dykstra, J., 1987, Compaction correction for burial history curves: application to Lopatin's method for source rock maturation determination: GeoByte, v. 2:4, p. 16-23.

Dyni, J. R., Milton, C., and Cashion, W. R., 1985, The saline facies of the upper part of the Green River Formation near Duchesne, Utah, in M. D. Picard, ed., Geology and energy resources, Uinta Basin of Utah: Utah Geological Association Publication 12, p. 51–60.

Foos, A., 1999, Geology of the Colorado Plateau: Geology Department, University of Akron, p. 1-6.

Fouch, T. D., Lawton, T. F., Nichols, D. J., Cashion, W. B., and Cobban, W. A., 1983, Patterns and timing of synorogenic sedimentation in Upper Cretaceous rocks of central and northeast Utah, in Reynolds, M.W., and Dolly, E.D., eds., Mesozoic paleogeography of the west-central United States: Society of Economic Paleontologists and Mineralogists, Rocky Mountain Section, p. 305-336.

Fouch, T. D., V. F. Nuccio, D. E. Anders, D. D. Rice, J. K. Pitman, and R. F. Mast, 1994, Green River petroleum system, Uinta Basin, Utah, U.S.A., in L. B. Magoon and W. G. Dow, eds., The petroleum system-from source to trap: American Association of Petroleum Geologists Memoir 60, p. 399–421.

Gable, D. J., and Hatton, T., 1983, Maps of vertical crustal movement in the conterminous United States over the last 100 million years: U.S. Geological Survey Miscellaneous Investigations Map 1-1315, scale 1:10,000,000.

Goebel, K. A., 1991, Paleogeographic setting of Late Devonian to Early Mississippian transition from passive to collisional margin, Antler foreland, eastern Nevada and western Utah, in Cooper, J.D., and Stevens, C.H., eds., Paleozoic paleogeography of the western United States II: Society of Economic Paleontologists and Mineralogists, Pacific Section, p. 401-4l7.

Hamilton, W. B., 1988, Laramide crustal shortening, *in* Schmidt, C.J., and Perry, W.J., Jr., eds., Interaction of the Rocky Mountain foreland and the Cordilleran thrust belt: Geological Society of America Memoir 171, p. 27-39.

Hansen W. R., 1986, History of faulting in the eastern Uinta Mountains, Colorado and Utah, in Stone, D.S., ed., New interpretations of northwest Colorado geology: Rocky Mountain Association of Geologists, p. 5-18.

Hunt, C. B., 1969, Geologic history of the Colorado River: U.S. Geological Survey Professional Paper 669-C, p. 59-130.

Hunt, J., 1979, Petroleum geochemistry and geology: W. H. Freeman and Co., San Francisco, 617 p.

IHS, 2012, Energy Information, Software and Solutions >Analytical and Decision Support Tools <Petra, http://www.ihs.com/products/oil-gas-information/analysis-software/petra.aspx> Accessed October 28, 2012.

Johnson, R. C., 1985, Early Cenozoic history of the Uinta and Piceance Creek basins, Utah and Colorado, with special reference to the development of Eocene Lake Uinta, in Flores, R.M., and Kaplan, S.S., eds., Cenozoic paleogeography of the west-central United States: Society of Economic Paleontologists and Mineralogists, Rocky Mountain Section, p. 247-276.

Johnson, R. C., 1988, Early Cenozoic history of the Uinta and Piceance Creek basins, Colorado and Utah, in Sloss, L.L., ed., Sedimentary cover – North American craton: Geological Society of America, Geology of North America, v. D-2, p. 144-154.

Johnson, R. C., and Johnson, S. Y., 1991, Stratigraphic and time- stratigraphic cross sections of Phanerozoic rocks along line B–B', Uinta and Piceance Basin area, west-central Uinta Basin, Utah, to eastern Piceance Basin, Colorado: U.S. Geological Survey Miscellaneous Investigations Series Map I–2184–B, 2 sheets.

Johnson, R. C., and May, F., 1980, A study of the Cretaceous-Tertiary unconformity in the Piceance Creek Basin, Colorado: the underlying Ohio Creek Formation (Upper Cretaceous) redefined as a member of the Hunter Canyon or Mesaverde Formation: U.S. Geological Survey Bulletin 1482-B, 27 p.

Johnson, R. C., and Nuccio V. F., 1986, Structural and thermal history of the Piceance Creek Basin, Western Colorado, in relation to hydrocarbon occurrence in the Mesaverde Group: U.S. Geological Survey, Denver, Colorado, p. 165-205.

Johnson, R. C., and Nuccio, V. F., 1993, Surface vitrinite reflectance study of the Uinta and Piceance Creek area, eastern Utah and western Colorado- implications for the development of Laramide basins and uplifts: U.S. Geological Survey Bulletin 1787-DD, 38 p.

Johnson, S. Y., 1992, Evolution of sedimentary basins in the Uinta-Piceance basin region, northwestern Colorado and northeastern Utah: U.S. Geological Survey Bulletin 1787, p. FF1-FF38.

Kluth, C. F., 1986, Plate tectonics of the ancestral Rocky Mountains, in Peterson, J.A., ed., Paleotectonics and sedimentation in the Rocky Mountain region, United States: American Association of Petroleum Geologists Memoir 41, p. 535-370

Kominz, M. A., and Bond, G. C., 1991, Unusually large subsidence and sea level events during middle Paleozoic time: New evidence supporting mantle convection models for supercontinent assembly: Geology, v. 19, p. 56-60.

La Rocque, A., 1960, Molluscan faunas of the Flagstaff Formation of central Utah: Geological Society of America Memoir 78, 100 p.

Lerche, I., 1990, Basin Analysis - Quantitative Methods, Volume 1, San Diego: Academic Press, Inc., 562 pages.

Liu, L., and Gurnis, M., 2010, Dynamic subsidence and uplift of the Colorado Plateau: Geological Society of America, v. 38, p. 663-666.

Morgan, P., and Swanberg, C. A., 1985, On the Cenezoic uplift and tectonic stability of the Colorado Plateau: Journal of Geodynamics, v. 3, p. 39-63.

Morgan, C. D., Chidsey, T. C., McClure, K. P., Bereskin, S. R., and Deo, M. D., 2003, Reservoir characterization of the Lower Green River Formation, Uinta Basin, Utah: Utah Geological Survey Open File Report 441, 140 p.

Moucha, R., Forte, A. M., Rowley, D. B., Mitrovica, J. X., Simmons, N. A., and Grand, S. P., 2009, Deep mantle forces and the uplift of the Colorado Plateau: Geophysical Research Letters, v. 36, L19310, doi: 10.1029/2009GL039778.

Narr, W., and Currie, J. B., 1982, Origin of fracture porosity-example from Altamont Field, Utah: American Association of Petroleum Geologists Bulletin, v. 66, p. 1231-1247.

Nicolo, M. J., Dickens, G. R., Hollis, C. J., and Zachos, J. C., 2007, Multiple early Eocene hyperthermals: Their sedimentary expression on the New Zealand continental margin and in the deep sea: Geology, v. 35, p. 699-702.

Nuccio, V. F., and Condon, S. M., 1996, Burial and thermal history of the Paradox basin, Utah and Colorado, and petroleum potential of the Middle Pennsylvanian Paradox Formation: U.S. Geological Survey Bulletin 2000–O, 41 p., 2 plates.

Nuccio, V. F., and Roberts, L. N. R., 2003, Thermal Maturity and oil and gas generation history of petroleum systems in the Uinta-Piceance province, Utah and Colorado: U.S. Geological Survey Digital Data Series DDS-69-B, chp. 4.

Osmond, J. C., 1965, Geologic History of Site of Uinta Basin, Utah: American Association of Petroleum Geologists Bulletin, v. 49, no. 11, p. 1957-1973.

Osmond, J. C., 2003, History of Oil and Gas Exploration in the Uinta Basin, Utah: The Mountain Geologist, v. 40, no. 4, p. 101-110.

Platte River Associates, 2012, Premier Petroleum Services and Software, <http://www.platte.com/software/> Accessed September 26, 2012.

Plink-Bjorklund, L. P., Golab, J., and Birgenheier, L. P., 2010, Separating allogenic and autogenic controls in a super-greenhouse fluvial system: Abstracts Volume, American Association of Petroleum Geologists Annual Meeting, New Orleans, LA, April 11-14, no. 735331.

Price, L. C., and Barker, C. E., 1985, Suppression of vitrinite reflectance in amorphous rich kerogen – a major unrecognized problem: Journal of Petroleum Geology, v. 8, p. 59-84.

Remy, R. R., 1992, Stratigraphy of the Eocene part of the Green River Formation in the southcentral part of the Uinta Basin, Utah: U. S. Geological Survey Bulletin 1787, Evolution of Sedimentary Basins - Uinta and Piceance Basins, Chapter BB, 80 p.

Roy, M., Jordan, T.H., and Pederson, J., 2009, Colorado Plateau magmatism and uplift by warming of heterogeneous lithosphere: Nature, v. 459, p. 978–982, doi: 10.1038/nature08052.

Ruble, T. E., Lewan, M. D., and Philip, R. P., 2001, New insights on the Green River petroleum system in the Uinta Basin from hydrous pyrolysis experiments: American Association of Petroleum Geologists Bulletin, v. 85, no. 8, p. 1333-1371.

Ryder, R. T., Fouch, T. D., and Elison, J. H., 1976, Early Tertiary sedimentation in the western Uinta Basin, Utah: Geological Society of America Bulletin, v. 87, p. 496-512.

Sclater, J. G. and Christie, P. A. F., 1980, Continental stretching: an explanation of the post-mid-cretaceous subsidence of the central North Sea basin: Journal of Geophysical Research, v. 85, p. 3711-3739.

Sexton, P. F., Wilson, P. A., and Norris, R. D., 2006. Testing the Cenozoic multisite composite d18O and d13C curves: New monospecific Eocene records from a single locality, Demerara Rise (Ocean Drilling Program Leg 207): Paleoceanography, v. 21, PA2019, doi:10.1029/20095PA001253.

Smith, M. E., Carroll, A. R., and Singer, B. S., 2008, Synoptic reconstruction of a major ancient lake system: Eocene Green River Formation, western United States: GSA Bulletin, v.120, no. 1-2, p. 54-84.

Smith, M. E., Chamberlain, K. R., Singer, B. S., Carroll, A. R., 2010. Eocene clocks agree: Coeval 40Ar/39Ar, U-Pb, and astronomical ages from the Green River Formation: Geology, v. 38, no. 6, p. 527-530.

Spieker, E. M., 1946, Late Mesozoic and early Cenozoic history of central Utah: U.S. Geological Survey Professional Paper 205-D, p. 117-161.

Stanley, K. O., and Collinson, J. W., 1979, Depositional history of the Paleocene – lower Eocene Flagstaff Limestone and coeval rocks, central Utah: American Association of Petroleum Geologists Bulletin, v. 63, no. 3, p. 311-323.

Steckler, M. S., and Watts, A. B., 1978, Subsidence of the Atlantic-type continental margin off New York: Earth and Planetary Science Letters, 41, p. 1-13.

Swanberg, C. A., and Morgan, P., 1985, Silica heat flow estimates and heat flow in the Colorado Plateau and adjacent areas: Journal of Geodynamics, v. 3, p. 65-85.

Sweeney, J. J., Burnham, A. K., and Bruan, R. L., 1987, A model of hydrocarbon. generation from type I kerogen, application to Uinta Basin, Utah: American Association of Petroleum Geologists Bulletin, v. 71, no. 8, p. 967-985.

Thorman, C. H., Ketner, K. B., Brooks, W. E., Snee, L. W., and Zimmermann, R. A., 1991, Late Mesozoic-Cenozoic tectonics in northeastern Nevada, in Raines, G.L., Lisle, R.E., Schafer, R.W., and Wilkinson, N.H., eds., Geology and ore deposits of the Great Basin: Geological Society of Nevada, p. 25-46.

Tissot, B., G. Deroo, and A. Hood, 1978, Geochemical study of the Uinta basin-Formation of petroleum from the Green River Formation: Geochimica et Cosmochimica Acta, v. 42, p. 1469– 1485.

Tissot, B. P., Pelet, R., and Ungerer, P.H., 1987, Thermal history of sedimentary basins, maturation indices, and kinetics of oil and gas generation: American Association of Petroleum Geologists Bulletin, v. 71, no. 12, p. 1445-1466.

Untermann, G. E., and Untermann, B. R., 1964, Geology of Uintah County: Utah Geological and Mineralogical Survey Bulletin, v. 72, 112 p.

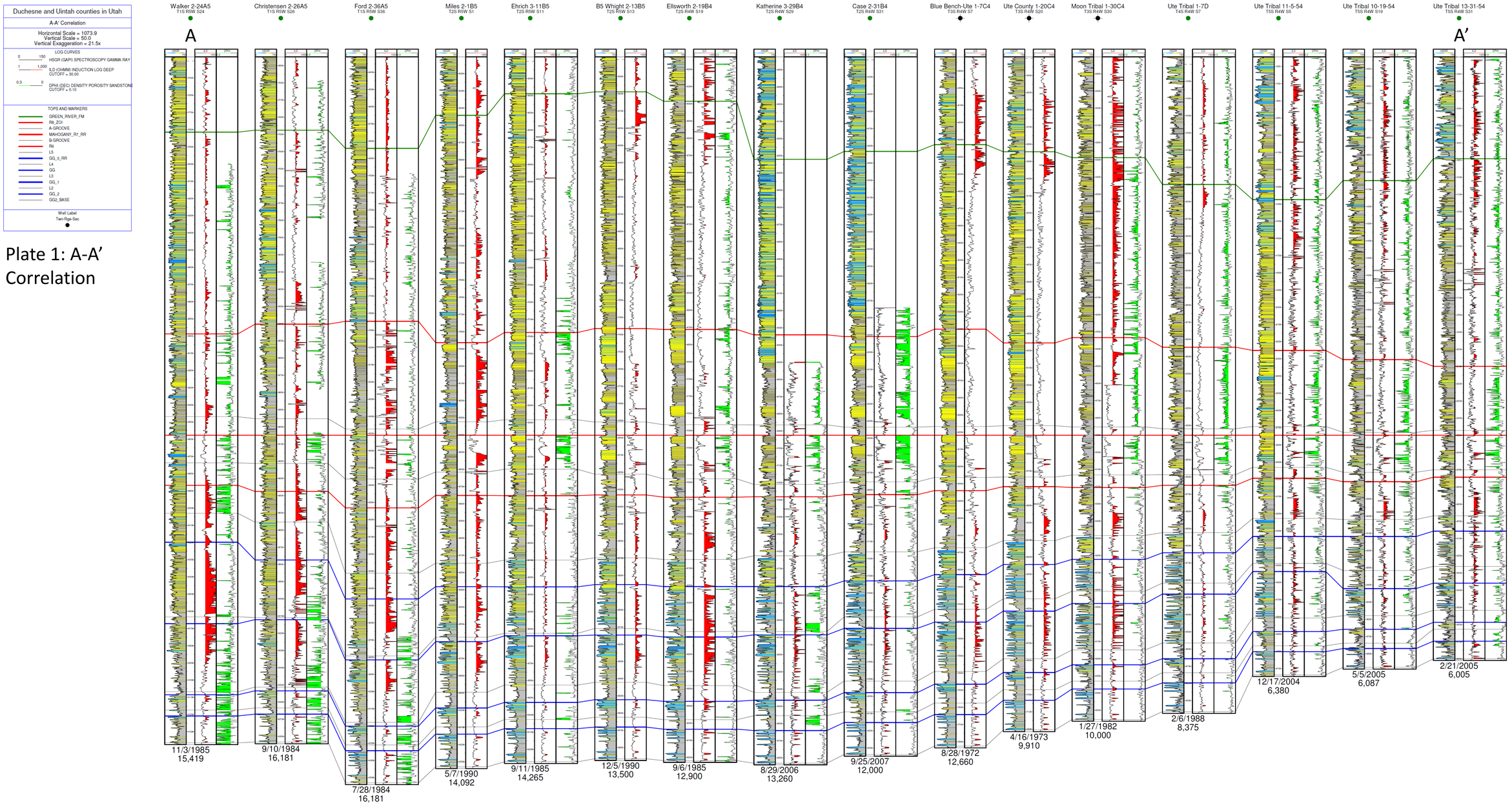


# Plate 1: A-A' Correlation

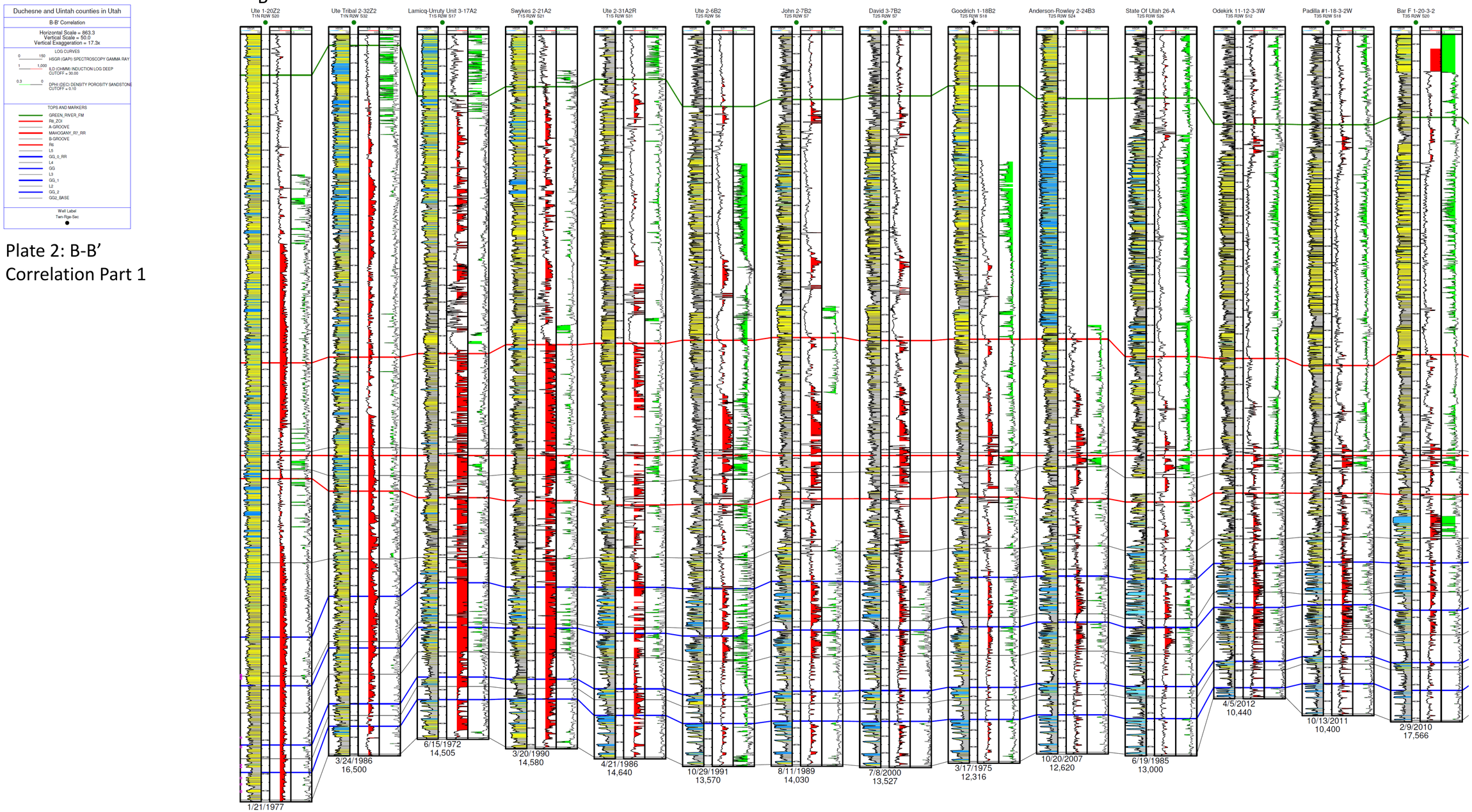


Plate 2: B-B’ Correlation Part 1

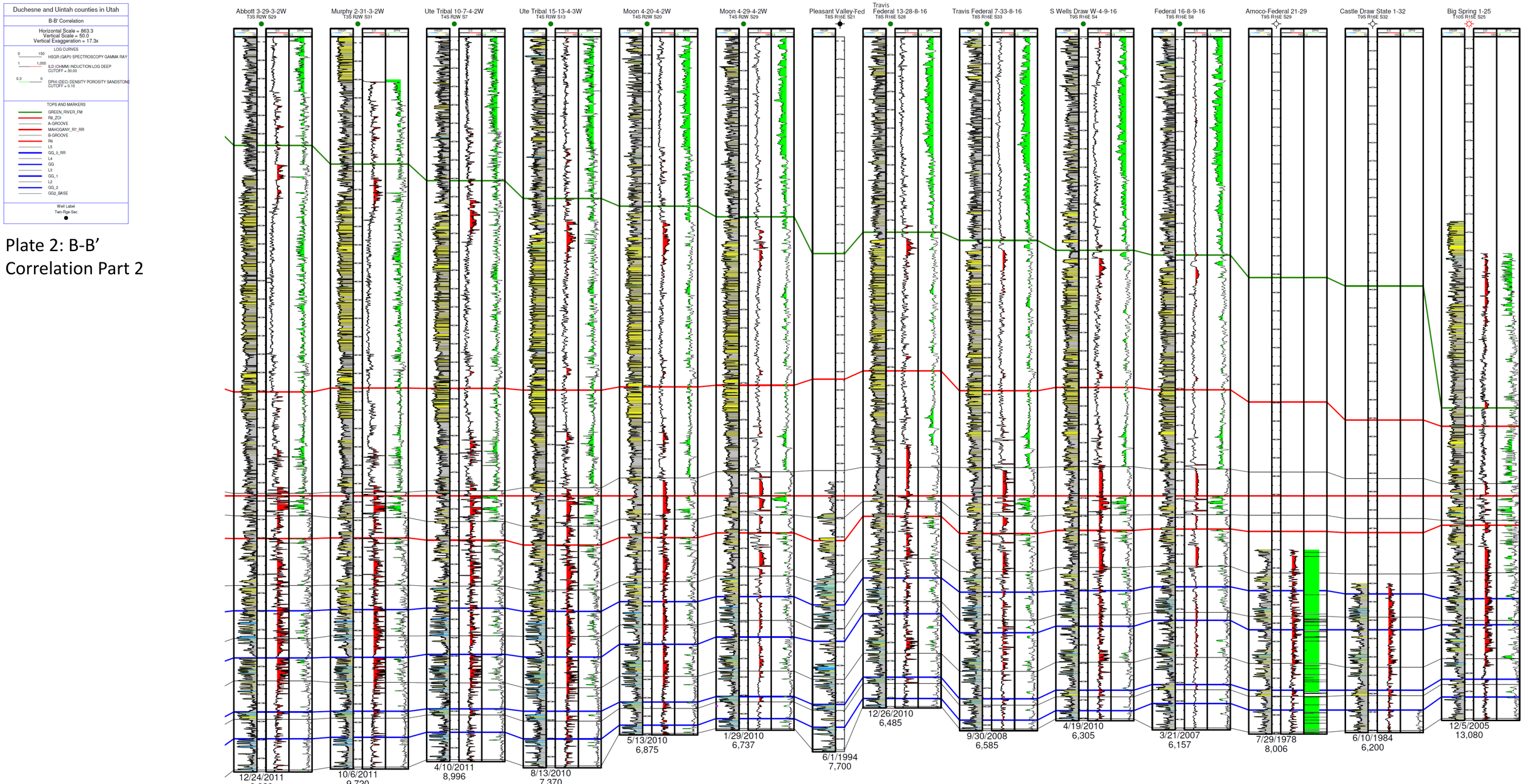


Plate 2: B-B' Correlation Part 2

Duchesne and Uintah counties in Utah

C-C' Correlation

Horizontal Scale = 1123.7
Vertical Scale = 50.0
Vertical Exaggeration = 22.5x

LOG CURVES

0 — 150 HSGR (GAPI) SPECTROSCOPY GAMMA RAY

1 — 1,000 ILD (OHMM) INDUCTION LOG DEEP
CUTOFF = 30.00

0.3 — 0 DPHI (DEC) DENSITY POROSITY SANDSTONE
CUTOFF = 0.10

TOPS AND MARKERS

- GREEN_RIVER_FM
- Rb_ZOI
- A-GROOVE
- MAHOGANY_R7_RR
- B-GROOVE
- Rb
- L5
- GG_0_RR
- L4
- GG
- L3
- GG_1
- L2
- GG_2
- GG2_BASE

Well Label
Twn-Rge-Sec

# Plate 3: C-C' Correlation